NOVEL ELECTROWINNING OF ZINC FROM ZINC OXIDE COMPOUND IN LOW TEMPERATURE IONIC LIQUID

by

HAOXING YANG

RAMANA G. REDDY, COMMITTEE CHAIR

NITIN CHOPRA
SUBHADRA GUPTA
HUNGTA WANG
UDAY VAIDYA

A DISSERTATION

Submitted in partial fulfillment of the requirements
for the degree of Doctor of Philosophy
in the Department of Metallurgical and Materials Engineering
in the Graduate School of
The University of Alabama

TUSCALOOSA, ALABAMA

2015

ABSTRACT

A novel method for zinc electrodeposition was investigated by using a urea and choline chloride in a molar ratio of 2:1 low temperature deep eutectic solvent as electrolyte. The dissolution of zinc oxide was investigated using FTIR and corresponding solubility measurement was carried out in ICP-AES. Through direct comparison of IR Peak identified for the $[ZnO{\cdot}Cl{\cdot}urea]^-$ complex, optimized solubility was found at a temperature of 100°C. The dissolution limit is approximated in FTIR with 1.23 mol/L ZnO in the Urea/ChCl eutectic mixture and is verified in ICP-AES with a measurement of 90584 ppm at 100°C.

The reduction potential of Zn^{2+} to Zn was found at -1.1V, using Ag as reference electrode. The reduction of Zn and its corresponding stripping process was characterized as irreversible and controlled by diffusion. The diffusion coefficient was confirmed with an average value of 1.89 $\times 10^{-8}$ cm^2/s at 100°C. The nucleation process was characterized as instantaneous by comparing with 3-D nucleation model. Process variables such as temperature and surface lubricant concentration were investigated in order to improve deposit layer surface quality. Temperature was proven to have large impact of the formation of deposit layer as nodular cauliflower like structure was formed at the top of each particle at 100°C. The addition of $[Bmim]HSO_4$ can effectively generate a more compact surface layer on the cathode and promote an improved finer grain size.

Lab-scale electrowinning of Zn was conducted from applied potentials from 3.2 to 3.5V at 90°C. Concentration polarization was confirmed in the beginning of the reaction and the diffusion coefficient was confirmed with an average value of 7.85×10^{-9} cm^2/s at 90°C which agrees to the

previous value. A gradual increase of current density was due to activation polarization in which a linear correlation between current density and over-potential was confirmed. The kinetics study of the electrowinning process was carried out in the steady-state region. Tafel plots were obtained in temperatures from 80 to 100°C. The activation energy was obtained as 3.85 kJ/mol. The effect of applied potential on microstructure was investigated. It was seen that dendrites formed in a higher over-potential of -0.65V and was beyond the calculated critical value for dendrite formation which is equal to -0.62V. Process variables such as cell voltage, temperature, and surface additive concentration were investigated to obtain higher current efficiency and lower energy consumption. An efficiency as high as 92.6% was obtained with 2.0mg/mL [Bmim]HSO_4 at 100°C, 3.3V showing a promising advantage over conventional zinc electrolytic technology which owns a efficiency close to 90%.

The feasibility of this novel technology was explored for large scale application, for example, in batch mode. Electrowinning duration is the main variable that was investigated under batch mode. The current efficiency was calculated with an average value of 88.8 ± 0.1% irrespective of electrowinning time. Correspondingly, energy consumption was calculated to be 3.23 ± 0.03 kWh/kg which shows reasonable agreement with results calculated in small scale electrowinning. The rate of cathodic weight gain is equal to 9.01 $\times 10^{-4}$ g/min at given condition. In addition, the graphite anode is proven to be stable during the long-term electrowinning as the rate of anodic weight loss is equal to 5.82×10^{-5} g/min

A model was established to study the electrolyte fluid flow velocity distribution in the electrowinning reactor. Results were illustrated that velocity in between electrodes is higher than other domain leading to the formation of cycling flow.

DEDICATION

To my parents, family and anyone who helped and guided me in the fulfillment of this work.

ACKNOWLEDGMENTS

My stay at the University of Alabama, Tuscaloosa was a profound academic adventure as well as a personal journey that I have learned many lessons helped me grown intellectually. I have benefited a lot from interactions and discussions with my professors, colleagues and friends. I couldn't have achieved it without their help and encouragement.

First of all, I would like to express my deepest sense of gratitude to my advisor, Dr. Ramana G Reddy for his guidance and persistent help during my graduate study and in my pursuit of doctoral degree.

I would like to express my sincere thanks to Dr. Nitin Chopra, Dr. Subhadra Gupta, Dr. Hungta Wang, and Dr. Uday Vaidya for serving as my committee members. Their invaluable comments and suggestions motivate me accomplishing this work.

With high regards, I would like to thank Dr. Tao Wang, Dr. Murali, Min Li, Malli Bogala for advising the experimental procedure, as well as assistance and discussion. I would like to express my sincere appreciation for all other group members for their unending support.

I would like to thank my Mom. She is the only person in this world who has been with me and experienced every second of my life, my greatest appreciation to her. Without her love and support, I couldn't have accomplished anything. Though geographically she is thousands miles away from me, she is always acting like a harbor for me, taking all the trouble I met away from

me, letting me smile, doing whatever she can do to encourage me. In here, I want to take this opportunity to thank my dear Mom for helping me reach where I am now.

I would like to thank The University of Alabama for giving me a treasured opportunity to further my study and lead me in a whole different life. Needless to say this place has generated many lingering memories for me to treasure for a lifetime. I would like to acknowledge the financial support from the U.S Department of Energy (DOE) under the grant number DE-EE0003459, and National Science Foundation (NSF) under the grant number NSF-No.1310072 throughout this research work.

CONTENTS

LIST OF TABLES

LIST OF FIGURES

CHAPTER 1

INTRODUCTION

Metal extraction process has been developed since metal was firstly found in early 8000 BC. As the need for metal grown since industrial civilization, metallurgy and the metal extraction process took an important part in mass production of metals and alloys for infrastructure, construction and weapon production for human hunting**.** Metals exist in the earth's crust as chemical states of (i) oxides; (ii) sulfides; (iii) oxysalts. The extraction process of metal from its ore depends on its physical and chemical properties as well as availability of ores. At the beginning, the beneficiation also known as concentration of the ore is vital, either to increase the purity or to better use of physical properties so as to facilitate the metal extraction process. The mining process usually includes several operations, namely, (i) comminution: Reduction of particle size achieved by detaching valuable parts from materials of no value; (ii) separation: Minerals are separated from each other because of difference in physical properties, such as density and physical shape, and chemical properties between species.

The most widely used methods for metal extraction are usually referred to as (a) pyrometallurgy, (b) hydrometallurgy, and (c) electrometallurgy. Pyrometallurgy involves reactions that taken place at high temperature where the decomposition of ore occurs employing enormous amount of heat and a reducing agent thereby other elements are separated from the metal in a form of gas or slag. Some metals such as iron, copper, aluminum, magnesium, sodium whose

oxides are less reactive are produced by this process **[1].** Four sub-categories of pyrometallurgy are generally referred, they are calcining, roasting, smelting, and refining. Calcination process is the thermal decomposition of a material ($CaCO_3$, $FeCO_3$) taken place in a variety of furnaces. Roasting process is the gas-solid reaction occurred at elevated temperature. The most common example for roasting is the oxidation of the metal sulfide ores. Smelting process is known for a reaction which involves the materials in molten phase. The required temperature is usually above the melting temperature of the product. Basically, smelting is the following step after roasting; the obtained oxide can be heating with reducing agent (coke or charcoal) liberating oxygen in a form of carbon oxide and leaving the refined mineral behind. Refining is the removal of the impurities at higher temperature. For the purpose of differentiating from electro-refining, in the pyrometallurgy process, it is generally referred to as fire refining.

Hydrometallurgy is another method to obtain metal from its ore. It involves reactions in aqueous solution for metal recovery, concentration and recycling of the residual materials **[2]**. Hydrometallurgy can be described as three primary steps. Leaching is the process where an aqueous solution containing lixiviant is used to create complete contact with the metal ores in order to selectively dissolve desired metal in the solvent and leave behind the other carriers in the underflow. This process is controlled by reduction potential of metals, PH of the solution, as well as temperature of the reaction. After leaching, solution concentration and purification of the metal ions are required to remove undesirable metal ions. The final step in a hydrometallurgy process is referred to as metal recovery. The primary types of metal recovery is mentioned as electrolysis and precipitation. Electrowinning and electrorefining involve the recovery of the metal using electro-deposition on the cathode and metal dissolution or another oxidation reaction occurred on the anode. Precipitation generally involves the chemical precipitation where contaminates or the

undesired compounds precipitated from the solution. The most common used example for hydrometallurgy is Cu where Cu^{2+} reduced to Cu at mild potentials and leaving other more reactive metal cations such as Zn^{2+} or Fe^{3+} in the solution.

The method of hydrometallurgy is well suited for complex ores but cannot be applied to reactive metals such as aluminum, magnesium, and titanium for which hydrogen liberates prior to the metal. As a result, for reactive metal, electrometallurgical method is preferred. The electrometallurgical process is usually divided into four major categories: electrowinning (extraction), electrorefining (purification), electroforming (formation of thin metal parts) and electroplating (formation of metal layer on substrate) **[3]**. A typical electro-deposition cell consists of an electrode system and electrolyte from which metal is deposited on to the cathode, with the anode acting as an inert conductor. Electrowinning is widely used for the extraction of reactive metals such as aluminum and magnesium as an alternative way to pyrometallurgy. More noble metals such as Ni, Zn and Pb can be extracted from their sulphate solution after the leaching process. This dissertation emphasizes the use of electrometallurgical process to reduce zinc oxide to zinc. In the following section, a detailed introduction of various zinc production methods will be given.

1.1 Introduction to zinc and conventional zinc production methods

Zinc is the 24^{th} most abundant metal element making up about 0.0075% of the earth's crust **[4].** Pure Zinc is a silvery-white lustrous metal which owns attractive characteristics that enables it to be extensively used in different applications. Zinc is well-known for its distinguishable abilities to resist corrosion as well as oxidation. Galvanization is by far the largest application of zinc, which uses about 50% Zn throughout the world, promotes a coating on iron or steel to prevent from corrosion and oxidation **[5]**. Another major application for Zn production is brass, which is

known as a zinc contained alloy. Brass has superior corrosion resistance as well as high ductility which makes up 17% usage of Zn production. The main uses of Zn production is shown in Figure 1.1 **[6]**.

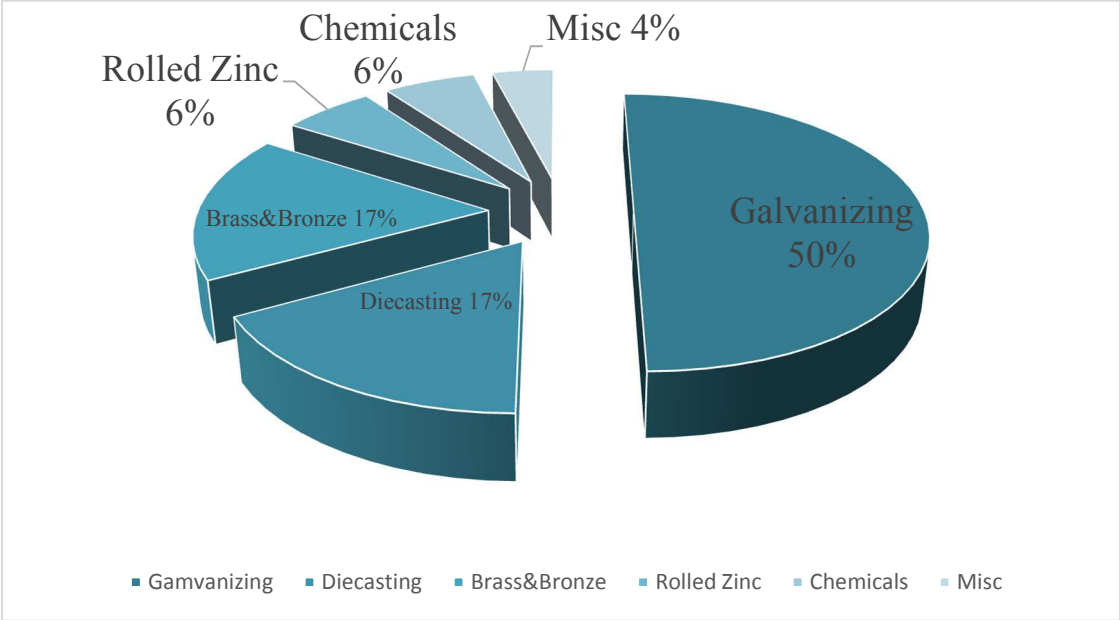

Figure 1.1 Main uses of Zinc

Zn is the fourth most commonly used metal in the world, falling behind iron/steel, aluminum and copper, with an annual production of approximately 13 million tons**.** The World zinc production trend is described in Figure 1.2 **[7]**.

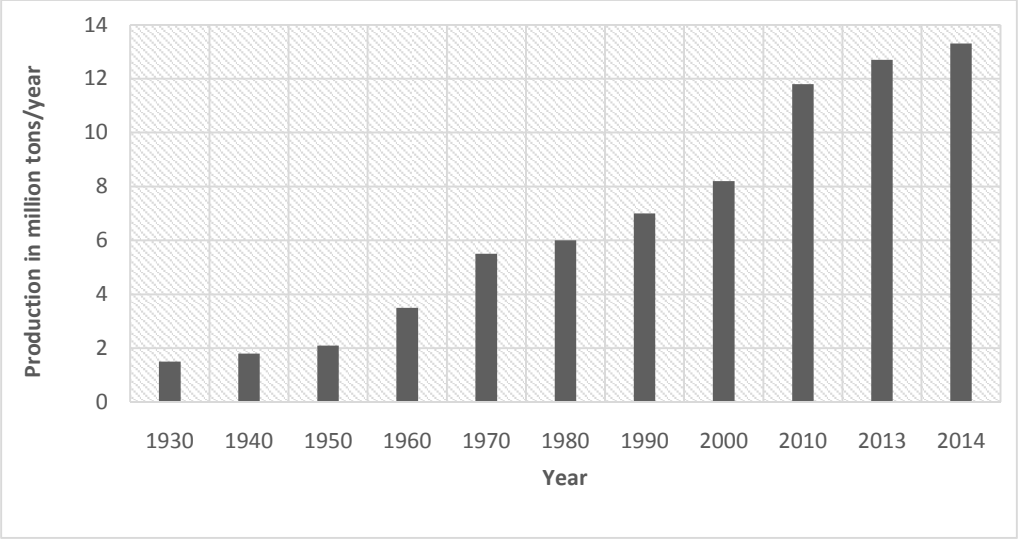

Figure 1.2 World Zn production from 1930 to 2014

Zinc manufacturing methods can be categorized to primary and secondary zinc processing. Primary zinc processing accounts for more than 90% of zinc production throughout the world. It starts from the zinc ore mining. Zinc ores are dug from underground mines utilizing some conventional techniques such as drilling, blasting, and hauling. The as mined ores are generally not enough for directly using for further smelting, which means concentration is required prior to transport to smelters. The commonly available concentration process is known as froth flotation. This process involves grinding of the zinc ores to finer powders and then mixed with water, oil as well as a variety of flotation chemicals. The chemicals are used to coat important zinc particles and as the air is injected, the coated particles flows out in a form of bubbles. It is driven by an impeller, and as the agitation proceeds, zinc minerals rises to the top while the residue remains in the bottom of the pulp. The froth is then filtered to remove water, oil and other coated particles. The concentrates are being roasted at a temperature more than 900°C where zinc blende (ZnS) completely converts to zinc oxide, releasing sulphur dioxide in a form of gaseous product. It is followed by a process called leaching. The obtained SO_2 is subsequently converted to sulfuric acid

which is employed as leaching solution to separate zinc oxide from other calcines. In this stage, zinc content can be easily dissolved while other metal contents such as iron, lead and silver remains in a form of precipitates or undissolved. Further purification is required for the dissolved solution to remove other impurities that yet to be eliminated during the leaching process. Purification is primarily done by adding zinc dust to the solution. All the element to be removed lie underneath zinc in the electrolyte can be precipitated by cementation. The purified solution is then piped in to an electrowinning cell where the zinc is electrodeposited on aluminum cathode and oxygen release on lead-silver anode ran by electric current provided from electrical difference of 3.3-3.5 volts **[8]**; the occurring reactions on both electrode are shown below and the primary zinc production flow sheet is shown in Figure 1.3.

Cathode:

$$ZnSO_4 + 2e^- \rightarrow Zn + SO_4^{2-} \quad (1.1)$$

Anode:

$$H_2O \rightarrow 0.5O_2 + 2H^+ + 2e^- \quad (1.2)$$

Overall:

$$ZnSO_4 + H_2O \rightarrow Zn + 0.5O_2 + H_2SO_4 \quad (1.3)$$

The process takes advantage of low cost of raw materials and relatively high current efficiency as well as low energy consumption. However, the problems associated are also vital. Primary zinc production method produces air emissions. Mass release of SO_2 is a major concern to the environment as well as to human health. Although most of the emissions are recovered on site in sulfuric acid production plant, where sulfuric acid solution is produced, people who work in the Zn production plant suffer from potential health problems. Moreover, rigorous purification process is required in order to achieve zinc in high purity. Correspondingly, high processing as well as labor cost should be seriously considered.

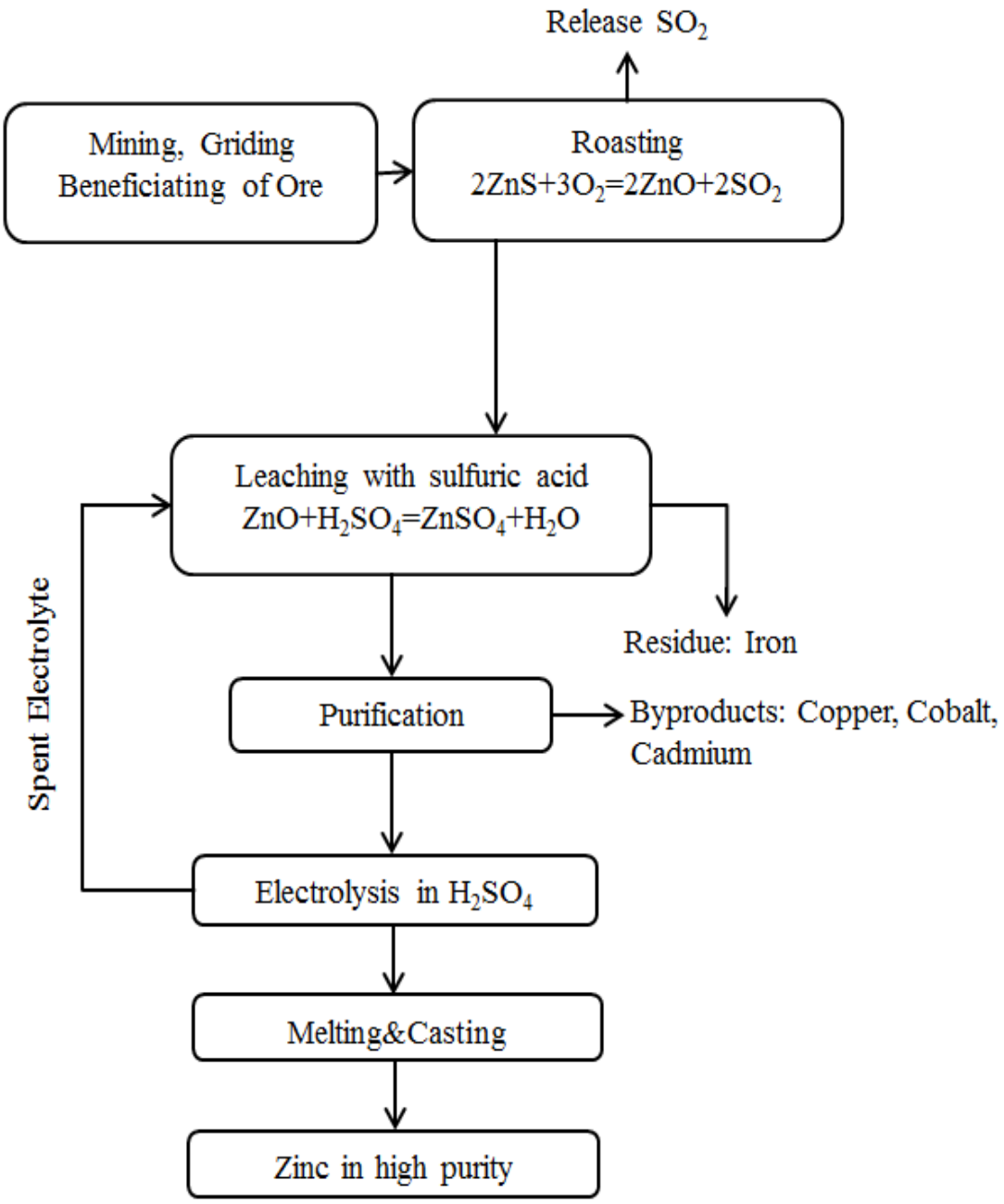

Figure 1.3 Flow sheet of Zn production from sulfate electrolytic process

Secondary zinc production uses process scrap from zinc oxide, zinc slabs, zinc dusts and furnace dust of galvanized steel making plants. Unlike primary zinc production utilizes hydrometallurgical process, zinc is recovered using pyrometallurgical refinement techniques. Once obtained, the secondary zinc undergoes a downdraft sintering operation. A mixture of roaster calcine and EAF calcine is loaded in the sinter together with combustion gases. Carbon in the combustion gases react with some of the impurities such as lead, cadmium, and halides, driven off from the filtration bag. The sintered product is then charged with coke into an electric retort furnace. Coke is used to provide electrical resistance as well as to produce carbon monoxide. The reaction occurred in the furnace is described as follows.

$$ZnO + CO \rightarrow Zn\ (vapor) + CO_2 \qquad (1.4)$$

In this process, a spray of molten lead droplets is used to rapidly cool down and absorb the zinc vapor, regardless of the high concentration of carbon dioxide. The liquid zinc is then separated from the lead in the cooling process. The pyrometallurgical process is an energy intensive process and the highest purity is can achieve is 98%. Today, it is only in operation in Japan, India, China and Poland [**9**]. A comparison between Primary and secondary zinc production methods are described as shown in the following flow sheet.

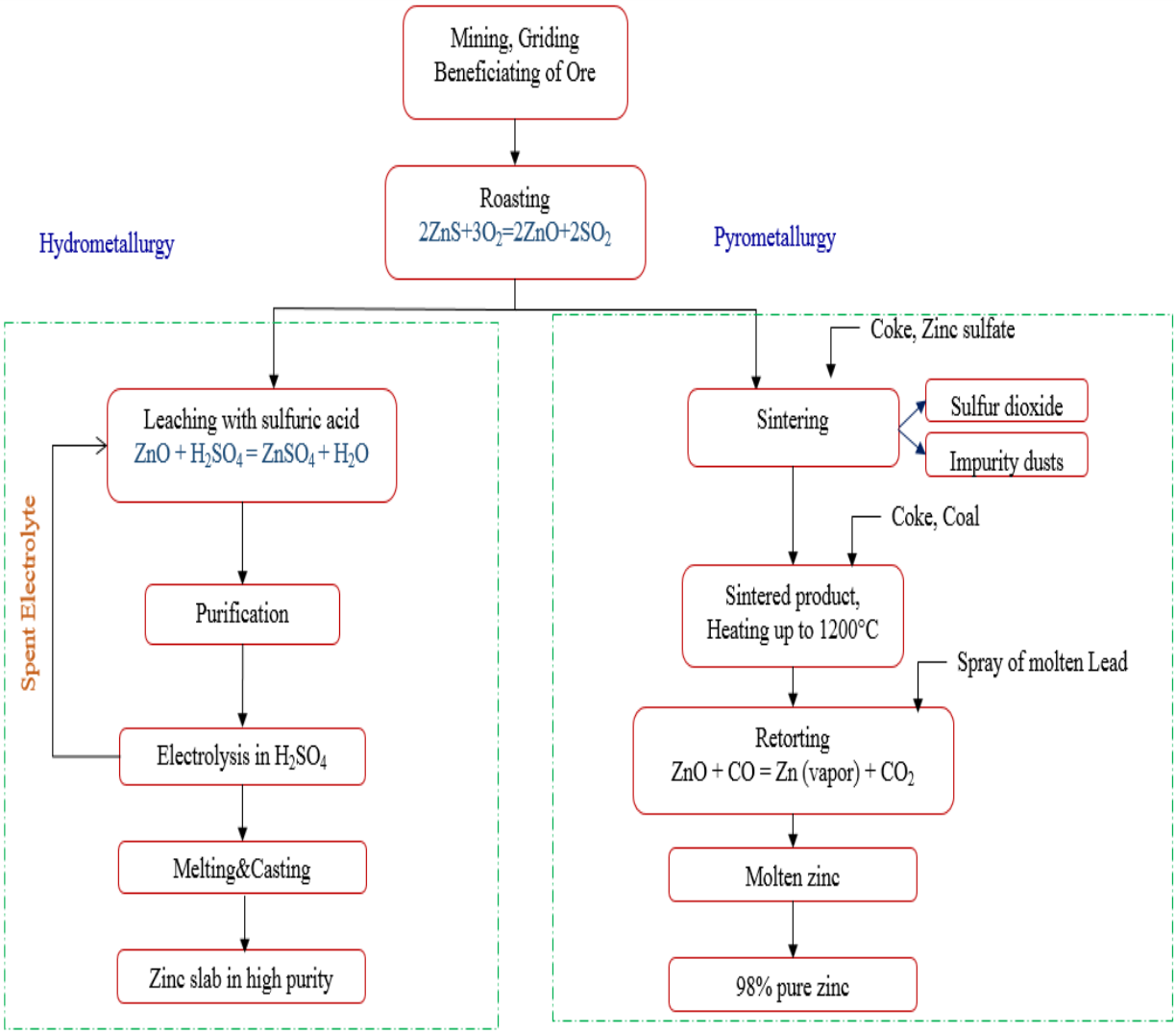

Figure 1.4 Comparison between primary and secondary zinc production

1.2 Introduction to ionic liquids

In searching of a green solvent that can effectively reduce pollutant emissions in Zn production, ionic liquids appear and draw our attention.

1.2.1 Definition of ionic liquids

Ionic liquids are widely recognized as liquid substances that composed only of cation and anion at temperatures below 100°C" **[10]**. An essential property of ionic liquids is that they are liquidus over a wide range of temperature. To distinguish them from molten salts which melt only at elevated temperature, ionic liquids have a low melting point that makes it more promising in energy saving. As ionic liquids developed, the most vital advantages of the liquids are becoming **[11,12]:**

- non measurable vapor pressure
- non-flammable and non-corrosive
- wide electro-chemical window
- thermal stability
- high solubility of metal salts
- high conductivity compared to non-aqueous solvents

1.3.2 Development of ionic liquids

1.3.2.1 First generation of Ionic liquids

The first ionic liquid [$EtNH_3$-NO_3] was initially designed in 1914 to use as a battery electrolyte [**13**]. Later, it has been reinvented by Hurley and Wier in 1948 to explore their application in aluminum electrodeposition **[14**]. It was reported based on $AlCl_3$ in 1980s. Hussey

et al **[15-17]** and Osteryoung et al **[18,19]** did extensive researches on aluminum chloride room temperature ionic liquids and the first review paper of room temperature ionic liquid was written by Hussey **[20]**. The $AlCl_3$ based room temperature ionic liquid was deemed as first generation of ionic liquids. The first breakthrough in the field came along with the full investigation and synthesis of $[C_2mim]Cl - AlCl_3$ ionic liquid system. The phase diagram of this system is investigated by Wilkes et al and is illustrated in Figure 1.5 [**21**]. It is clearly demonstrated that the low viscosity liquid forms at room temperature in an $AlCl_3$ molar ratio from 0.33 to 0.67 [**22-24**]. The unique characteristics of Chloroaluminate (III) system is that the acidity/basicity is totally depending on the mole fraction of $AlCl_3$ (neutral for 50%, acidic for more than 50% and basic for less than 50% of $AlCl_3$). The reaction between $[C_2min]Cl$ and $AlCl_3$ were represented as a serier of equilibria, as given in the following equations:

$$[C_2mim]^+ Cl^- + AlCl_3 \leftrightarrow [C_2mim]^+ [AlCl_4]^- \qquad (1.5)$$

$$[C_2mim]^+ [AlCl_4]^- + AlCl_3 \leftrightarrow [C_2mim]^+ [Al_2Cl_7]^- \qquad (1.6)$$

$$[C_2mim]^+ [Al_2Cl_7]^- + AlCl_3 \leftrightarrow [C_2mim]^+ [Al_3Cl_{10}]^- \qquad (1.7)$$

For a system where $[C_2mim]Cl$ is excess over $AlCl_3$, equilibrium as shown in eq. (1) governs and the ionic liquid is shown basic since the dominant anions are Cl^- and $[AlCl_4]^-$. In contrast, when $AlCl_3$ is in a molar excess over $[C_2mim]Cl$, an acidic ionic liquid forms as equilibrium as shown in eq. (2) and (3) controls. In brief, Chloroaluminate systems are governed by the following primary equilibrium in eq. 1.8, where K is the equilibrium rate constant **[25]**.

$$2[AlCl_4]^- \leftrightarrow [Al_2Cl_7]^- + Cl^- \qquad K = 10^{-16.3} \qquad (1.8)$$

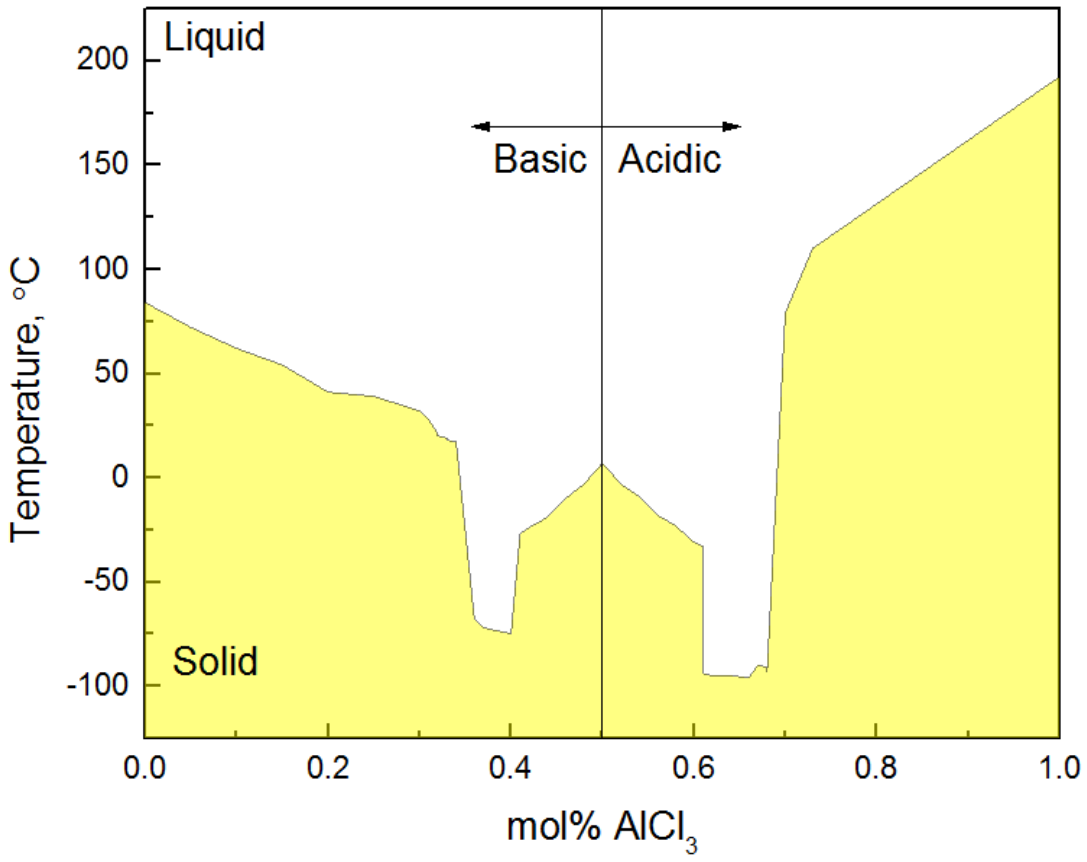

Figure 1.5 Phase diagram of $[C_2min]Cl$-$AlCl_3$ system [**21**]

1.3.2.2 Second generation of ionic liquids

The further use of $AlCl_3$ based ionic liquid in many applications was limited by its hydroscopic nature and as a result, the preparation and synthesis of ionic liquids is only possible under at least dry atmosphere. Air and moisture stable room temperature ionic liquids which are considered to be the second generation of ionic liquid that had attracted attention in application of various fields. The first air and water stable ionic liquid was found by Wilkes and Zaworotko **[26]** in 1992 which is still composed of the same 1-ethyl-3-methylimidazolium (C_2min) cation but contains a wide range of alternative anions, $[C_nmim]X$, where X can be $[CH_3CO_2]$, $[NO_3]$, $[BF_4]$ or $[PF_6]$ anions [**26**]. Unlike $AlCl_3$ based ionic liquids that required to be prepared in dry

atmosphere, this group of ionic liquids can be synthesized and prepared in ambient atmosphere. Figure 1.6 present the electrochemical window of water-free $[Bmim]^+BF_4^-$ on Tungsten wire at 80°C for a scan rate of 50 mv/s. A window as wide as 4 volts can be easily achieved. However, the longtime exposure to air and moisture could generate changes in physical and chemical properties of ionic liquid. In the presence of moisture, tetrafluoroborate and hexafluorophosphate ionic liquids are the least acceptable medium for electrochemistry as the formation of HF could cause decomposition of the ionic liquid as well as hazardous experimental condition. As a consequence, more hydrophobic anions such as trifluoromethanesulfonate $[TfO]^-$, bis{(trifluoromethyl)sulfonyl}amide $[Tf_2N]^-$, and tris{(trifluoromethyl)-sulfonyl}methanide $[Tf_3C]^-$ have been investigated and developed by Gratzel et al **[27,28]**. This group of ionic liquid receives extensive attentions not only due to the high water resistance, but also because of their wide electrochemical window. Table 1.1 below provides a direct comparison of electrochemical windows between water and some typical ionic liquid solvents **[29]**. Over the years that followed, novel types of cations such as phosphonium and pyrrolidinium were developed and it has been recognized that over 1 million ionic liquids could possibly synthesized **[30]**.

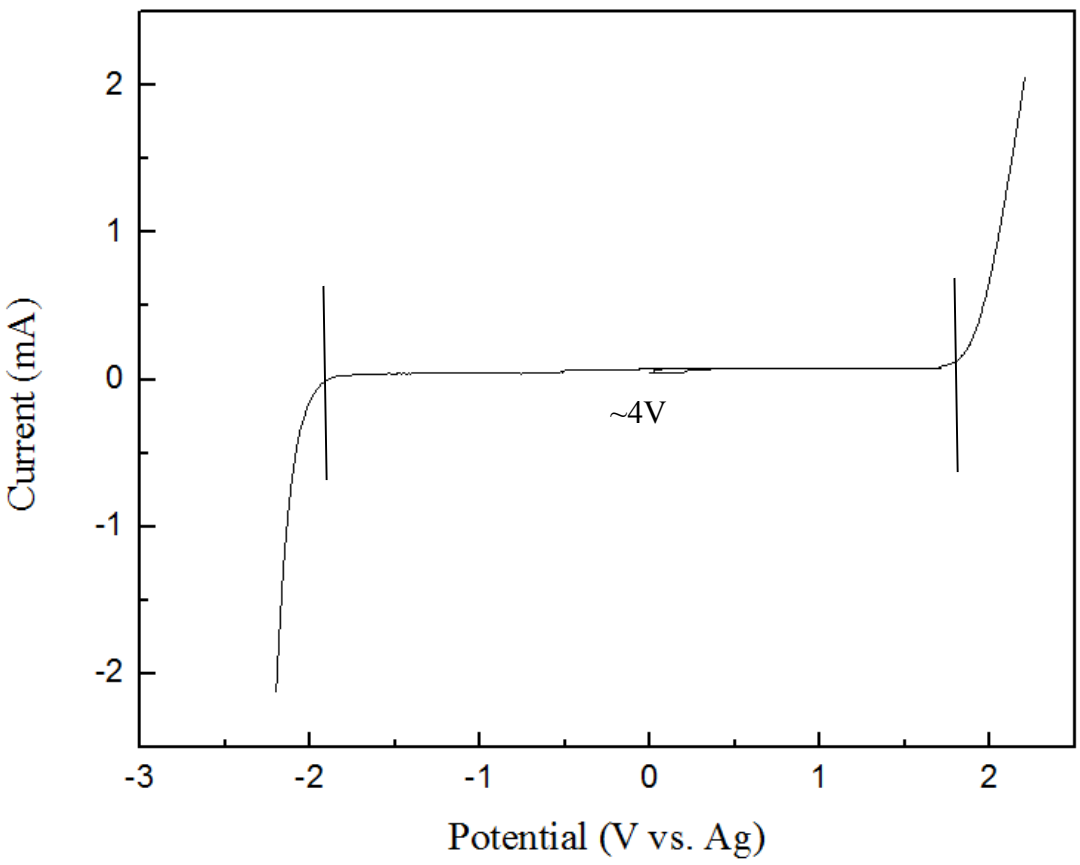

Figure 1.6 Electrochemical window for dry $[Bmim]^{+}BF4^{-}$ ionic liquid on tungsten electrode at a temperature of 80°C for a scan rate of 50 mv/s

Table 1.1 The comparison of electrochemical windows between water and ionic liquid solvents **[29]**

Solvents	Negative End (V vs. SCE)	Positive End (V vs. SCE)
Water	-1.23	+1.23
$[EtNH_3]NO_3$ (first IL)	-0.8	+1.5
$[C_4mim][HSO_4]$	-2.2	+0.5
$[C_4mim][CF_3CO_2]$	-2.2	+0.6
$[C_4mim][H_2PO_4]$	-2.2	+0.7
$[C_4mim][Cl]$	-2.2	+0.9
$[C_4mim][NO_3]$	-2.2	+1.5
$[C_4mim][TfO]$	-2.2	+2
$[C_4mim][BF_4]$	-2.2	+2
$[C_4mim][PF_6]$	-2.2	+2.5

1.2.3 Deep eutectic solvent (DES)

In light of the fast development of ionic liquid, the searching for an ionic liquid with low price and low toxicity is ended with the emergence of a new generation of solvent, named Deep Eutectic Solvents (DES) at the beginning of this century. As its name implies, the formation of DESs can be easily achieved by simply mixing two components where a eutectic mixture forms through hydrogen bond interaction. DESs own many advantages over traditional ionic liquids. Compared to ILs, DESs are (1) much cheaper; (2) non-reactive with water (easy preparation and storage); (3) most of them are biodegradable and biocompatible; and (4) non-toxicity. Because of their economic and ecological foot print, DESs has been selected for a wide range of applications

at both academic and industrial level. Abbott and his coworkers [**31**] reported in 2007 defined DESs can be formed by quaternary ammonium salts of a formula $[R_1R_2R_3R_4N^+]X^-$ with a ligand agent. Four types of DESs can be described in the form listed below:

(1) Anhydrous metal salts (MCl_x), M = Zn, Sn, Fe, Ga [**32,33**];

(2) Hydrated metal salts ($MCl_x \cdot yH_2O$), M = Cr, Co, Cu, Ni, Fe [**34**];

(3) Hydrogen bond donors (HBDs) such as $-CONH_2$, -COOH, -OH [**35,36]**;

(4) $MCl_x \cdot Z$ with Z = urea, ethylene glycol, acetamide [**37**].

Among the candidates, choline chloride (ChCl) has been deemed as the most commonly used component resulting from its cheap price, availability and biodegradability. Upon thorough mixing with safe hydrogen bond donors such as urea (common fertilizer), renewable carboxylic acids (citric, succinic or oxalic acids), or polyols (glycerol, carbohydrates), ChCl is capable of forming a DES easily. This type of DESs exhibits similar physical chemical properties compared to imidazolium-based ILs and moreover, it shows many advantages over traditional organic solvents. Easy storage is the most attractive feature because of their non-volatility and non-flammability. In addition, they are easy to handle and no further purification is required, and therefore, making the large-scale application feasible.

In the following section, an overview of ChCl based DESs in terms of physical-chemical properties will be presented.

1.2.3.1 Freezing point/Phase behavior

One appealing feature of DESs is having low freezing point. For all reported DESs, the freezing points are below 150°C. It can be acknowledged from the hydrogen bond interaction between two solid constituents. For example, the mixture of ChCl (melting temperature is 302°C) and Urea (melting temperature is 133°C) in a molar ratio of 1:2 leads to the major depression of freezing temperature to 12 °C. This depression is brought by an interaction between the Cl^- anion and the hydrogen bond donor component (in this case, urea). Freezing temperature of six typical ChCl based eutectic electrolytes are compared in Table 1.2 and corresponding phase analysis is shown in Figure 1.7 [**36, 37**]. Because of the difference in the ability to form hydrogen bond with ChCl, freezing point and molar ratio varies when different HBDs are selected, as shown in Table 1.2. Similar to urea, Phenylpropionic and Phenylacetic acid present the eutectic molar ratio with ChCl in 2:1, which means for each Ch^-, two carboxylic acid molecules are required to form eutectics. In the case of dicarboxylic acid, such as oxalic, malonic or succinic acid, the eutectic composition with ChCl is at 50% of acid (1:1 in molar ratio), further verified that two carboxylic acid molecules is needed to complex with Cl^-. Although a significant depression in freezing point can be seen, there is no clear correlation established between melting point of the single components and freezing point of the DESs.

Table 1.2 Freezing temperature of ChCl/acid deep eutectic solvents [**36, 37**]

Acid	Freezing point (°C)	Molar ratio
Urea	12	1:2
Phenylpropionic	21	1:2
Phenylacetic	25	1:2
Oxalic	31	1:1
Malonic	12	1:1
Succinic	71	1:1

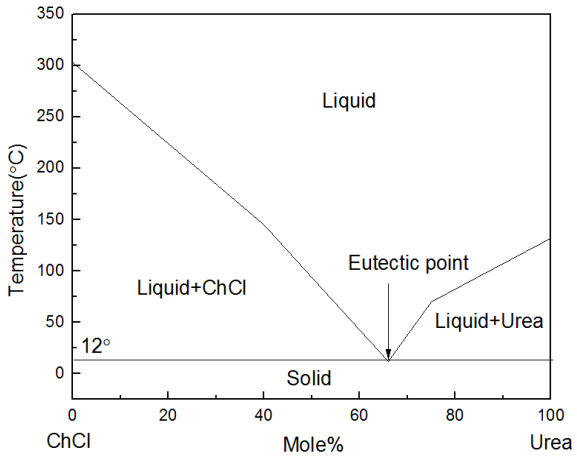

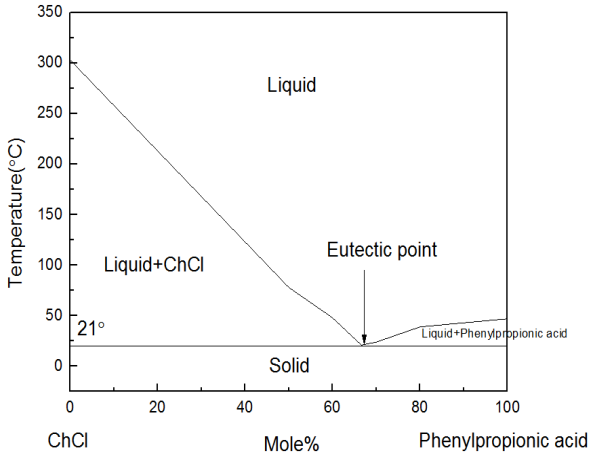

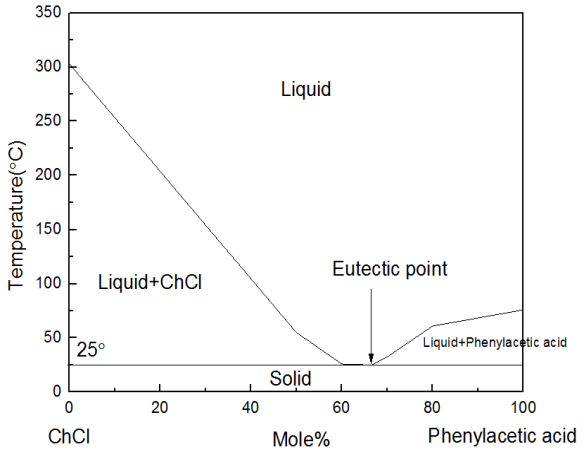

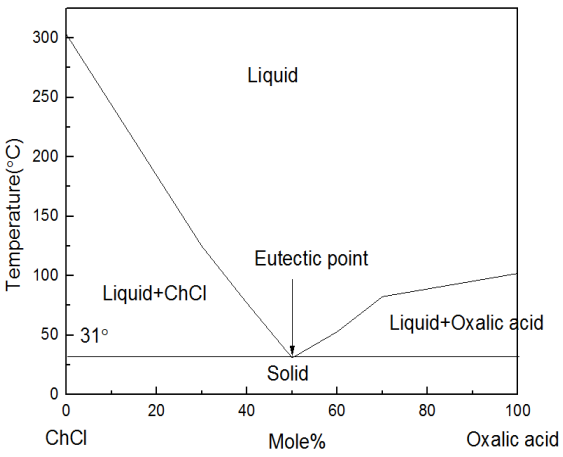

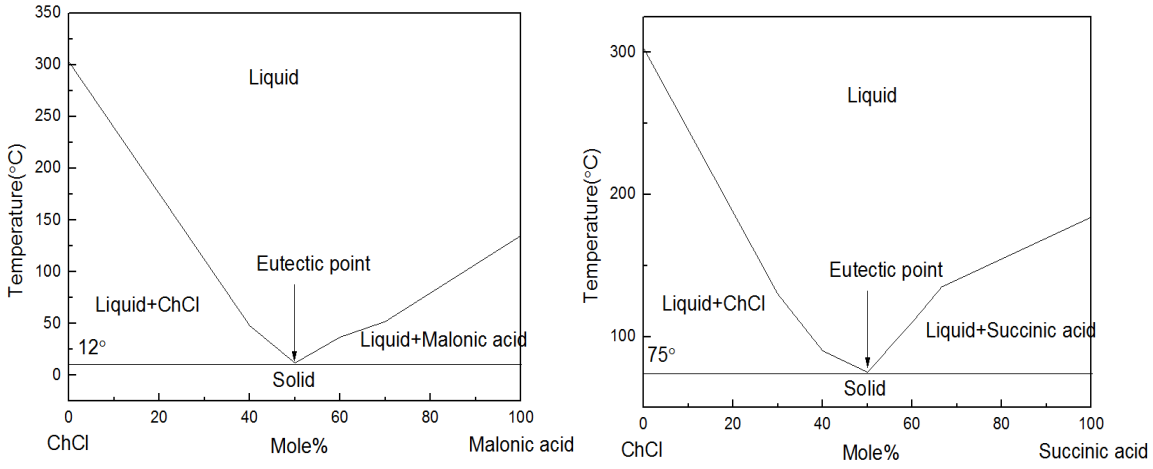

Figure 1.7 Phase behavior and eutectic point determination of (a) ChCl/Urea; (b) ChCl/Phenylpropionic acid; (c) ChCl/Phenylacetic acid; (d) ChCl/Oxalic acid; (e) ChCl/Malonic acid; (f) ChCl/Succinic acid ionic liquid eutectic electrolytes [**36**]

1.2.3.2 Density

Density is a vital property for characterization of ionic liquid and is a necessity in thermodynamic computational modeling and technological design. Density of four types of ChCl based DESs are measured in the literature, as recorded in Table 1.3 **[38]**. All DESs show densities higher than water. However, the selection of different HBDs leads to variation in the density, and this can be ascribed to difference in packing structure as well as the molecular organization.

Table 1.3 Density measurement of ChCl based DESs at 25°C [**38**]

ILs	Molar ratio	Density (g/cm^3)
ChCl/Urea	1:2	1.25
ChCl/Malonic acid	1:1	1.25
ChCl/ethylene glycol	1:2	1.12
ChCl/oxalic acid	1:1	1.133

1.2.3.3 Viscosity

Viscosity is vital parameter that has major impact on all application of ionic liquids, such as electrolytic process. The viscosity measurement for ChCl based DESs is recorded in Table 1.4 [**39**,**40**]. As seen, except for ChCl/EG, most of DESs present relatively large viscosity at room temperature (larger than 100 cP). It can be attributed to the existence of intensive hydrogen bond interaction between components, which leads to lower mobility of species. Viscosity exert considerable influence on the course of chemical reactions (high viscosity is the cause for low reaction rate), and thus, DESs with lower viscosity is preferable in engineering applications.

Table 1.4 Viscosity measurement of ChCl based DESs **[39, 40]**

ILs	Molar ratio	Viscosity (cP)
ChCl/Urea	1:2	750 (25°C)
ChCl/Malonic acid	1:1	1124 (25°C)
ChCl/ethylene glycol	1:2	37 (25°C)
ChCl/oxalic acid	1:1	120 (30°C)

1.2.3.4 Electrical Conductivity

For the selection of a good electrolyte, electrical conductivity is a parameter that needs to take into consideration. Because of the high viscosity that most DESs presented, conductivity is shown to be relatively low. Table 1.5 records conductivity measurement of ChCl based DESs at various temperatures [**36, 38**]. All DESs that under investigation exhibit electrical conductivity below 10 mS/cm at temperature below 40°C. This is due to reduced ion mobility involved in high viscous liquid.

Table 1.5 Electrical conductivity measurement of ChCl based DESs **[36, 38]**

ILs	Molar ratio	Conductivity (mS/cm)
ChCl/Urea	1:2	0.199 (40°C)
ChCl/Malonic acid	1:1	~8 (25°C)
ChCl/ethylene glycol	1:2	7.61 (20°C)
ChCl/oxalic acid	1:1	5 (30°C)

1.2.3.5 Molar heat capacity

Molar heat capacity is one of the most important properties required to evaluate the suitability as a solvent for heat transfer applications. Table 1.6 compares the molar heat capacity of three most commonly used DESs, namely ChCl/Urea, ChCl/Ethylene glycol, and ChCl/Glycerol in a molar ratio of 1:2 at temperatures from 30 to 80°C [**41**]. They all exhibit higher heat capacities compared to water which is attributed to the higher molar mass of DESs. Similarly, the C_p values follows the order that ChCl/Urea < ChCl/Ethylene glycol< ChCl/Glycerol which is because of the difference in molar mass as well. It is expected that higher heat capacity achieved with larger molar mass since C_p is associated with the number of translational, vibrational, and rotational energy storage modes in the molecule [**42**].

Table 1.6 Molar heat capacities of DESs in a molar ratio of 1:2

T (°C)	Molar heat capacity, Cp (J mol^{-1} K^{-1})		
	ChCl/Urea	ChCl/EG	ChCl/Glycerol
30	181.4±0.5	190.8±0.4	237.7±0.6
35	182.2±0.6	192.2±0.3	239.1±0.5
40	183.2±0.5	194±0.3	240.8±0.4
45	183.5±0.5	194.9±0.4	241.9±0.2
50	184.5±0.6	196.4±0.2	243.5±0.4
55	185.3±0.6	197.6±0.2	244.9±0.1
60	186.4±0.6	199.2±0.3	246.9±0.1
65	187.4±0.5	200.6±0.3	248.4±0.4
70	188.5±0.7	202.1±0.1	250.3±0.3
75	189.5±0.6	203.9±0.2	252.1±0.3
80	190.8±0.8	205.6±0.2	254.3±0.4

1.2.3.6 Solubility of metal oxides

Metal salt solubility an in ionic liquid is very important for the electrodeposition process. The weak coordination between anions and cations in IL results in salvation energy that is not enough to break the electrostatic interactions between ions or between metallic atoms from the metal compounds. It is then to be expected poor metal or metal compound solubility in ILs. However, a good solubility of some of metal oxides is found for ChCl based DESs due to the capability of donating and accepting electrons to form hydrogen bonds. Table 1.7 shows the solubility of a wide variety of metal oxides in 2:1 Urea/ChCl eutectic mixture at a temperature of 60°C [**43**]. Oxides such as ZnO, CuO, and PbO_2 show great solubility while CaO and Al_2O_3 both show poor solubility. Metal oxides solubility in high temperature molten salts can be well compared to deep eutectic system. The solubility for ZnO, NiO, Cu_2O reported in NaCl-KCl

system are 27.6, 2.3, 1216ppm [**44]** which are lower than those in room temperature ionic liquids. In high temperature molten salts, the solubility of metal oxides is controlled by a mechanism in which naked metal ions separate from oxygen ions and can be demonstrated as $MO \rightarrow M^{2+} + O^{2-}$. However, in DES system, it is proposed that high solubility of transition metals is mainly due to the ability to complex with a ligand agent, in this case urea, thus increasing surface area that interacts with solvents. A formula of $[MO{\cdot}nCl{\cdot}urea]^{n-}$ is proposed as soluble form in urea and choline chloride mixture. Its capability to selectively dissolve metal oxides (ZnO and PbO_2) present great potential in recovery of Zn, and Pb from steelmaking slags produced from electric arc furnace (EAF).

Table 1.7 Solubility of metal oxide in 2:1 molar ratio of Urea and ChCl in a temperature of 60ºC determined by ICP-AES

Metal Oxide	Solubility/ppm
ZnO	8466
Cu_2O	8725
CuO	470
PbO_2	9157
Al_2O_3	<1
MnO_2	493
Fe_2O_3	49
Fe_3O_4	40
NiO	325
CaO	6

1.2.4 Applications of ionic liquids

The use of ionic liquids in a wide variety of applications has recently gathered attention. It is reported that imidazolium cation based ionic liquids can be used as lubricant or surfactant

additives [**45**], in organic synthesis and catalytic reactions [**46,47**], or mobile phase additives in liquid chromatography [**48].** Chengfeng Ye et al proposed that the dipole structure of ionic liquid enables it to be easily absorbed on the interface of electrode-electrolyte thus forming effective smooth boundary layer that reduces friction and produces finer deposit surface morphology **[49]**. Qibo Zhang et al reported that 1-butyl-3-methylimidazolium hydrogen sulfate ([BMIM]HSO_4) has a significant effect on the process of zinc electrodeposition in sulfuric acid electrolyte [**50**]. In order to improve the quality of deposited layer, [BMIM]HSO_4 has been used as additive agent to investigate if it can work as an equally efficient additive agent in ChCl/Urea deep eutectic solvent.

1.3 Electrodepositon of Zn in DESs

Due to the significant solubility of ZnO in DESs, particularly in 2:1 Urea/ChCl eutectic mixture, DESs are considered to be a potential candidate to serve as an alternative green solvent for sulfuric acid. Electrodeposition of zinc involves:

(1) Dissolution of pure zinc oxide (ZnO) in the studied electrolyte;

(2) Deposition of conductive metal from an electrolytic solution by the application of an electric current or potential.

In recent years, it has been reported that zinc can be obtained in 2:1 EG/ChCl via electrodeposition [**51**]. However, the morphology has shown variation and has been proved to be controlled by experimental conditions, such as deposition over-potential, current density, temperature and concentration of the additives. Zinc morphology can be categorized primarily in three types [**52**]:

(a) Compact;

(b) Spongy, granular etc;

(c) Dendritic

They are mostly related to the deposition current density as well as over-potentials. Dendrites forms at non-equilibrium condition which requires the largest over-potential. Spongy or granular type morphology forms at intermediate over-potential. Compact type of deposit forms at equilibrium condition and thus requires the least amount of over-potential. Dendritic deposition which is commonly observed during the electrodeposition process is not preferable as it hinders the process in many aspects mentioned in the earlier chapters. Therefore, dendritic free zinc electrodeposition is the main concentration in this work in order to ensure smooth, economic and efficient operation.

1.3.1 Reasons for dendritic formation

The morphology of zinc deposit largely depends on process parameters. Table 1.8 shows the effect of experimental process parameters on dendritic formation [**53**].

Table 1.8 Effect of experimental process parameters on dendritic formation [**53**]

Experimental Parameters	Effect on Dendritic formation
Additives	To prevent dendritic formation by decreasing viscosity of the electrolyte
Temperature	Dendritic formation prohibited at higher temperature
Electrolyte Stirring	Dendritic formation prohibited as increasing stirring rate
Deposition Time	Dendritic formation enhanced as increasing deposition time
Impurities	Dendritic formation prohibited with the presence of impurities
Substrate Material Surface Treatment	Dendritic formation enhanced as Surface roughness, oxidation and contamination existed

Dendritic formation can be explained in the sequence discussed as follows. B.N. Pal **[54]** reported that (0001) crystal plane is parallel to the substrate and there exists a preferred growth direction which is normal to the crystal plane. Zn forms as hexagonal closed packed (hcp) crystalline structure and for each basal plane, there are six crystallographic directions that are perpendicular to it, as shown in Figure 1.8. At the influence of the electric field, the growth along one specific direction initiates and forms a needle in that direction. As the first dendrite growing, the growth along two crystallographically equivalent directions leads to the formation of symmetric branches on both sides, and eventually interconnected and forming a dendritic structure, as seen in Figure 1.9.

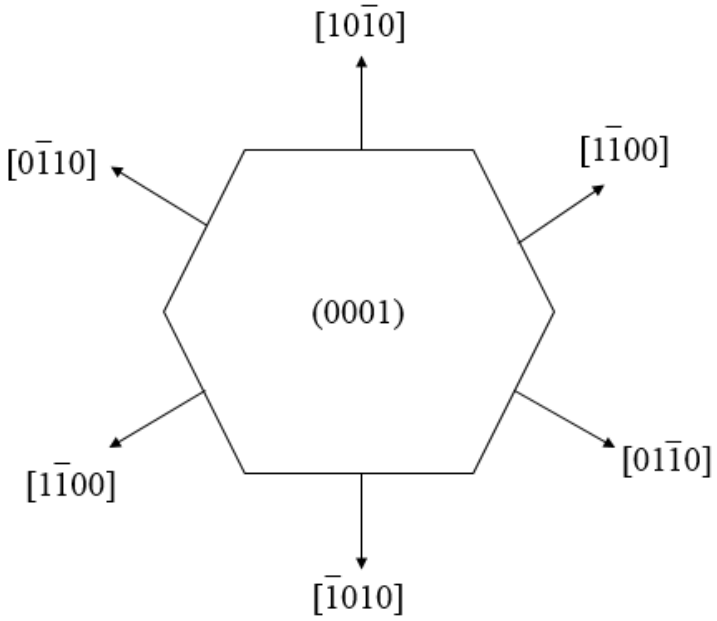

Figure 1.8 Schematic representation of the six crystallographically equivalent directions of hcp zinc

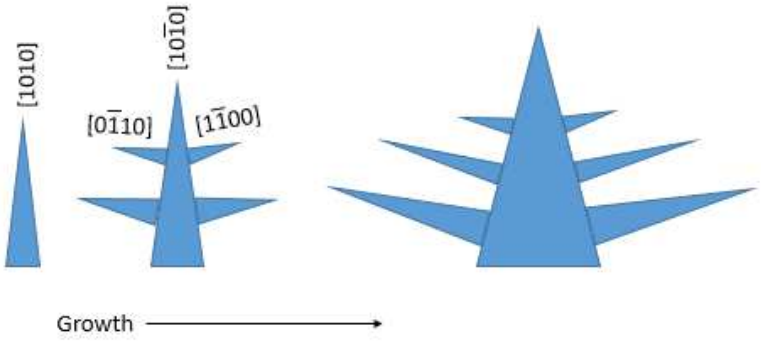

Figure 1.9 Schematic representation of development of zinc dendritic structure from a single zinc crystal from the growth in the fast growing directions [**54]**

The initiation of dendritic growth is largely depended on cathodic current density and over-potential. It is of vital importance to derive an equation to calculate critical over-potential which is a kinetic parameter to determine dendritic growth. The condition for initiation of dendritic growth is expressed as follows **[55]:**

$$i_L \leq i_o \frac{h}{\delta} \cdot f_{crt} \tag{1.9}$$

Where i_L is the limiting cathodic current density (A/m^2), h is the height of the growing dendrite (m), δ is the diffusion boundary layer thickness (m), and f_{crt} corresponds to critical over-potential, which can be expressed as eq 1.10:

$$f_{crt} = \exp(\frac{-nF\eta}{RT}) \tag{1.10}$$

Based on Butler-Volmer equation, when the electrode process is diffusion controlled, in the limiting current region, the value of current density can be expressed in eq. 1.11:

$$i_L = \frac{nFDC}{\delta} \tag{1.11}$$

Where n is the number of transferred electrons, D is diffusion coefficient, F is the Faraday constant, and C is the bulk concentration of electro-active species. Combining eq. (1.9) and (1.10) yields the expression of critical over-potential (η_{crt}) which is expressed in eq. (1.12):

$$\eta_{crt} = \frac{RT}{nF} ln \left(\frac{i_L \delta}{i_o h}\right) \tag{1.12}$$

The minimum required over-potential for dendrite formation can be determined when the height of the growing dendrite (h) is equal to the diffusion boundary layer thickness (δ) and is given by eq. (1.13):

$$\eta_{crt} = \frac{RT}{nF} ln \left(\frac{i_L}{i_o}\right) \tag{1.13}$$

This expression obviously indicates that critical over-potential is related to temperature, diffusion coefficient of the solvent, concentration of the electro-active species and number of transferred electrons. The chances of dendritic deposition will be reduced when higher critical over-potential is needed in a given system.

CHAPTER 2

RESEARCH OBJECTIVES

The aim of the present research is to thoroughly investigate zinc electrowinning process in lab-scale and to focus on the optimization of experimental parameters in order to develop a general applicable environmental-friendly methodology for zinc electrowinning of large scale in low temperature ionic liquid electrolytes. Although sulfate electrolytic process has been commercially used in industrial metal extraction process for a long time, we are trying to develop a novel pathway for metal deposition that produces much less harmful gases such as CO, CO_2 or SO_2 and maintains high current utilization as well. Parameters in the process of electrodeposition of metal are discussed for optimizing the experimental outcomes and investigating their effect on the deposit. The main objectives of the present research are listed below:

1. To synthesize in large scale of Urea/ChCl eutectic mixture in a molar ratio of 2:1 at low temperature.
2. To characterize Urea/ChCl deep eutectic solvent in a molar ratio of 2:1
3. To develop and investigate electrochemical behavior of Zn electrodeposition in low temperature ionic liquid electrolytes.
4. To investigate the zinc electrowinning process in terms of kinetic parameters, effect of applied voltage on surface morphology, current efficiency and energy consumption.

5. To optimize experimental parameters such as concentration of additive, temperature, and applied cell voltage for high yielding process, and better surface morphology as well.
6. To design and model a recycling electrochemical cell in order to scale up laboratory based zinc electrowinning process.

These objectives are determined through systematic experimentation and comprehensive analysis of the process. Detailed results will be discussed in the following chapters.

CHAPTER 3

EXPERIMENTAL PROCEDURE

3.1 Preparation of Chemicals

3.1.1 Synthesis of Ionic Liquid

Ionic liquids (eutectic mixture of 2:1 urea and choline chloride) were synthesized in our laboratory, by following the procedure reported in the literature [**56**]. Choline chloride and urea were dried and keep for 2 hours prior to use. Pyrex glassware used in synthesis and experimental process is purchasing from Fisher Scientific Company. The flow sheet illustrated the synthesis procedure of 2:1 urea and choline chloride ionic liquid can be seen in Figure 3.1. The electrolyte was prepared by heating urea ($CO(NH_2)_2$) (Alfa Aesar 99.3%) and choline chloride ($C_5H_{14}ClNO$) (ChCl) (Alfa Aesar 98%) in a molar ratio of 2:1 at 90ºC for 12 hours with constant stirring. A clear homogeneous solution was obtained, as seen in Figure 3.2.

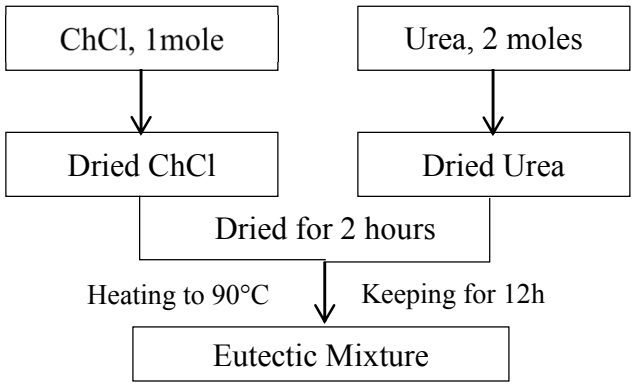

Figure 3.1 Flow sheet for synthesis of urea and choline chloride ionic liquid

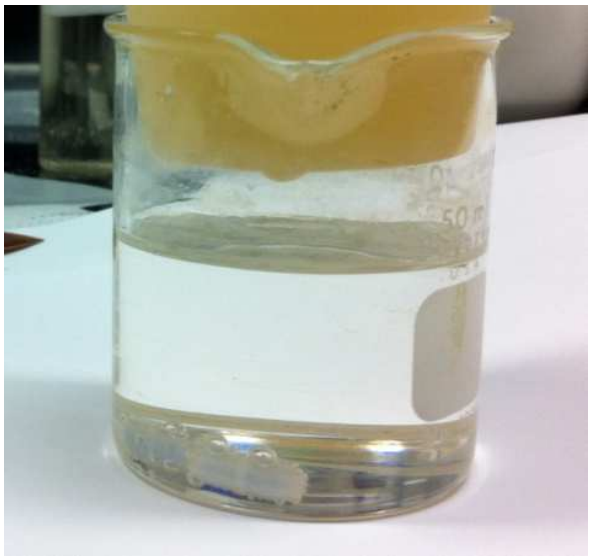

Figure 3.2 Clear homogeneous solution formed by mixing Urea/ChCl in a molar ratio of 2:1

3.1.2 Preparation of Materials

Zinc oxide used in the present experiments was purchasing from Fisher Scientific (certified ACS, ≥99.0%). For the purpose of investigating the effect of 1-Butyl-3-methylimidazolium hydrogen sulfate ($[BMIM]^+HSO_4^-$) as an novel ionic additive (Sigma Aldrich ≥ 95%) on zinc electrodeposits morphology, $[BMIM]^+HSO_4^-$ in a purity of 95% was purchased from Sigma Aldrich. The experiments were conducted in a controlled atmosphere glove box to eliminate the influence of moisture. The zinc compound were dried at a temperature of 50°C kept for 3 hours before all measurements. The specifications for the purchased ZnO is shown in Table 3.1.

Table 3.1 ZnO product specifications

ZnO	99.0% min.
Calcium [Ca]	0.005% max.
Iron [Fe]	0.001% max.
Magnesium [Mg]	0.005% max.
Manganese [Mn]	5ppm max.
Nitrate	0.003% max.
Potassium [K]	0.01% max.
Sodium [Na]	0.05% max.
Lead [Pb]	0.005% max.
Chloride	0.001% max.
Insoluble in Sulfuric Acid	0.01% max.
Sulfur Compounds	0.01% max.

3.2 Experimental Methodology

3.2.1 Dissolution Analysis of Zinc Oxides in Studied Ionic Liquid

Dried metal oxides were mixed with synthesized 2:1 urea/choline chloride ionic liquid in different experimental temperatures. A magnetic stirrer was inserted into the solution for proper mixing. Dissolution time was controlled in 24 hours for the completion of the process.

3.2.1.1 Fourier Transform Infrared Spectroscopy (FTIR)

When a colorless, homogeneous solution formed, the dissolution analysis was carried out by using Fourier Transform Infrared Spectroscopy (FTIR), model Perkin Elmer spectrum 400 (showed in Figure 3.3a). In schematic instrument which is showed in Figure 3.3b, all source radiations pass through a beamsplitter, sent the lights in two directions at right angles. One beam goes to a stationary mirror and the other one goes to the moving mirror. When two beams meet up again at the beamsplitter, they recombine and create constructive and destructive interference (also

called interferogram) due to the difference in path length. The recombined beams then pass through the sample and the sample absorbs all the different wavelengths characteristic of its spectrum. By subtracting specific wavelengths from the interferogram, the detector reports variation in energy versus time for all wavelengths simultaneously. A mathematical function called Fourier transform can convert intensity vs. time spectrum into intensity vs. frequency spectrum.

(a)

(b)

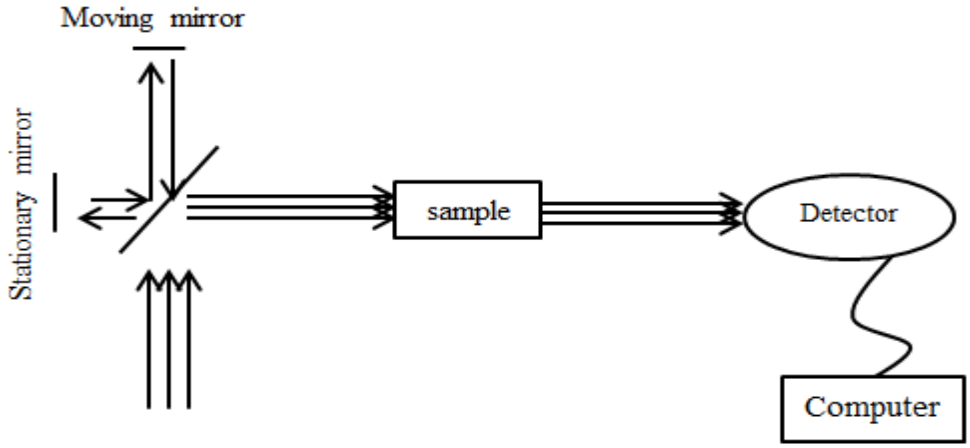

Figure 3.3 (a) picture of FTIR model Perkin Elmer spectrum 400; (b) Schematic FT instrument

The absorbance was plotted in a function of wavelength in spectrum software. The instrument has been calibrated and the background scan can be seen in Figure 3.4.

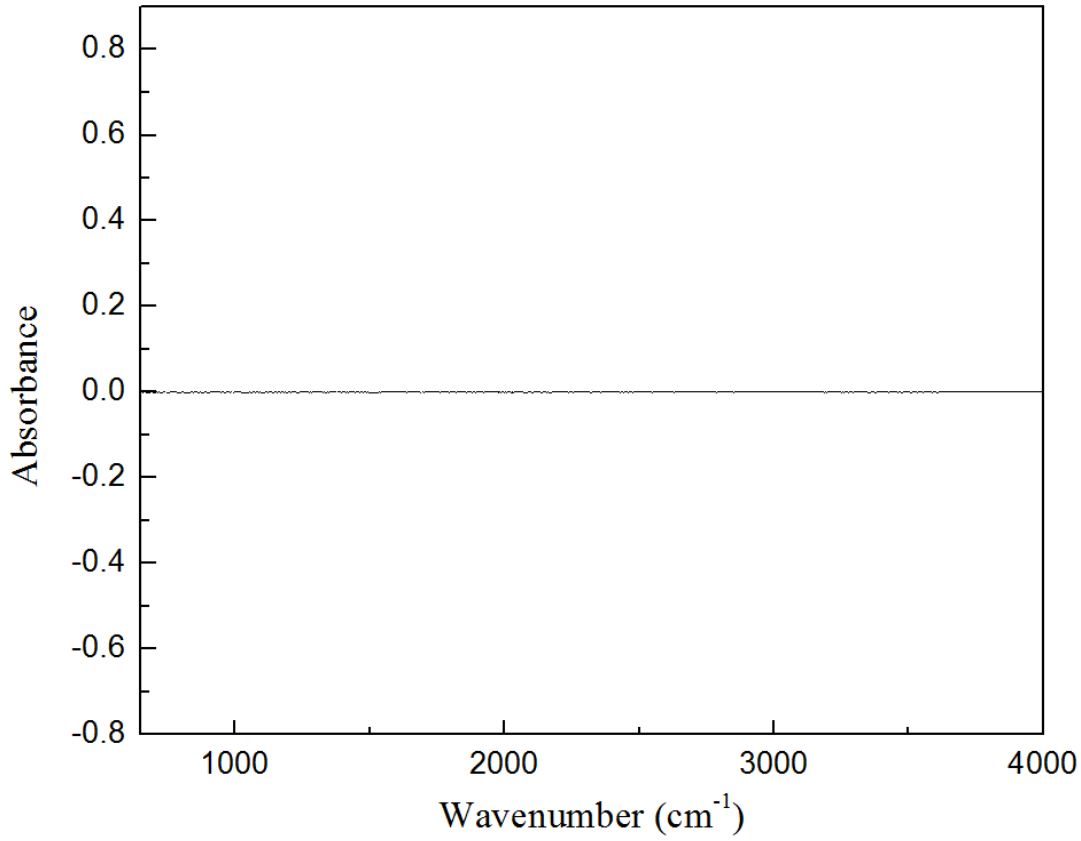

Figure 3.4 FTIR background scan for calibration of instrument

3.2.1.2 Inductively Coupled Plasma Atomic Emission Spectroscopy (ICP-AES)

While FTIR analysis study the comparative dissolution at each condition, ICP-AES is commonly utilized to quantitatively measure the concentration of metal element. ZnO dissolved deep eutectic solution is firstly converted to an aerosol using a nebulizer and is then sprayed into the center of the plasma. The sample is excited, emitting light characteristic of each element. A diffraction grating was used to separate the element wavelengths onto photomultiplier detectors. The amount of light on a given wavelength is proportional to the concentration of the corresponding element in the solution poured to the instrument.

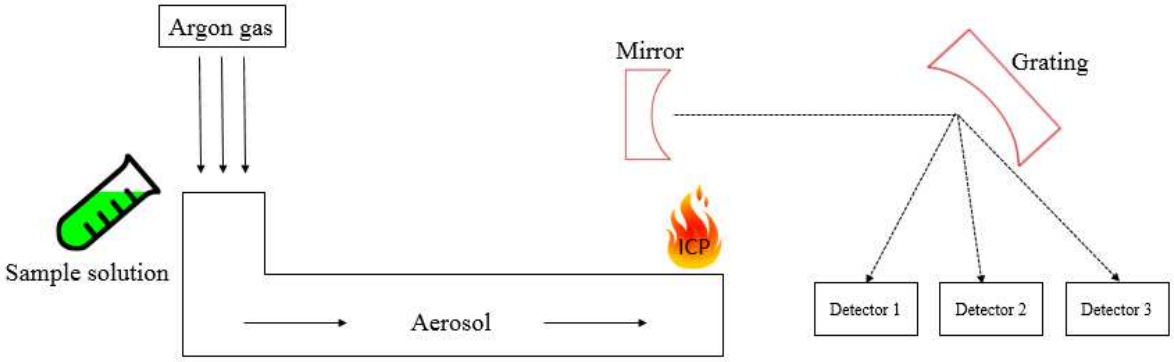

Figure 3.5 Schematic of Inductively Coupled Plasma Atomic Emission Spectroscopy

3.2.2 Electrochemical Measurements

The electrochemical experiments were carried out by using EG&G PAR model 273A potentiostat /galvanostat. This instrument was controlled with a desktop computer using Power Suite software from Princeton Applied Research [**57-60**]. Controlled-potential methods, namely, cyclic voltammetry (CV) and chronoamperometry (CA) are being used in this experiment to characterize the ionic liquid as well as investigate the behavior of electrolyte at electrode surface. To be specific, CV is used to determine the reversible nature of the electrode reactions and CA is useful for studying the kinetics and diffusion/ nucleation mechanism.

Basically, controlled-potential methods measure the current response for oxidation or reduction reaction of the electrochemical active species as a function of applied potential. The rate of mass transfer of species to the electrode is a measurement of current response. Three forms of mass transfers that govern the current response in electrodes reaction: (1) electromigration, (2) diffusion, and (3) convection. The combined effect can be described in Nerst-Planck equation [**61**], as showed in Eq. 3.1:

$$J(x,t) = -\frac{nFDC^*}{RT}\frac{\delta\phi(x,t)}{\delta x} - D\frac{\delta C(x,t)}{\delta x} + C^* v(x,t) \qquad (3.1)$$

Where J(x,t) is the flux of the species at a distance x from the electrode surface, D is diffusion coefficient C^* is the concentration of the species, potential gradient $\frac{\delta\phi(x,t)}{\delta x}$ is the migration component, concentration gradient $\frac{\delta C(x,t)}{\delta x}$ is the diffusion component and v(x,t) is the convection component.

Typically, cyclic voltammetry and chronoamperometry are based on the diffusion of electro-active species to the electrode surface in an unstirred and convection-free solution, thus the effect of migration and convection are undesirable. In experiments of cyclic voltammetry and chronoamperometry, a concentration gradient between electrode surface and bulk solution was created during electrolysis. The current response can be directly related to diffusion component $\frac{\delta C(x,t)}{\delta x}$ which is showed in eq. 3.2

$$i = nFAD(\delta C(x,t)/\delta x) \qquad (3.2)$$

3.2.1.1 Cyclic Voltammetry

Cyclic voltammetry is a potential sweep method where a stationary planar disk working electrode is placed in an unstirred solution. An initial potential (E_i) is set for working electrode, where the electro-active species are not yet electrolyzed. The potential of the electrode then change in a constant rate which is known as scan rate, v (mV/s). This process is called linear sweep. The potential is linearly changing to a potential called switching potential (E_λ), where the linear sweep is reversed and then potential is scanned in an opposite direction until it goes back to E_i (Figure 3.6a).

The potential range between (E_i) and (E_λ) depends on the electrochemical window of the liquid during which all possible electrochemical reactions would be observed. Typically, for electro-active species that are solvated in both reduction and oxidation form, the current response for the forward sweep almost appears symmetry to reverse potential sweep, as described in Figure 3.6b. However, the shape of cyclic voltammetry is quite different for electrodeposition of metals, shown in 3.6c.

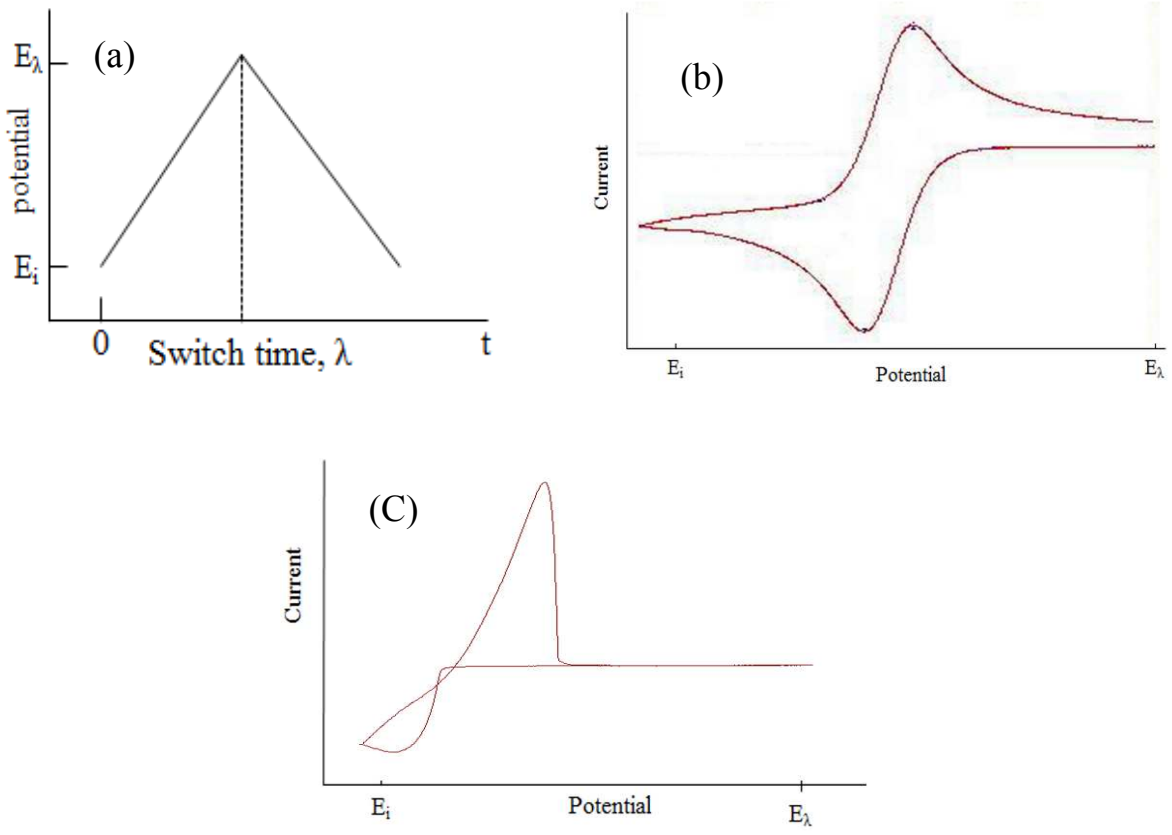

Figure 3.6 Schematic diagram of a typical cyclic voltammetry: (a) typical potential sweep program (b) current responses for a freely diffusing electrochemical couple; (c) current response for the electrodeposition and stripping of a metal

3.2.1.2 Chronoamperometry

Chronoamperometry is a potential step method in which potential is stepping from a starting potential (E_1) where no faradaic process occur to a more negative potential (E_2), where the

kinetics of reduction/oxidation is considerably high that E_2 can be deemed to be in mass-transfer-limited region. During the electrodeposition process, current is generated from reduction of M^{n+} to M on the electrode surface. The diffusion layer is the region of solution depleted of M^{n+} relative to the bulk solution, and the thickness of layer is δx. At the beginning of the process, the concentration gradient, $\frac{\delta C(x,t)}{\delta x}$, is large and thickness δx is small. With increasing time, the diffusion layer thickness increases and concentration gradient decreases due to the diffusion and reduction of M^{n+} at the working electrode. The current response is proportional to concentration gradient as we discussed in eq. 3.2; therefore, current decreases with passing time. For a linear diffusion to a planar disk electrode, the current response as a function of time is given in Cottrell equation [**62**]:

$$I = nFAC(D/\pi)^{1/2}t^{-1/2} \qquad (3.3)$$

Where I is current, A is real surface area of electrode, D and C are diffusion coefficient and concentration of the bulk solution respectively, F is Faraday's constant, n is the charge number and t is the time.

The potential program used to carry out chronoamperometry along with graphical waveform of concentration profile and plot of current as a function time is described in Figure 3.7.

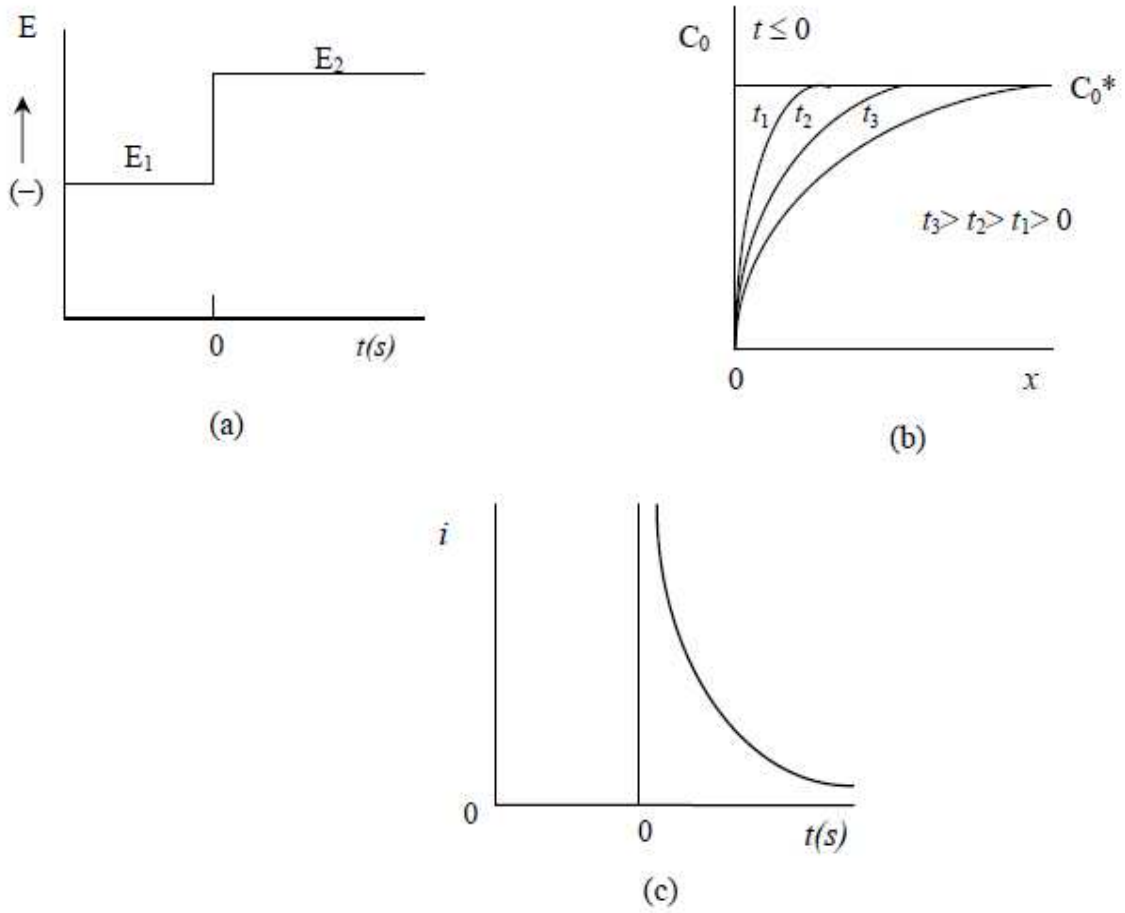

Figure 3.7(a) potential variation as a function of time; (b) simulated concentration profile at different times; and (c) current as a function of time

However in the electrodeposition of metals, the nucleation process causes deviation from Cottrell behavior. Figure 3.8a shows a typical current time transient for a potential step observed during a nucleation involved electrodeposition process. Immediately after applying potential pulse, a small current flow is observed due to the double layer charge. The charging current is then followed by a steady increasing current which is the result of nucleation. During the nucleation process, diffusion occurs in multiple hemispherical fields surrounding the growing crystalline. Current eventually reaches its limit i_m at t_m, because individual diffusion zones of the growing crystalline coalesce. Both i_m and t_m are related to applied potential. After reaching i_m, the current

begins to decrease and decaying with $t^{-1/2}$ which is expected for the linear diffusion to a planar surface described in Cottrell Equation. Figure 3.8(b) [**63**] schematically described the nucleation process and illustrates how the change in the diffusion from hemispherical to planar occurs when hemispherical diffusion zones begin to overlap.

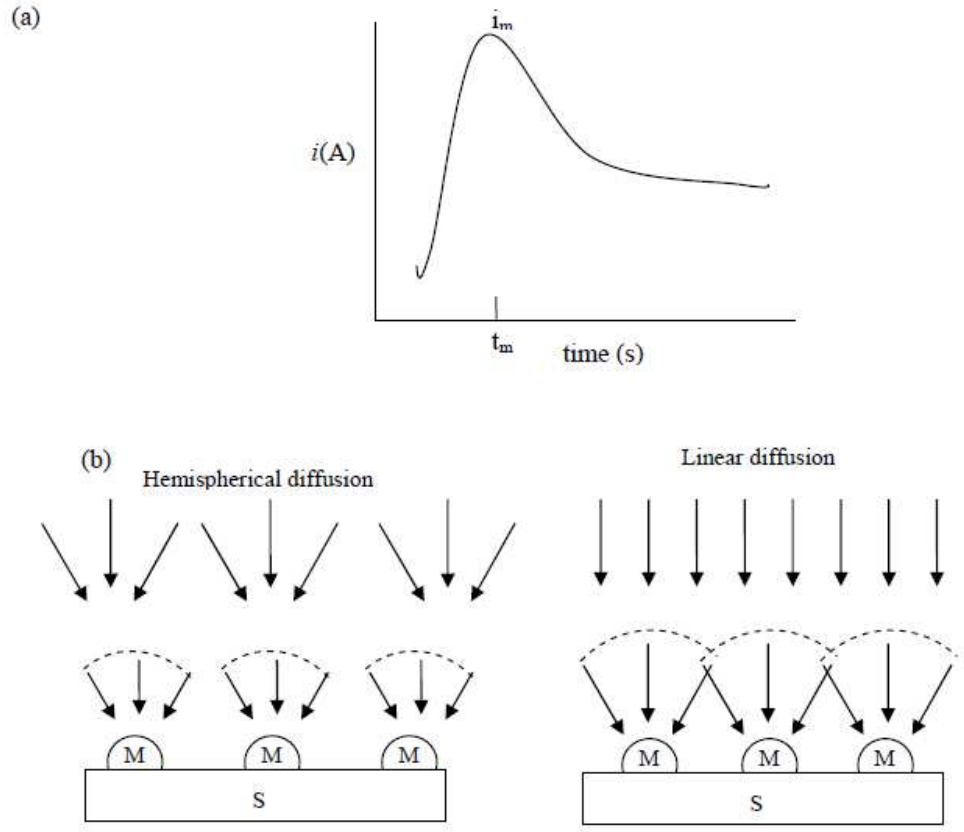

Figure 3.8(a) Typical current responses as a function of time; (b) schematic of nuclei growth demonstration overlapping of hemispherical diffusion zones causing linear diffusion to electrode

3.3 Experimental Set-up

3.3.1 Electrochemical Cell

Cyclic voltammograms and chronoamperometry investigations for zinc oxide dissolved deep eutectic solvent were performed using a three electrode system which has a platinum wire

(0.004 in diameters, Alfa Aesar) as counter, silver wire (0.004 in diameters) as reference and tungsten wire (0.019 in diameters) as working electrode. The electrochemical measurements were carried out using EG&G PARC model 273 A potentiostat/galvanostat. The instrument was controlled by a desktop computer using Power Suite software (Princeton Applied Research). Figure 3.9 and 3.10 show the schematic setup and actual photograph for the setup of electrochemical measurements.

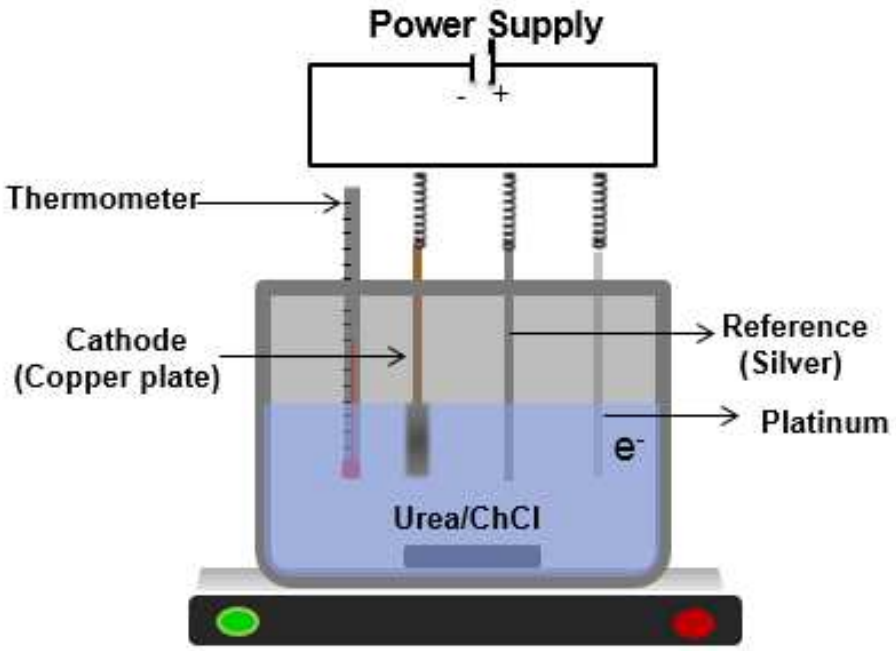

Figure 3.9 Schematic electrochemical measurement setup

3.3.2 Lab-scale Electrowinning Cell

Lab-scale zinc electrowinning process was performed in the same electrolyte using copper foil (0.02 in thickness, in a controlled surface area) as working electrode and platinum wire (0.004 in diameters) as counter electrode. A constant voltage was applied directly between cathode and

anode. A multimeter (Keithley 2000 Multimeter) was used to measure the cathodic and anodic potential respectively. All the electrodes were rinsed with acetone and deionized water and dried before and after all measurements. The temperature was controlled by placing the whole electrowinning cell on a hot plate. A thermometer was inserted into the solution to monitor temperature. Electrowinning duration is fixed at one hour. The electrolyte was keeping for half an hour after reaching the final temperature. The schematic of lab-scale electrowinning cell is shown in Figure 3.10.

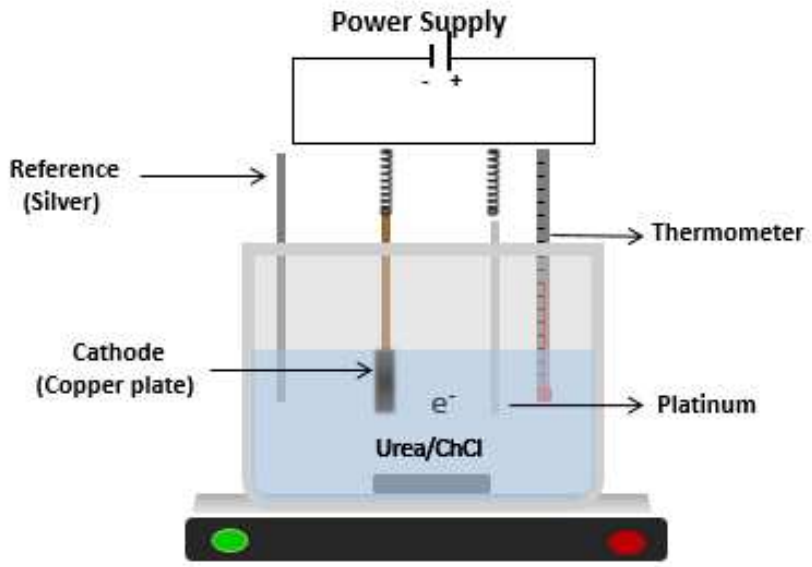

Figure 3.10 Schematic of lab-scale electrowinning cell setup

3.3.3 Large-scale Electrowinning Set-up Design

The batch electrowinning experiments were conducted in ventilated hood using an electrolytic cell as shown in Figure 3.11. The cell system has four parts: electrolyte reservoir, pump, electrowinning cell and electric connectors. The purpose of separating electrolyte mixing

from electrowinning process was to investigate the feasibility of zinc electrowinning in continuous or batch mode for large scale applications. Copper sheet and graphite plate were used as working and counter electrode respectively. The distance between electrodes are fixed at 2 cm, to minimize the effect of diffusion and to avoid contact of electrodes via deposit growth. A thicker graphite electrode was used as consumable anode. Electrowinning was carried out in a deep eutectic solution driven by piston pump with required concentrations of zinc oxide at constant temperatures. A constant voltage was applied to the cell. After the experiment, the pump was stopped and electrodes were removed from the cell, cleaned and weighted. Further analysis was performed to determine current efficiency, energy consumption, deposit microstructure and anodic weight loss. The main variable investigated in the batch process is electrowinning duration. Specific conditions employed in this experiment is concluded in Table 3.2.

Table 3.2 Batch recirculation electrowinning experimental parameters

Applied voltage	3.3V
Working Electrode	Cu (0.02'' in controlled area)
Counter Electrode	Graphite (0.2'' in diameters)
Concentration of ZnO	1.0 mol/L
Time	40-720 minutes
Temperature	90°C
Electrodes distance	2 cm

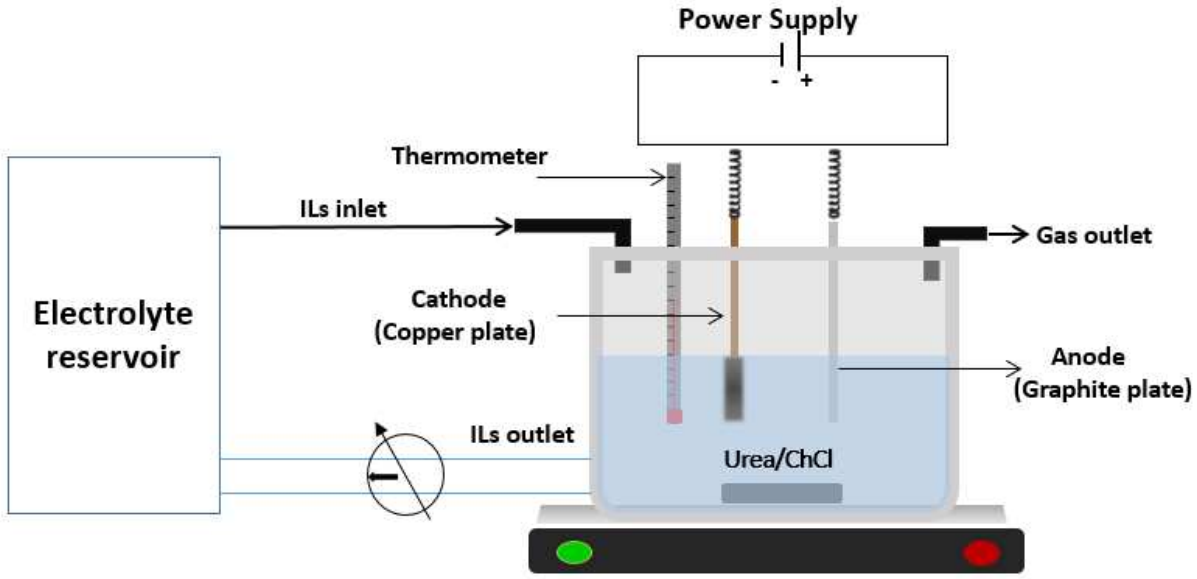

Figure 3.11 Schematic design of large-scale electrowinning system

3.3.4 SEM and EDS Analysis

The morphology and elemental analysis of the deposits were carried out using Scanning Electron Microscope (SEM), model JEOL 7000 equipped with Energy Dispersive Spectrometer (EDS). Samples were directly mounted on SEM sample stub using carbon conducting tape for morphological analysis. Samples are completely rinsed with ethanol and deionized water, then dried in the air prior to use. The SEM images were obtained by setting accelerating voltage at 20kV, and a working distance of 10.0mm.

3.3.5 XRD Analysis

The characterization of zinc deposits on the working electrode were analyzed using X-ray diffraction pattern obtained from a Phillips MPD XRD using a monochromated Cu kα radiation.

Samples are completely rinsed with ethanol and deionized, then dried in the air before use. Deposits along with substrate material were directly mounted on silica glass which was then inserted into diffractometer. The resulting pattern was compared with the standard ICDD card.

CHAPTER 4

FUNDAMENTAL STUDIES OF ELECTROCHEMICAL DEPOSITION OF ZINC

4.1 Dissolution of Zinc Oxide in Choline Chloride and Urea Based Ionic Liquid

4.1.1 Dissolution of ZnO in Urea/ChCl electrolyte

The dissolution of ZnO in 2:1 Urea/ChCl electrolyte was studied using Fourier Transform Infrared Spectroscopy (FTIR). Figure 4.1(b) shows the FTIR spectrum of neat 2:1 Urea/ChCl electrolyte and the spectral analysis of bond-stretching frequencies for different functional groups of Urea/ChCl indicate a close agreement with the corresponding reported peaks from literature (in Table 4.1) [**64, 65**]. Figure 4.1(a) shows the FTIR spectrum of 2:1 Urea/ChCl electrolyte containing dissolved ZnO. Noticeably, on comparison with the blank spectrum of Figure 4.1(b), an additional absorption peak was observed at 2150 cm^{-1} because of dissolution of ZnO in the electrolyte. Cl^- ions of the electrolyte weakens the chemical bond of dissolved ZnO molecule and then Zn (II) ion of ZnO interacts with urea molecule and forms complex anion, $[ZnClO\cdot\ urea]^-$. The additional absorption peak, of Figure 4.1(a), is associated with the stretching vibration of Zn (II) - urea bond of $[ZnClO\cdot\ urea]^-$ ion [**64**] and therefore, acts as a diagnostic tool to identify the dissolution of ZnO in 2:1 Urea/ChCl electrolyte.

Table 4.1 Standard infrared absorption of stretching and bond variations for different functional groups

Functional Group	Characteristic Absorptions (cm^{-1})	Intensity
$-NH_2$	3202-3444	Strong
-RNHC=ONHR	1620-1668	Strong
$-CH_3$	1360-1474	Strong
$-R_4N^+$	970-1360	Medium
-CCO	955	Strong

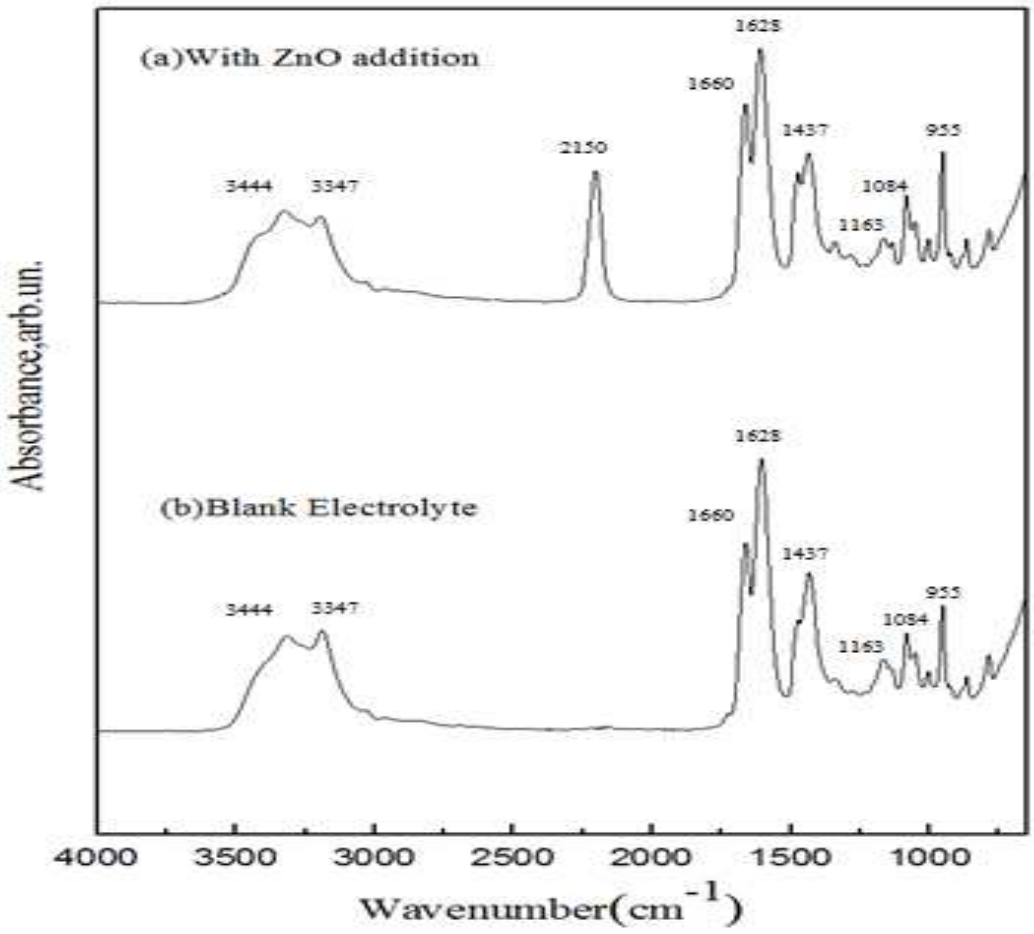

Figure 4.1 FTIR spectrum of (a) with zinc oxide addition in 2:1 Urea/ChCl; (b) 2:1 Urea/ChCl mixture

Dissolution of ZnO in 2:1 Urea/ChCl electrolyte is affected by (a) the temperature of mixing, and (b) the concentration of ZnO additions. Figure 4.2 shows the effect of temperature on dissolution of 0.82mol/L ZnO in 2:1 Urea/ChCl using FTIR spectra. The area of the characteristic absorption peak, from 2100 cm^{-1} to 2300 cm^{-1}, increases with the rise in temperature from 70 to 100°C, thus, implying a greater solubility of ZnO in Urea/ChCl at higher temperatures. This is because of the additional heat obtained at higher temperatures, which facilitates the dissolving reaction by providing sufficient energy to break bonds in the solid, and therefore, stronger FTIR absorption peak were observed from 2100 cm^{-1} to 2300 cm^{-1} at higher temperatures. Figure 4.3 shows the effect of ZnO concentration on dissolution process in the Urea/ChCl electrolyte at fixed temperature of 100°C. Solutions contained ZnO in different concentration (from 0.41 to 1.23 mol/L) are measured with respect to FTIR absorption intensities of the peak, from 2100 cm^{-1} to 2300 cm^{-1}, showing an increase in peak intensity in higher ZnO concentration. However, no change in the peak intensity is observed for solution with 2.05mol/L ZnO. For further scrutiny, Figure 4.4 is plotted peak intensity as a function of concentration. It is clearly seen that FTIR absorption intensities (2100 to 2300 cm^{-1}) increases linearly with ZnO concentration from 0.41 to 1.23 mol/L, which is according to Beer-Lambert law; while no change in peak intensity was observed beyond 1.23 mol/L. Therefore, dissolution limit of ZnO in Urea/ChCl (2:1 molar ratio) electrolyte is 1.23 M at 100°C based on FTIR absorbance peak analysis.

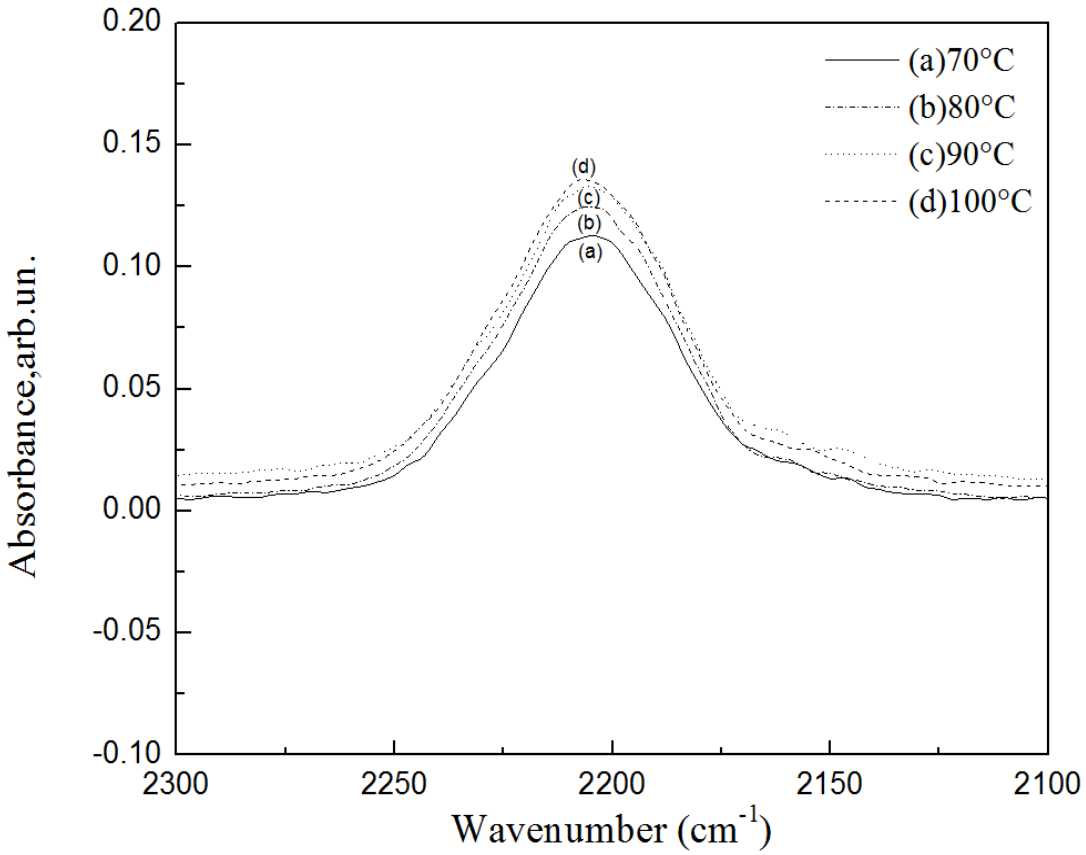

Figure 4.2 FTIR absorbing peaks (from 2100 to 2300 cm^{-1}) of 0.82mol/L ZnO in 2:1 Urea/ChCl at different temperatures

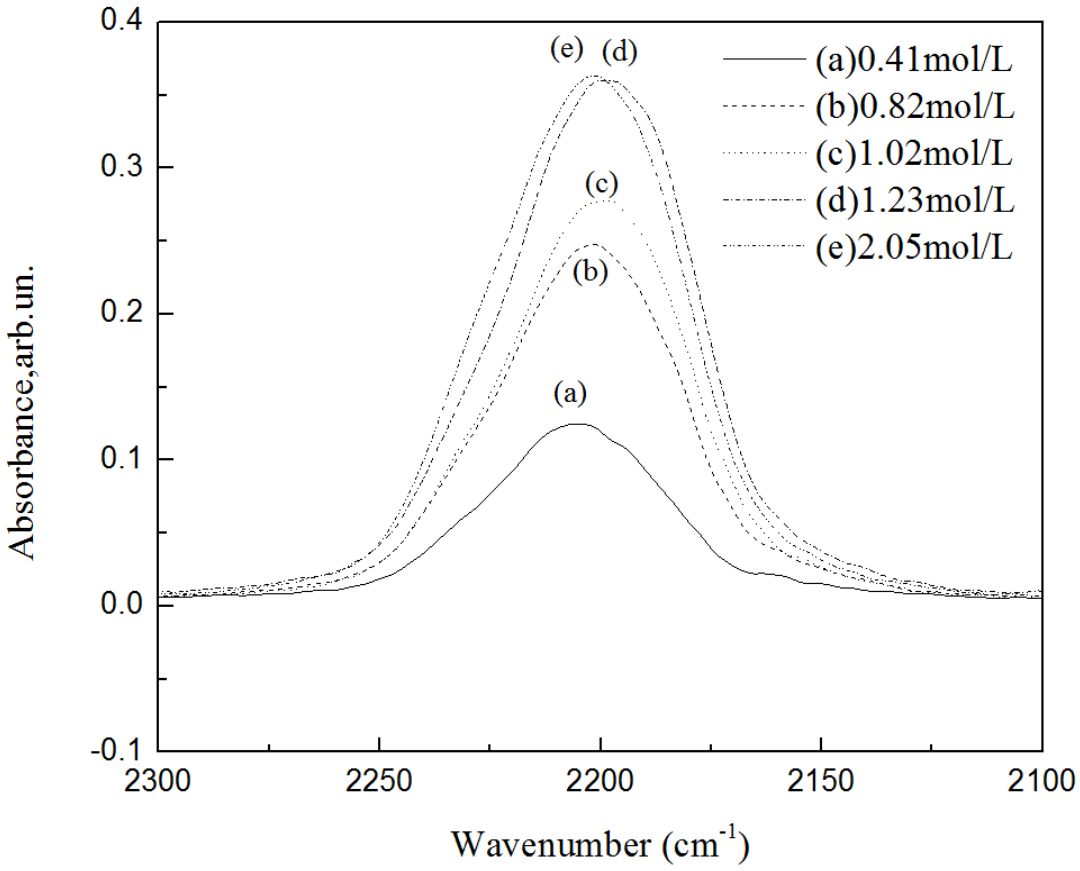

Figure 4.3 FTIR absorbing peaks (from 2100 to 2300 cm^{-1}) of ZnO in 2:1 Urea/ChCl in different concentrations at 100°C

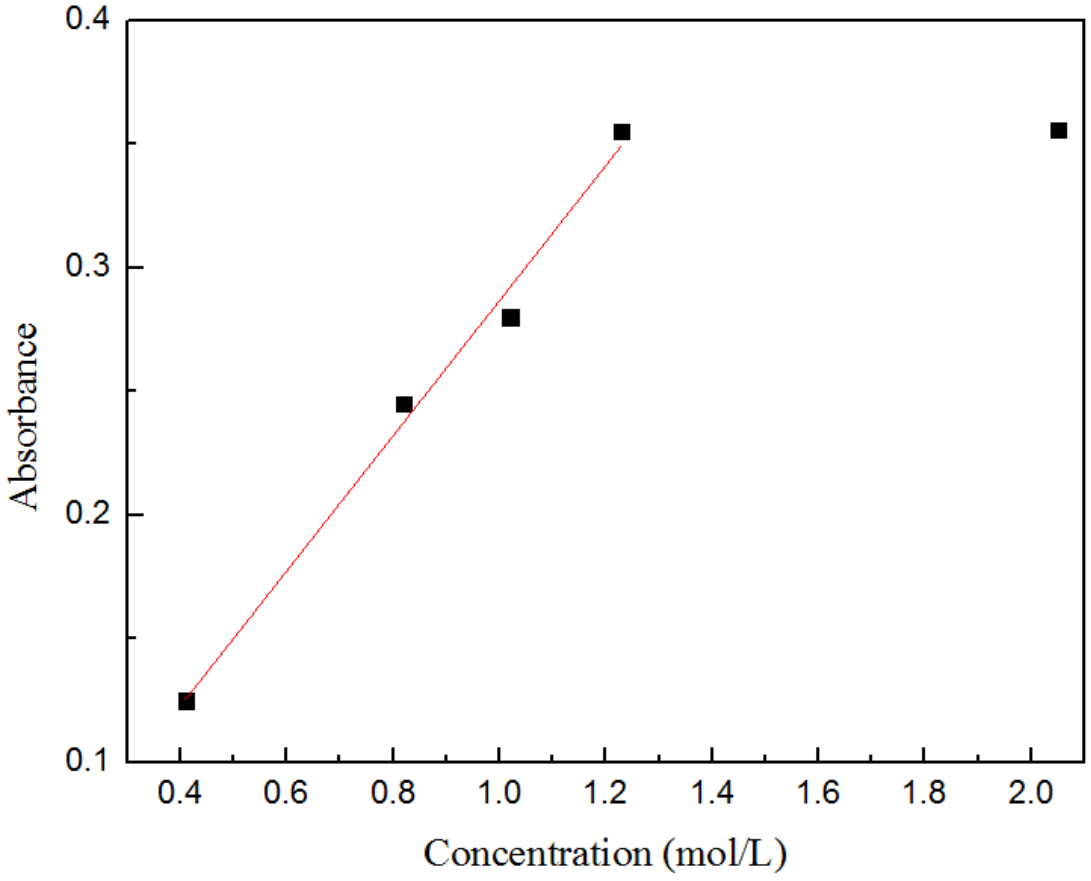

Figure 4.4 FTIR peak absorbance plot against concentration of ZnO at 100°C

4.1.2 Solubility of ZnO in Urea/ChCl electrolyte

While the FTIR provides a direct view of comparative dissolution at each condition, more quantitative analysis of zinc oxide solubility was studied using ICP-AES. The solution was prepared at room temperature, diluted with 0.2 N HNO_3. Solubility measurement was carried out by placing excess amount of ZnO in electrolyte, kept for 24 hours at different temperature with stirring rate of 60 rpm. Results are shown in Figure 4.5 comparing experimental data (in Black Square) with literature data (in red circle) [**66]**. It can be seen that zinc oxide solubility exhibits strong temperature dependence as a significant increase is observed when increases temperature

from 60 to 70°C. The solubility measured at 100°C is equal to 90584 in ppm, further confirmed with the dissolution limit obtained in FTIR.

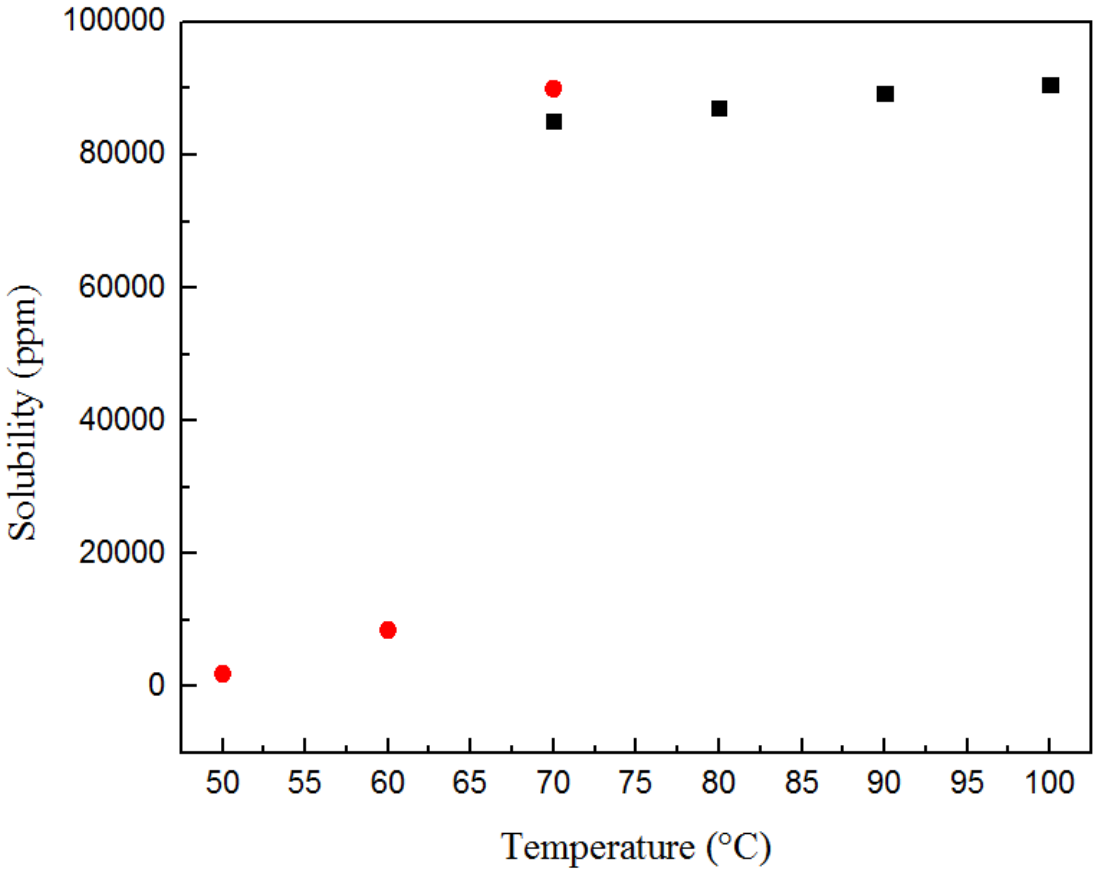

Figure 4.5 Solubility of zinc oxide in eutectic mixture of ChCl with Urea (in molar ratio 1:2) at different temperatures; (●) literature value (■) experiment value **[66]**

4.2 Electrochemical Measurement of ZnO-Urea/ChCl Solution

The solubility measurement of ZnO in Urea/ChCl eutectic mixture lays a good foundation for the electrodeposition of Zn from ZnO-Urea/ChCl solution. Cyclic Voltammetry (CV) is used to study the electron-transfer process and electrode reaction mechanism for ZnO-Urea/ChCl system. Three-electrode system was composed of tungsten as working electrode, platinum as counter electrode and silver as reference electrode. The solid curve of Figure 4.6 shows the CV of

Urea/ChCl (2:1 molar ratio) electrolyte. Formation of hydrogen gas takes place at the cathodic limit (-1.2 V) **[65]**. The dotted curve in Figure 4.6 shows the CV of ZnO-Urea/ChCl electrolyte. The red-ox reactions of Zn occurs within the electrochemical window of the blank electrolyte. Only one set of red-ox reaction peaks was observed in CV for ZnO-Urea/ChCl electrolyte, thus indicating the electrodeposition of Zn takes place via one step two-electron transfer process. The onset reduction potential at -1.05 V is due to the reduction of Zn^{2+} to Zn and similarly, the oxidation peak at -0.8 V is mainly because of stripping of deposited Zn. The electrodeposits were confirmed as pure Zn metal from XRD and EDS.

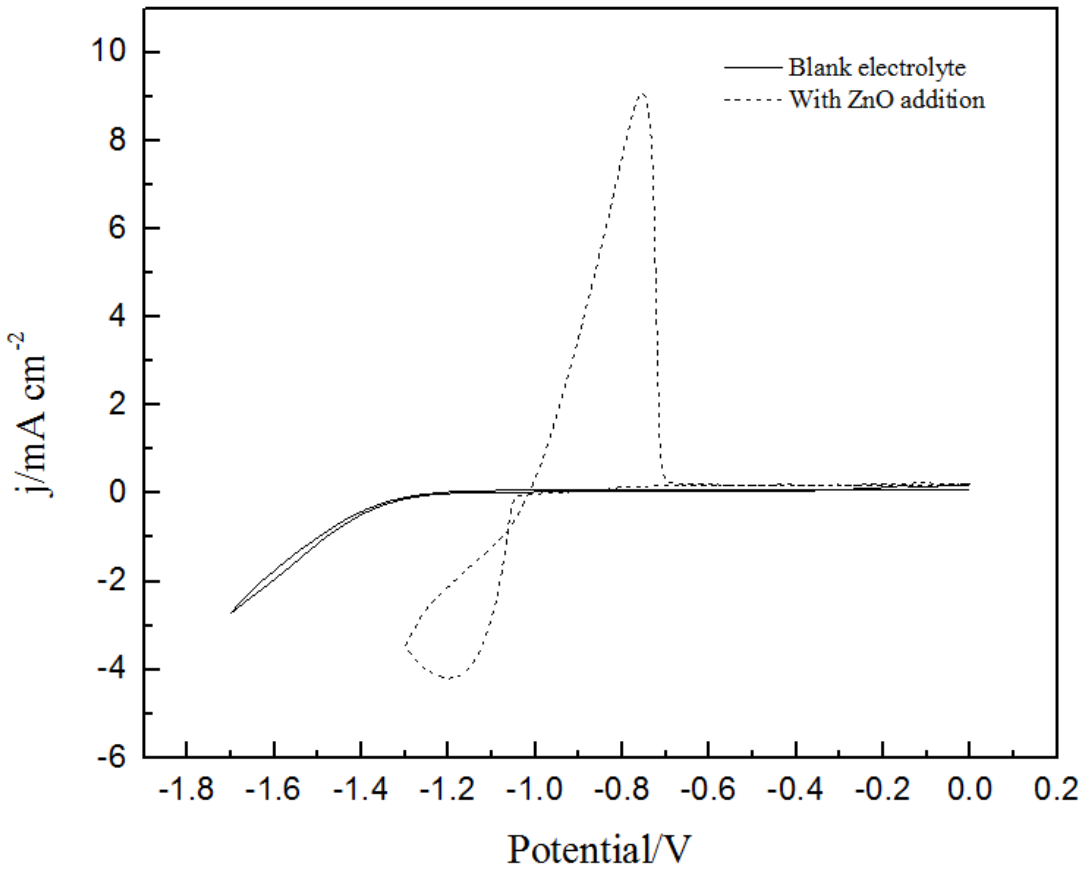

Figure 4.6 Cyclic Voltammetry of (—) blank electrolyte (Urea/ChCl) and (---) 0.41 M ZnO addition to Urea/ChCl (2:1 molar ratio), at 373 K and a scan rate of 50 mVs^{-1}

Figure 4.7 shows the CV plot of ZnO-Urea/ChCl electrolyte at different scan rates of (a) 20, (b) 35, (c) 50, (d) 65 and (e) 80 mV/s. Asymmetric reduction/oxidation peaks are observed, however, it is hard to judge reversibility of a metal ion/metal redox couple because a solid electrode is used as the working electrode. Nevertheless, it is observed that the maximum reduction potential (E_{pc}) undergoes a negative shift as the scan rate is increased from 20 to 80 mV/s which is a sign of an irreversible process. Meanwhile, the separation of reduction/oxidation peaks is much larger than the theoretical value 2.3RT/nF (37 mV when n=2), which is expected for a reversible exchange process. These features suggest that the charge-transfer process is very likely to have occurred in an irreversible manner [**67-69**] and similar observations are made in other literatures [**70,71]**.

It is also noticed that there is a clear interception between cathodic and anodic peak observed when scan direction was reversed (pointed out in Figure 4.7). This phenomenon indicates that there is nucleation and growth mechanism involved when Zn deposited on the cathode. Moreover, the cathodic peak current density (j_{pc}) against square root of scan rate ($v^{1/2}$) is found to be linear, as showed in the inset of Figure 4.7, which suggests that the reduction process is most likely to be controlled by diffusion of electroactive species from the electrolyte to the electrode surface. However, the plot of j_{pc} vs. $v^{1/2}$ does not pass through the origin as expected for simple linear diffusion process. This additional kinetic current may be due to the nucleation and growth involved in the process of diffusion or could be because of the influence of electrolyte resistance [**72-74]**. Diffusion process shows the temperature dependence, as the slope of each line increases as temperatures increase from 70 to 100°C, which can be seen in Figure 4.8.

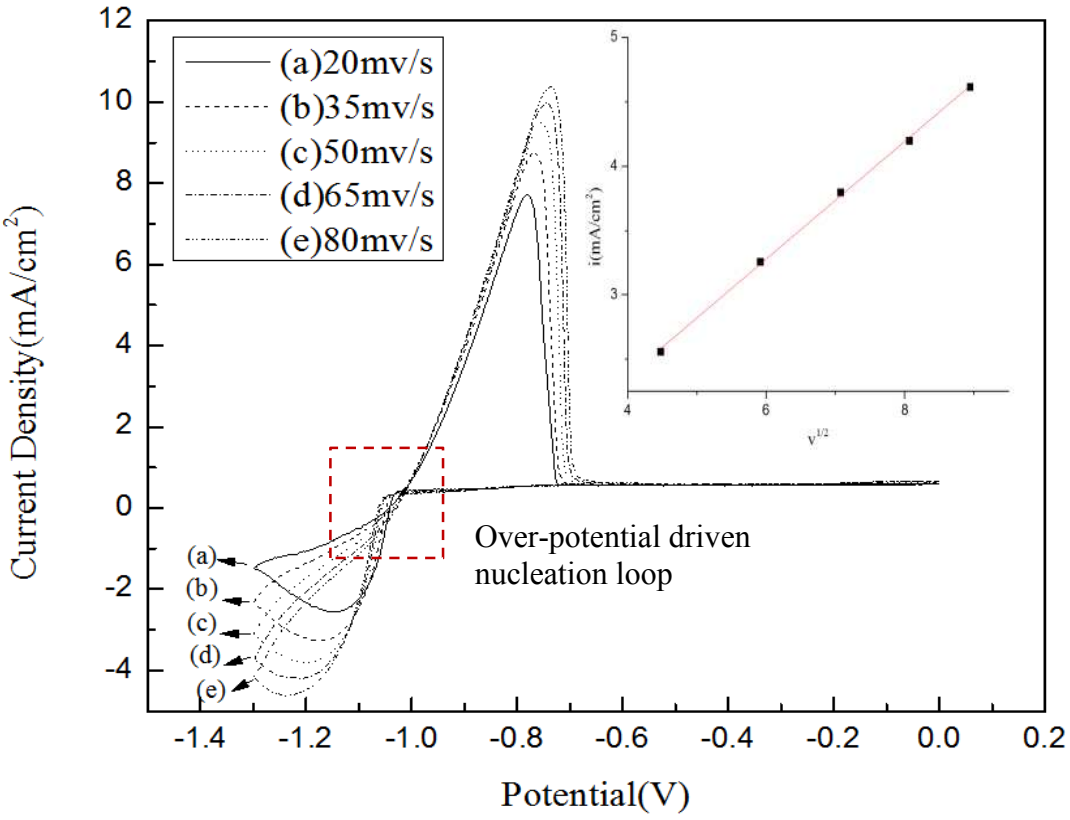

Figure 4.7 Cyclic voltammograms of ZnO addition (0.41mol/L) to 2:1 Urea/ChCl eutectic mixture at a temperature of 100°C scan rate (mV/s): (a) 20; (b) 35; (c) 50; (d) 65; (e) 80 respectively; the inset graph exhibits the relationship between i_{pc} and $v^{1/2}$

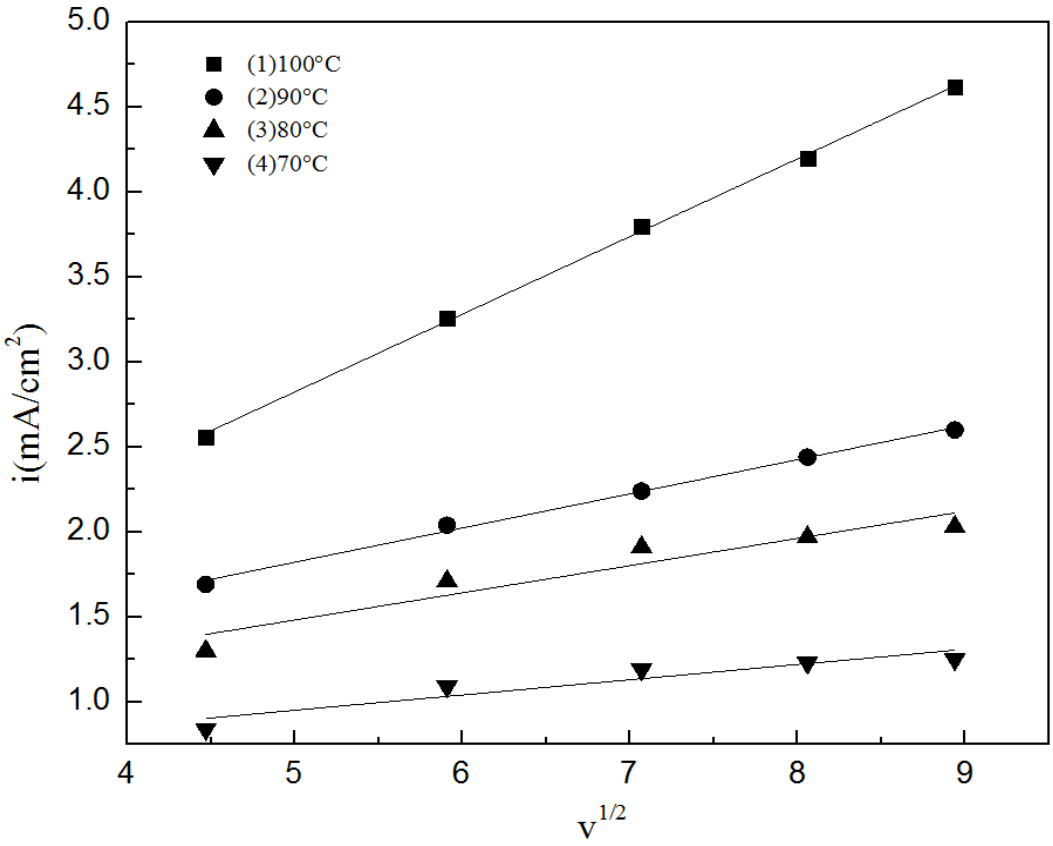

Figure 4.8 Cathodic peak current density as a function of square root of scan rate in 2:1 urea and choline chloride ionic liquid in various temperatures: (1) 100°C; (2) 90°C; (3) 80°C; (4) 70°C

4.3 Zn nucleation and growth mechanism

Chronoamperometry (CA) experiments were performed in Urea/ChCl electrolyte to study the nucleation and growth mechanism of Zn electrodeposition on Cu substrate. A collection of current-time transients were obtained by stepping the potential from the initial value of -1.0V where the substrate layer is stable, to the value that is negatively sufficient to initiate the nucleation and growth of zinc, as illustrated in Figure 4.9.

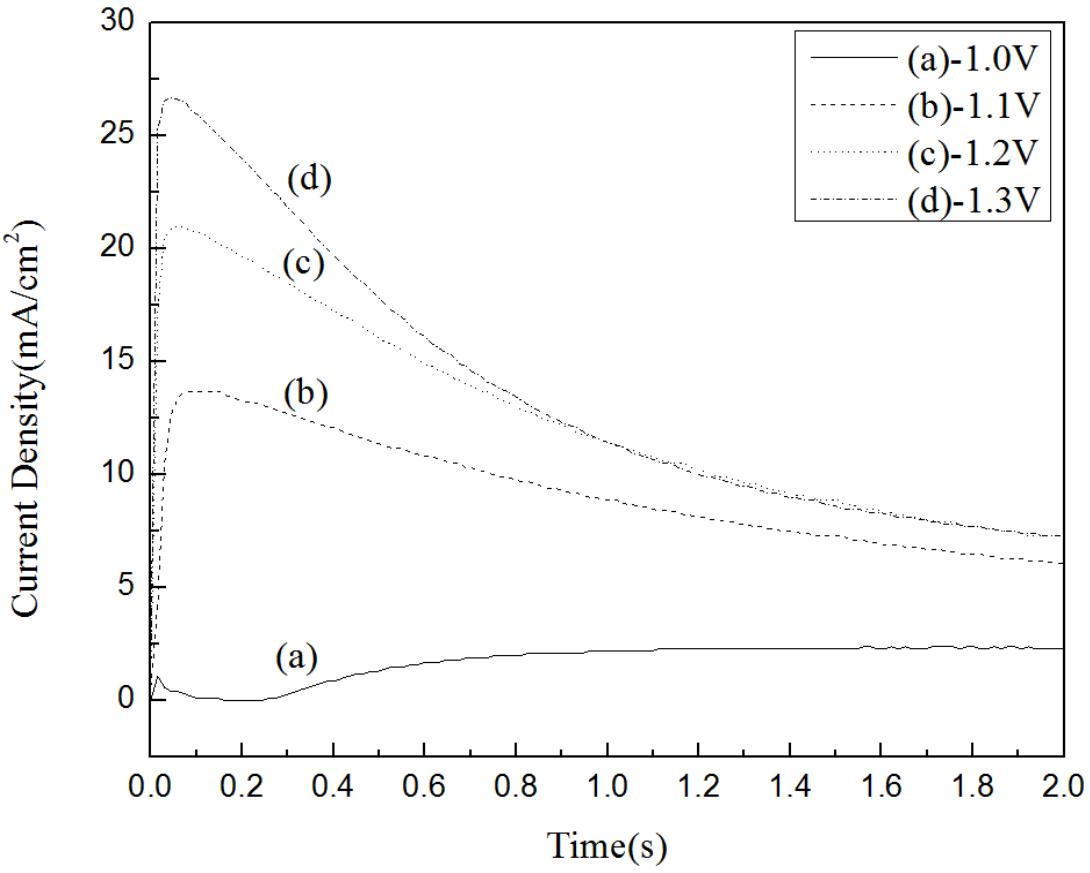

Figure 4.9 Current-time transients resulting from chronoamperometry of ZnO addition (0.41 mol/L) to 2:1 Urea/ChCl mixture at 100°C in different overpotentials: (a) -1.0V; (b) -1.1V; (c) -1.2V; (d) -1.3V

All current-time transients follow the typical trend of diffusion- controlled nucleation and growth which is characterized by a sudden change in current appeared at the first 0.02 s which is due to the electrochemical double layer charge; a subsequent rising portion is attributed to an increase in electro-active area in which nucleation occurs. A hemispherical diffusion zone around the nuclei was generated during the process of nuclei growth. Since the overlapping of these zones, hemispherical mass transfer changes its way to planar mass transfer. Thus, a maximum current density i_m obtained in t_m and started to decay after reaching its peak. The decaying portion of the transient is described in Cottrell equation i.e., inverse-relationship between current and time for a

diffusion-controlled process **[75]**. In addition, the time (t_m) needed to reach maximum current density (j_m) shifts to lower value at higher negative applied potential.

The most widely used model to describe nucleation and growth mechanism was first introduced and developed by Scharifker and Hills [**76**]. According to their theory, the three-dimensional nucleation and growth processes occurred during the electro-deposition process of metal on foreign substrates can be described as either instantaneous nucleation (fast nucleation on small number of active sites) or progressive nucleation (slow nucleation on large number of active sites) process. The resulting expression to distinguish instantaneous and progressive nucleation is as followed Eq. 4.1 and 4.2 [**77**]:

$$(i/i_m)^2 = 1.9542\left(\frac{t}{t_m}\right)^{-1}\{1-\exp[-1.2564(t/t_m)]\}^2 \quad (4.1)$$

$$(i/i_m)^2 = 1.2254\left(\frac{t}{t_m}\right)^{-1}\{1-\exp[-2.3367(t/t_m)^2]\}^2 \quad (4.2)$$

To understand whether the process is instantaneous or progressive nucleation, a common method is to compare the experimental current-time transients with theoretical transients of each mechanism, as presented in Figure 4.10. It exhibits the comparison of dimensionless current density-time transients with theoretical model which is obtained from Eq. 4.1, and 4.2. Instantaneous nucleation process takes place at each potential. The current density trend at longer time period is larger than predicted instantaneous model which is due to the hydrogen reduction on the electrode. All nucleation processes come with diffusion-controlled growth.

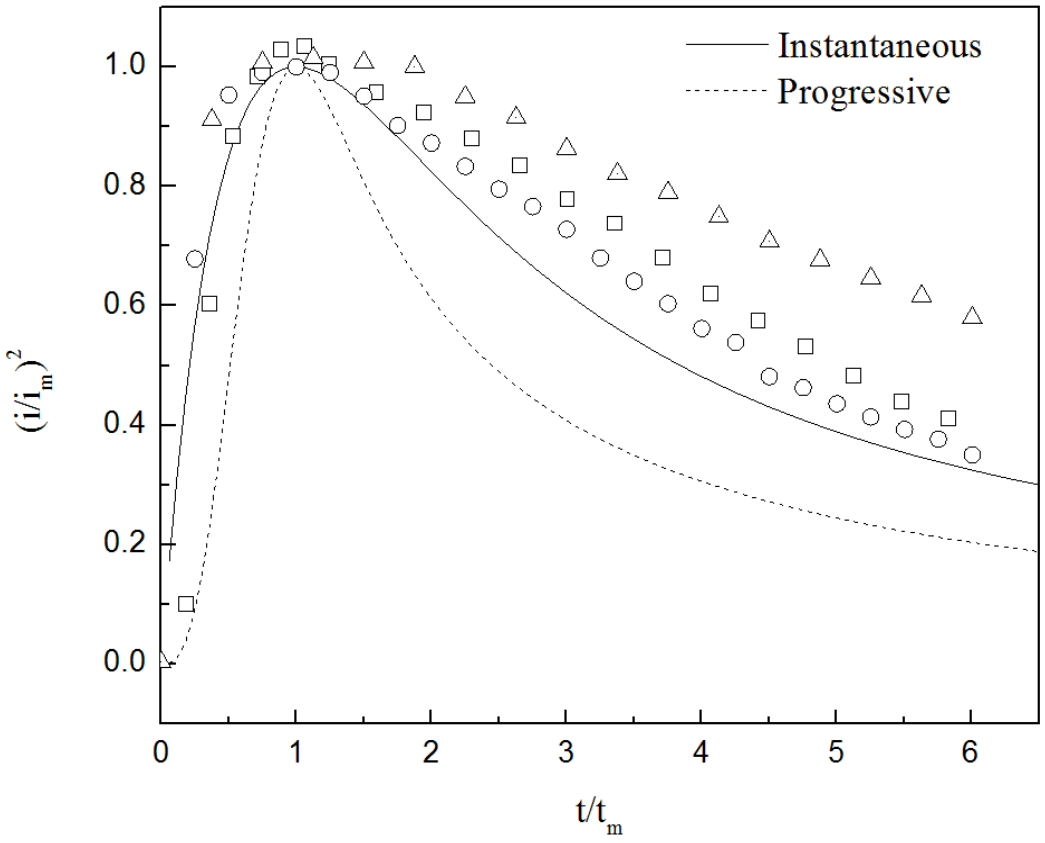

Figure 4.10 Comparison of the dimensionless experimental current-time transients over a potential range: (□) -1.1V; (○) -1.2V; (Δ) -1.3V, to the theoretical models for instantaneous and progressive nucleation with a diffusion controlled growth of zinc nuclei

The diffusion coefficient (D in cm^2/s) is calculated by measuring i_m and t_m from Figure 4.9, as shown in Eq. 4.3 [**78, 79**]:

$$i_m^2 t_m = 0.1629(nFC)^2 D \qquad (4.3)$$

The average value of the diffusion coefficient is 1.89×10^{-8} cm^2/s which is compared with the various systems investigated by Reddy's research group [**80-82**] and other groups [**83-84]** and are listed in Table 4.2. All values of diffusion coefficients fall within reasonable range. The different values of diffusion coefficient for Zn contained species could be due to different temperatures, and the ionic liquid systems considered for the electrodeposition. In addition, zinc

contained complexing agent is shown a smaller diffusion coefficient compared to Zn^{2+} mostly because of the highly viscous electrolyte as well as the heavier ion.

Table 4.2 Diffusion coefficient of different species in various ionic liquid systems

Ionic liquid	Predominant Species	T(K)	D ($cm^2\ s^{-1}$)	Reference
Urea/ChCl	$[ZnO{\cdot}Cl{\cdot}urea]^-$	373	1.89×10^{-8}	This work
Urea/ChCl	$[PbO{\cdot}Cl{\cdot}urea]^-$	363	2.42×10^{-7}	[56]
Urea/ChCl	$[CoCl_3]^-$	373	1.7×10^{-6}	[80]
$AlCl_3$-BMIC	$[Al_2Cl_7]^-$	363	2.2×10^{-7}	[81]
$AlCl_3$-EMIC	$[Al_2Cl_7]^-$	363	9.1×10^{-7}	[82]
$[Bu_3MeN]Tf_2N$	Zn^{2+}	373	4.12×10^{-8}	[83]
$AlCl_3$- MeEtimCl	Zn^{2+}	313	6.7×10^{-7}	[84]

4.4 Mechanism of Electrode Reaction

Electrodeposition of zinc were conducted at 90°C on Cu substrate for 1 h based on the reduction potential of Zn^{2+} ions from the CV experiments. Given that predominant $[ZnO{\cdot}nCl{\cdot}urea]^{n-}$ has been confirmed by other authors [**64, 85**] and the fact that stretching C-C=O bond found in FTIR at $955cm^{-1}$, the structure of Ch^+ is not destroyed in Urea-ChCl system. As a result, the remaining Ch^+ may react with $[ZnO{\cdot}nCl{\cdot}urea]^{n-}$ obtained two electrons forming Zn deposits on the cathode and left $[HOC_2H_4N(CH_3)_3\ OCl{\cdot}urea]^{2-}$ as possible anion which may remain in the solution. The possible electrode reactions have shown below:

Dissolution reaction:

$$ZnO + Cl^- + urea \rightarrow [ZnO{\cdot}Cl{\cdot}urea]^- \quad (4.4)$$

Cathodic reaction:

$$Ch^+ + [ZnO{\cdot}Cl{\cdot}urea]^- + 2e^- \rightarrow Zn(s) + [ChCl{\cdot}O{\cdot}urea]^{2-} \quad (4.5)$$

Anodic reaction:

$$[ChCl{\cdot}O{\cdot}urea]^{2-} \rightarrow Ch^+ + Cl^- + 2e^- + 0.5O_2 \quad (4.6)$$

Overall reaction:

$$ZnO \rightarrow Zn\ (s) + 0.5O_2 \quad (4.7)$$

4.5 Characterization of Zn electrodeposits

The XRD pattern in Figure 4.11 shows in common with the characteristic diffraction peaks of Zn (ICDD File No.00-004-0831) at 2θ=36.3°;38.9°;43.2°;54.3°;70.0°;82.1°;86.6°;89.9° which is corresponded to (002), (100), (101), (102), (103), (112), (201), and (104) diffraction peaks of hexagonal zinc particle. The distinct peak observed at 50.4° is coming from Cu substrate according to ICDD File No. 00-004-0836.

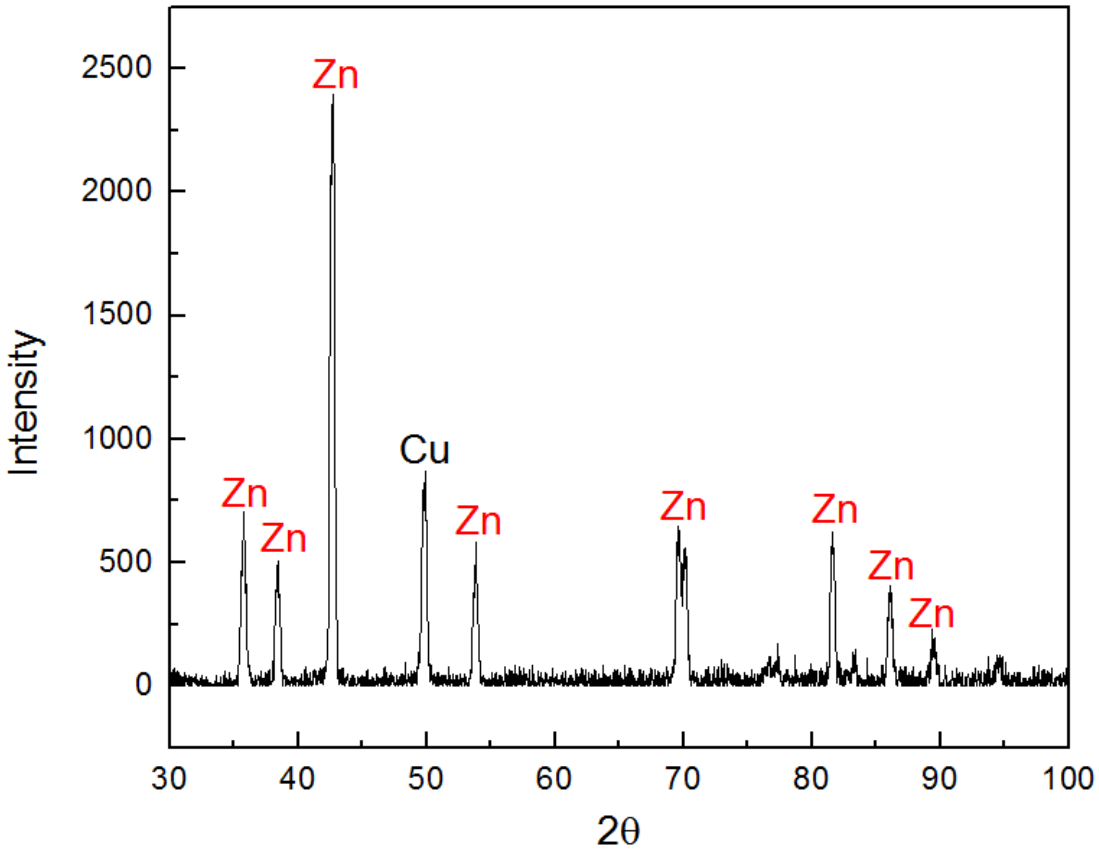

Figure 4.11X-ray diffraction (XRD) pattern for Zinc deposits on cathode

The composition analysis was conducted using EDS, as shown in Figure 4.12. As expected, all strong peaks account for zinc and weak Cu peaks are from substrate.

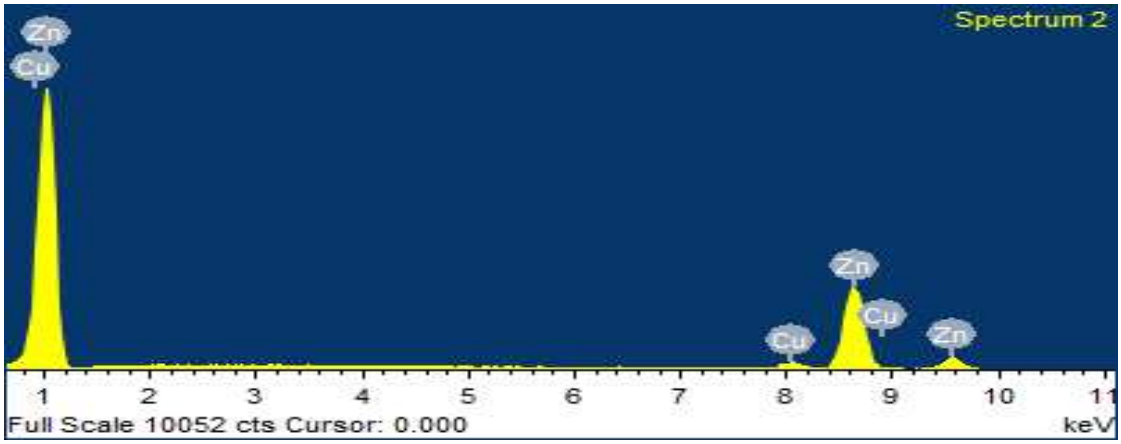

Figure 4.12 EDS spectrum analysis for zinc coating on the cathode

4.5.1 Effect of Reduction Potential

The morphology of zinc deposits on the cathode which obtained in different reduction potentials are shown in Figure 4.13. As seen in Figure 4.13(a), at -1.1V, nodular zinc particle was found while the film is not compact or uniform. However in Figure 4.13(b), the zinc deposits which obtained in a fixed potential of -1.2V exhibit coarse, typical hexagonal zinc crystals. At this stage, the film is dense and the growth of grain is significant which can reach an average size of 5μm. As potential goes more negative to -1.25V in Figure 4.13(c), agglomeration of particles observed while zinc particle is no longer grown in size. However, individual particle starts to split into small plate-like structure. In Figure 13(d), zinc deposits obtained from -1.3V appear to show morphology consisted of only platelets that perpendicular to the substrate surface. As seen from micrograph in higher magnification, the stacked-up platelets agglomerate inside each grain where further nucleation seems to occur along with the formation of plate-like crystal. Liu et al also observed similar changing morphology of the deposits that occur due to solvation layers absorbed at the growing Zn surface [**86].**

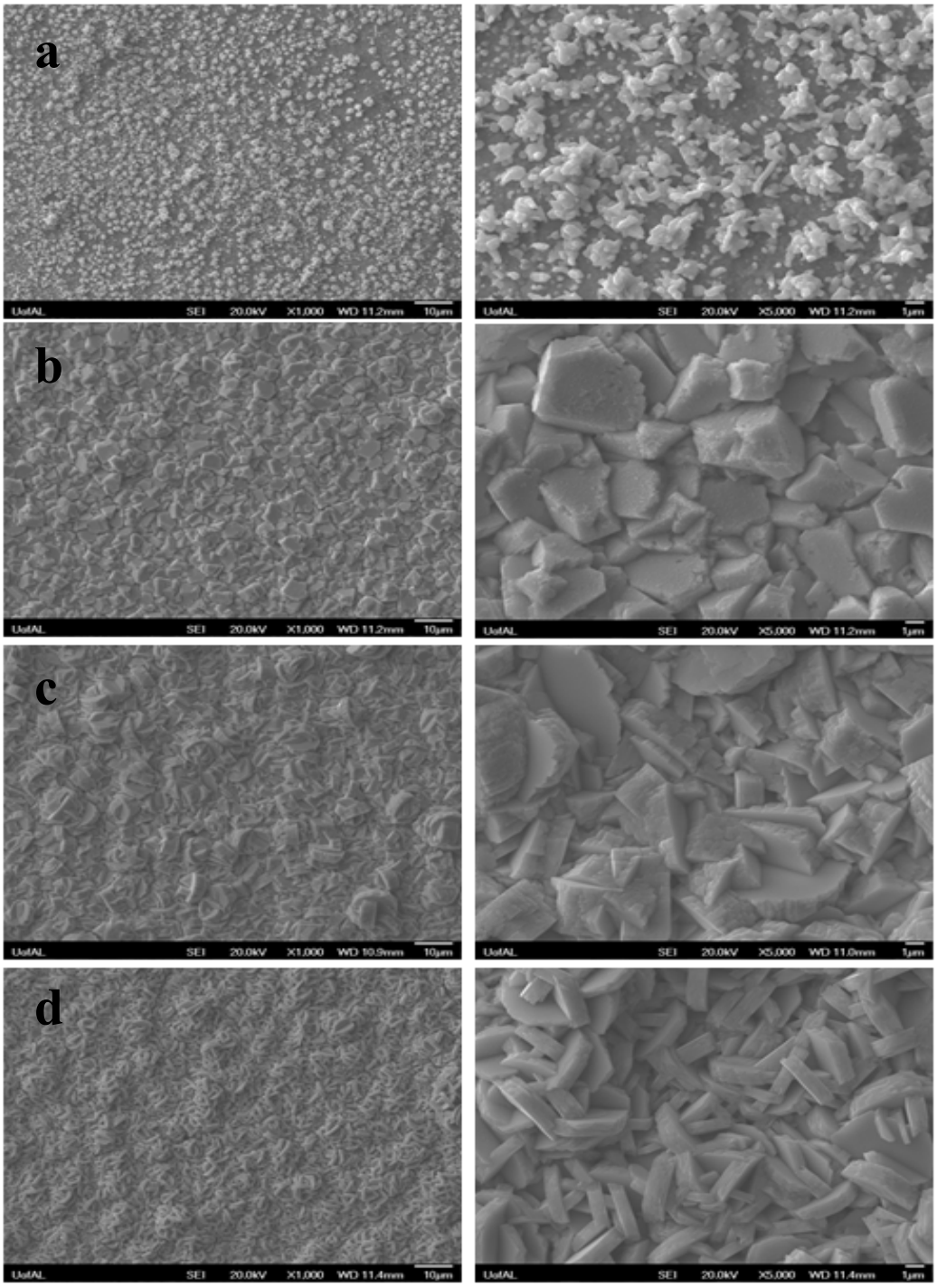

Figure 4.13 SEM micrographs of zinc deposits on Cu substrate in different potential: (a) -1.1V; (b) -1.2V; (c) -1.25V; (d) -1.3V at temperature of 100°C. On the right are pictures in higher magnification

4.5.2 Effect of Temperature

The effect of temperature on the morphology of zinc deposited film on the cathode is studied as well. As seen in 4.14a, zinc deposits seem to have a non-uniformity but compact film with smaller particle size about 0.5 μm at 70°C. With increasing temperature to 80°C which is shown in 4.14b, the zinc deposits show a typical hexagonal crystalline structure with a larger average particle size compared to the one obtained from lower temperatures. The overall morphology appears the same in even higher temperature such as 90°C, but with a thicker and larger particle with an approximate grain size of 2 μm. Further increase temperature to 100°C, it is showed a brighter grain with an average particle size about 3 μm. At this point, we notice that temperature has largely influenced surface morphology by generating nodular cauliflower like structure which formed at the top of each particle [**87**].

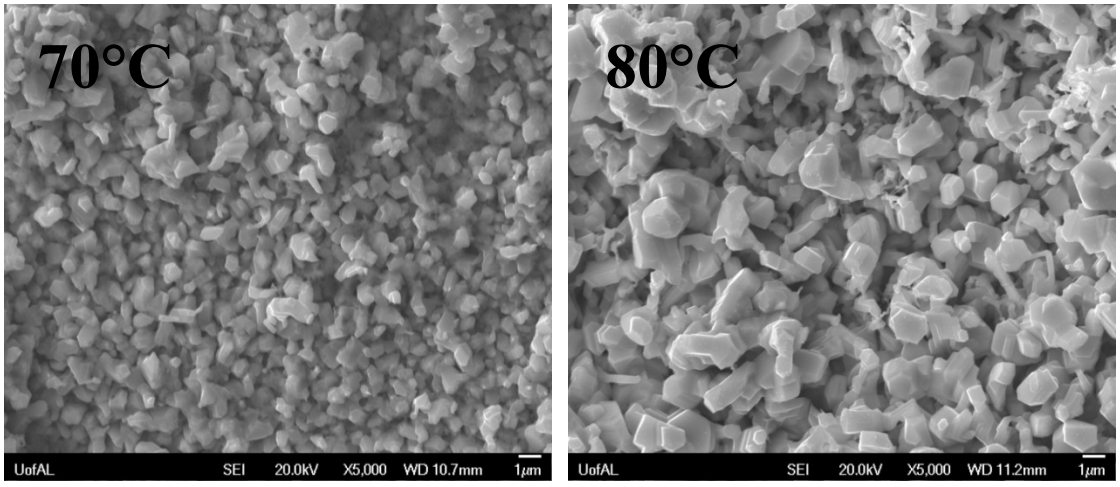

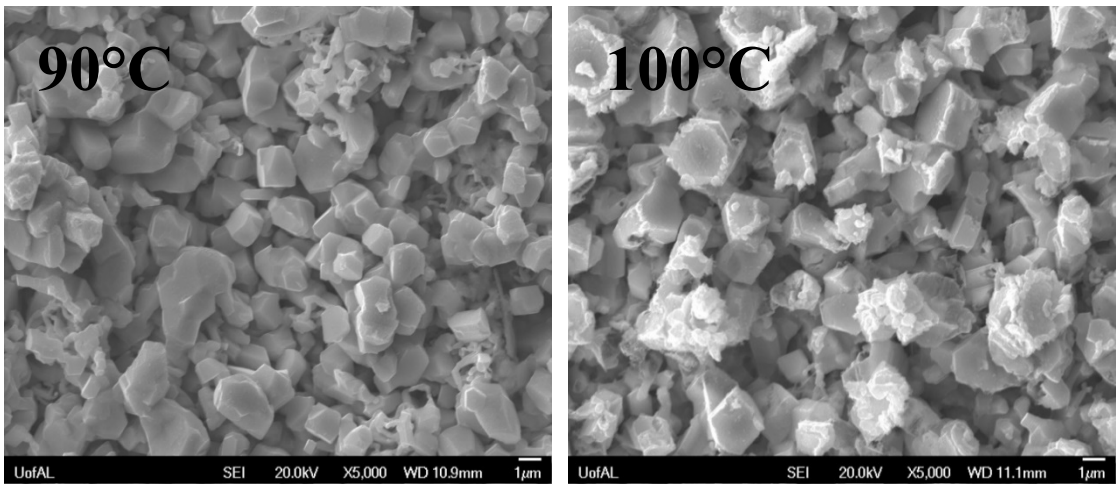

Figure 4.14 SEM images of deposited zinc on Cu substrate at different temperature: (a) 70°C; (b) 80°C; (c) 90°C; (d) 100°C, at 3.0V

4.5.3 Effect of $[Bmim]HSO_4$ as additive

In the present study, since $[Bmim]HSO_4$ has been used widely as lubricant, we propose that it can act as leveling agent to improve the quality of deposits in respect of surface morphology. The effect of $[Bmim]HSO_4$ on Zn morphology was studied using scanning electron microscopy (SEM). Typical SEM micrographs are shown in Figure 4.15a-c. In the presence of $[Bmim]HSO_4$, the deposited layer align smoothly and finer grain in found in the solution with higher additive concentration. With introducing $[Bmim]HSO_4$ to the solution, the formation of absorbed layer at the surface of electrode can effectively increase interfacial viscosity, thus the mass transfer process slow down which leading to a decrease in deposition rate. As a result, finer grains are observed.

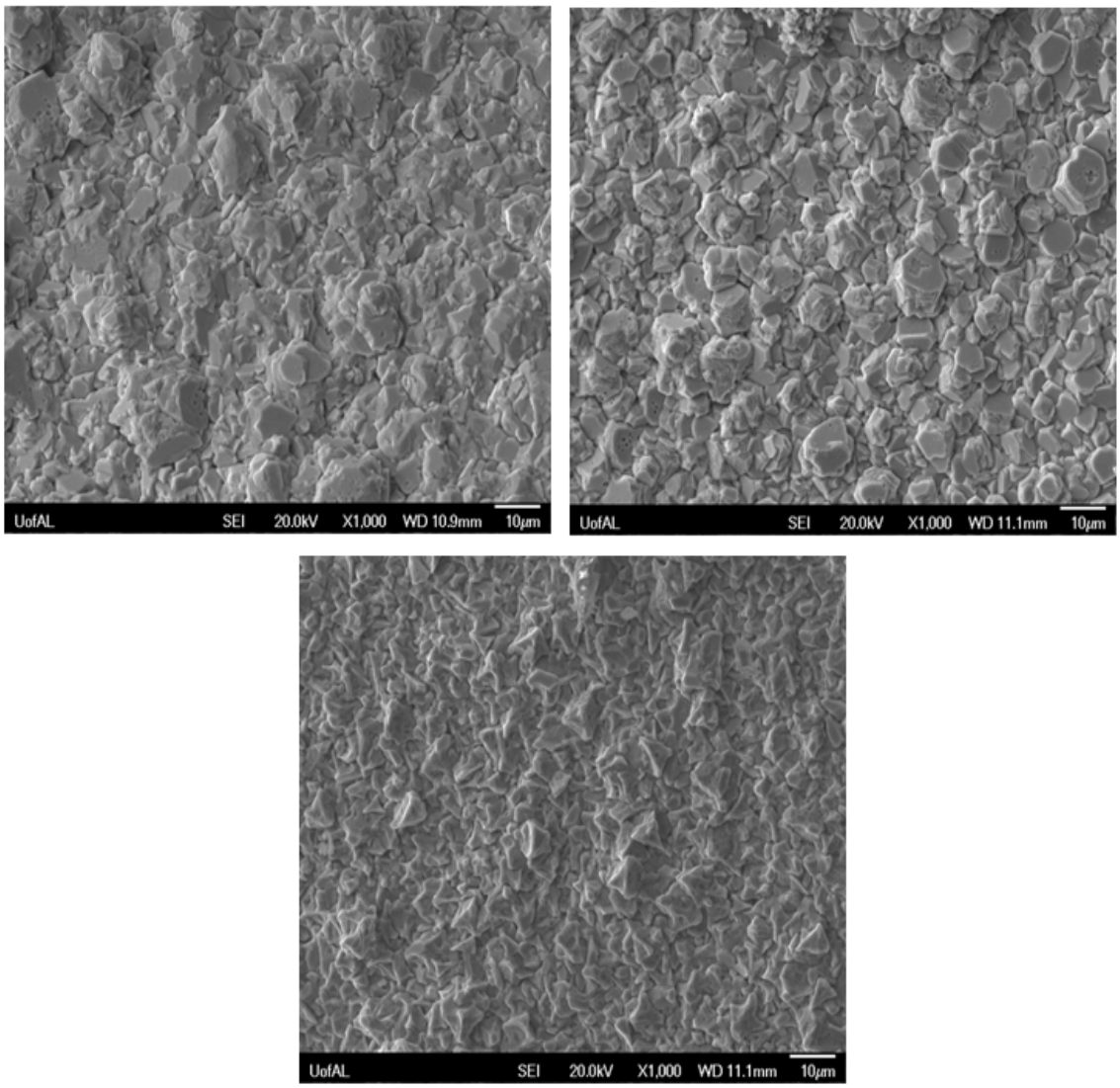

Figure 4.15 SEM images of deposited zinc on Cu substrate at different concentration of additives: (a) 1mg/mL; (b) 1.5mg/mL; (c) 2mg/mL, at 100°C

CHAPTER 5

LAB-SCALE ELECTROWINNING OF ZINC

5.1 Electrowinning of Zn in Urea/ChCl eutectic mixture

The applied cell voltage is measured directly through cathode to anode. Basically, it is consisted of four parts, namely, decomposition potential, anodic over-potential, cathodic over-potential, and electrolyte iR drop. The decomposition potential can be approximated through Gibbs free energy of the reaction. For example, for ZnO, the decomposition potential is shown below:

$$ZnO = Zn + 0.5O_2 \qquad \Delta G=311.590 \text{ kJ/mol}$$

$$E^0 = -1.615V$$

Both cathodic and anodic over-potential can be measured using a multimeter. The electrolyte iR drop is given by:

$$V_{iR} = iL/\sigma$$

Where I is current density, L is electrode separation, σ is electrolyte conductivity. After that, the cell voltage can be calculated by:

$$V_{cell} = V_0 + V_{iR} + \eta_a + \eta_c$$

In order to compare with the industrial used cell voltage which is 3.5V, the potentiostatic electrowinning of Zn was conducted at 90°C for one hour from 3.2 to 3.5V. ZnO was dissolved in the electrolyte in a form of $[ZnO{\cdot}Cl{\cdot}urea]^-$ as the predominant species, which was confirmed in a

previous study as well as in literatures [**88-89**] and the reaction mechanism has been discussed in the previous chapters.

5.2 Potentiostatic Electrowinning of Zn

Current output was recorded at regular intervals and converted into current density by dividing with the zinc deposited area of cathode. Figure 5.1 shows the current density (A/m^2) as a function of time (s) at applied voltages from 3.2 to 3.5V and at a temperature of 90°C.

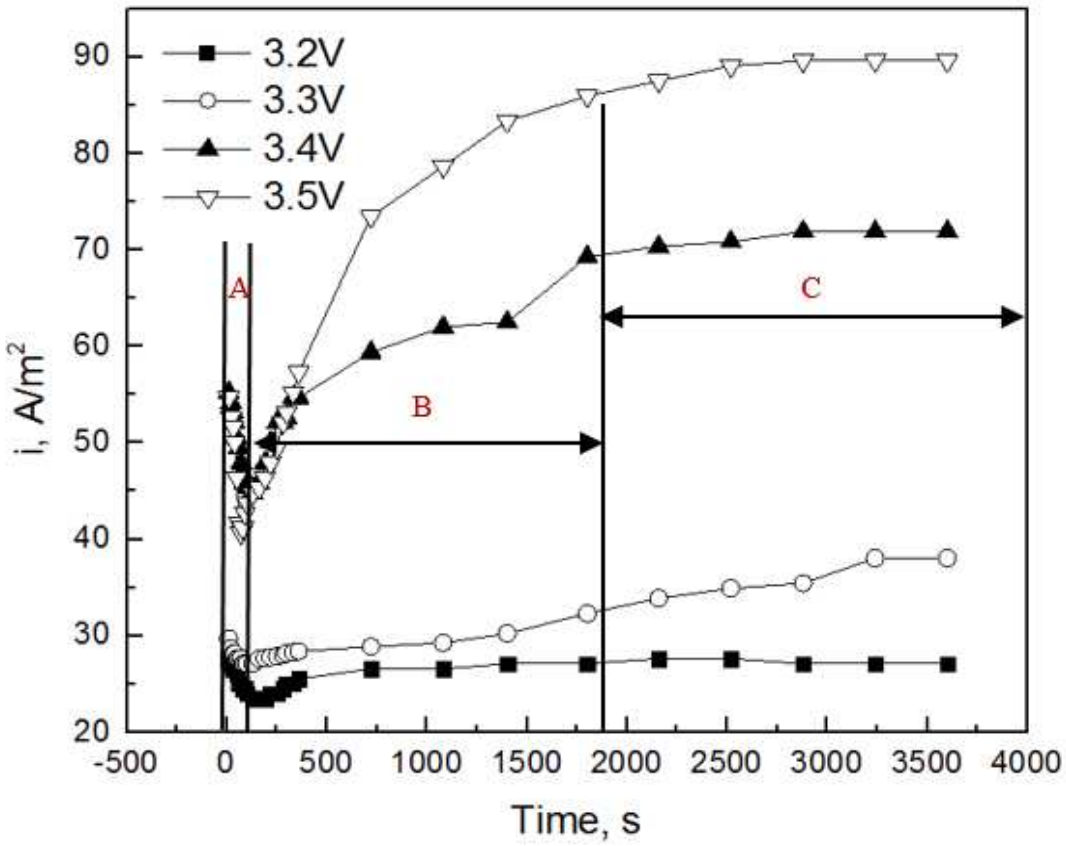

Figure 5.1 Variation of current density with time during electrowinning of Zn in ChCl/2Urea eutectic mixture, at fixed temperature of 90° C at different applied voltages: (■) 3.2V, (○) 3.3V, (▲) 3.4V, (▽) 3.5V; ZnO concentration is 0.41 mol/L

A typical current density against time curve is observed at all applied voltages and can be divided into three sections. A steep decrease marked as section A is observed during the first 50 s. In order to further analyze the reason that causes the sharp decrease, Figure 5.2 is plotted in the first six seconds of the electrowinning process. As seen in Figure 5.2, a short rising trend, which occurred in the first 0.1s of the curve, can be attributed to the nucleation process: the number of nuclei increases with the increase in electroactive area of the electrode. More clearly, it is then followed by a decreasing portion from 0.5s to 6s. The decaying current density is plotted with $t^{-1/2}$ and is found linear as showed in Figure 5.3, which is in agreement with the Cottrell equation given below [**90**] in eq. 5.1:

$$i = nFC\,(D/\pi)^{1/2}\,t^{-1/2} \qquad (5.1)$$

Where i is the current density (A/m^2), t is the time (s), C is the concentration of the solution, n is the number of exchange electrons, D is the diffusion coefficient, F is the Faraday's constant. The diffusion coefficient determined from the slope in Figure 5.3 is 7.85×10^{-13} m^2/s, which is in agreement with the previously reported value (1.89×10^{-12} m^2/s at 100°C), and is in reasonable range compared to other literatures [**69,83]**. The diffusion controlled process occurring in section A is kinetically driven, meaning that the rate of reaction is much higher than the rate of diffusion, creating a concentration gradient between electrode and the solution, and thus concentration polarization is the main reason that leads to the sharp decrease in current density.

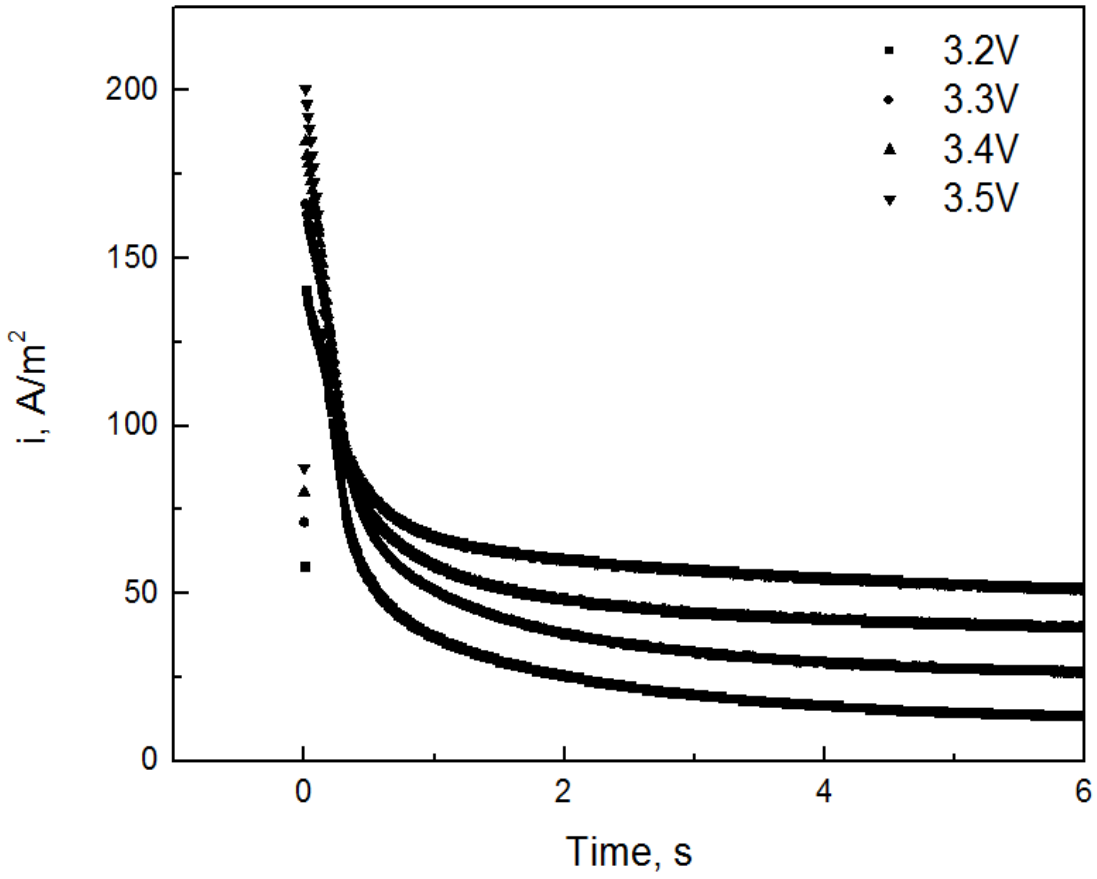

Figure 5.2 Current-time transient for the first 6s at applied voltages: (■) 3.2V, (●) 3.3V, (▲) 3.4V, (▼) 3.5V, at fixed temperature of 90° C

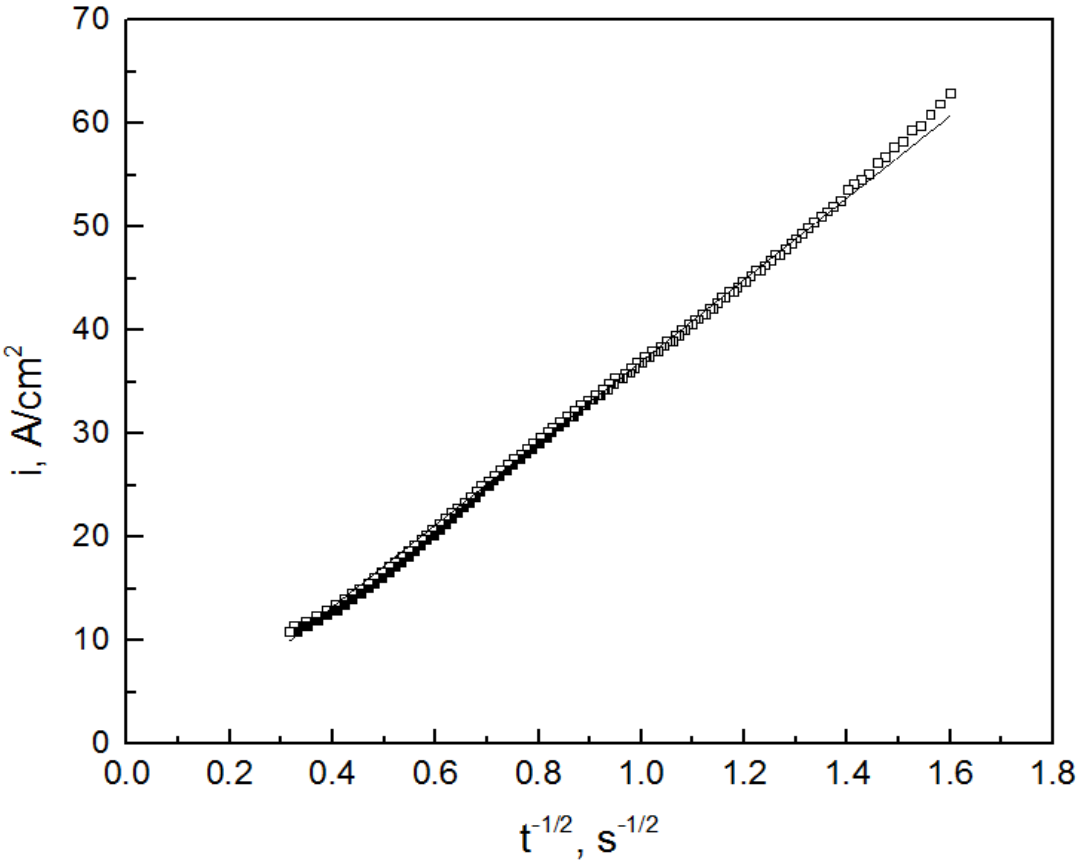

Figure 5.3 Variation of current density as a function of $t^{-1/2}$, data plotted for the decreasing portion of current-time transients at 3.2V, at fixed temperature of 90°C

It is then followed by an increasing portion which shows in section B. The gradual increase in current density is due to the activation polarization at the cathode. Figure 5.4 is shown to confirm activation polarization occurred in this region. Cathodic over-potential is calculated using eq. 5.2:

$$\eta = E^c - E^o \qquad (5.2)$$

where E^c is the cathodic potential (V) measured between cathode and reference, E^o is the equilibrium potential (V) obtained in literature as -1.05V vs. Ag [**69**]. As seen in Figure 5.4, the cathodic current density is plotted as a function of over-potential. A linear relationship is found indicating that activation polarization causes current density to increase in section B [**91**].

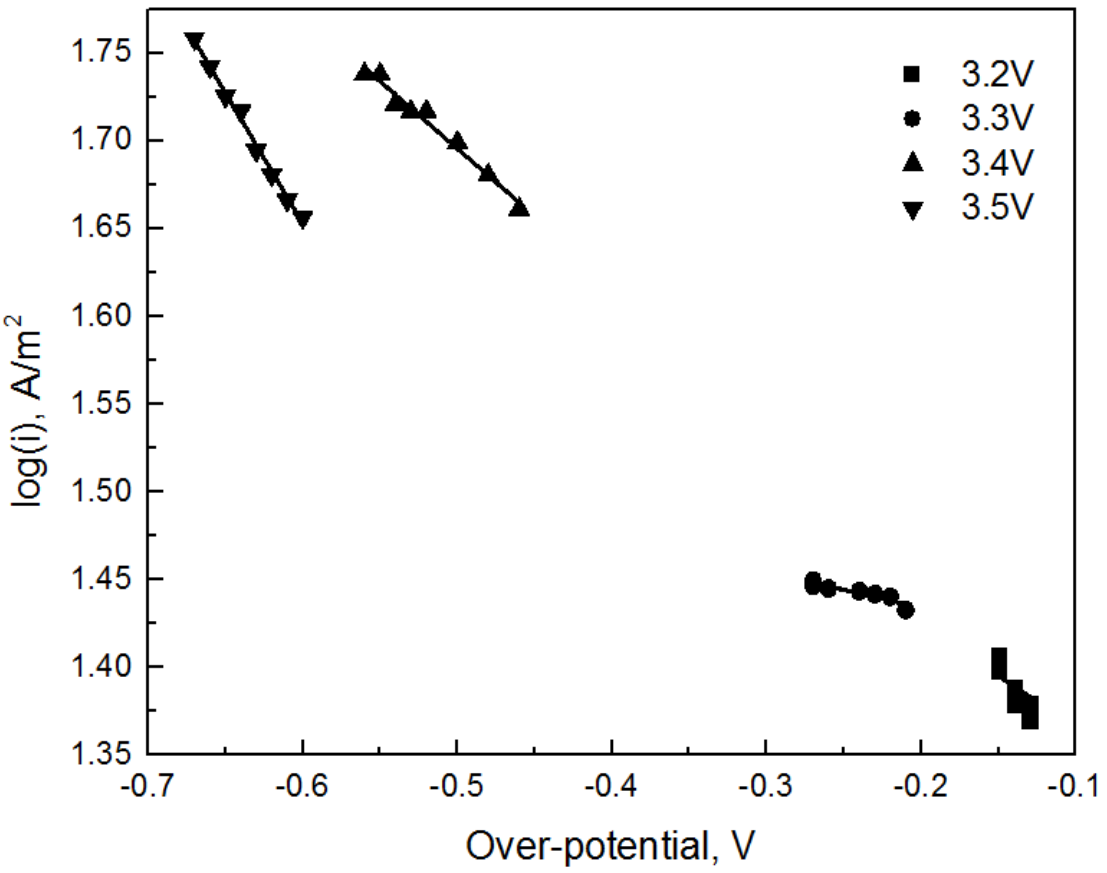

Figure 5.4 Cathodic polarization curve exhibiting the variation of current density as a function of cathodic over-potential in the B section showed in Figure 3 at different applied voltages between cathode and anode (■) 3.2V, (●) 3.3V, (▲) 3.4V, (▼) 3.5V, at fixed temperature of 90°C

These unstable current region can be visualized in Figure 5.5. At the beginning of the reaction, the concentration of electroactive species is very high, thus the reaction rate is much higher than the diffusion rate. The consumed electrons are hardly compensated by diffusion indicating diffusion is governing at this stage. However, with the electrowinning proceeds, the reaction rate is much lower than the initial stage. The consumed electrons can be easily compensated by diffusion and during this period, the reaction activation is predominant.

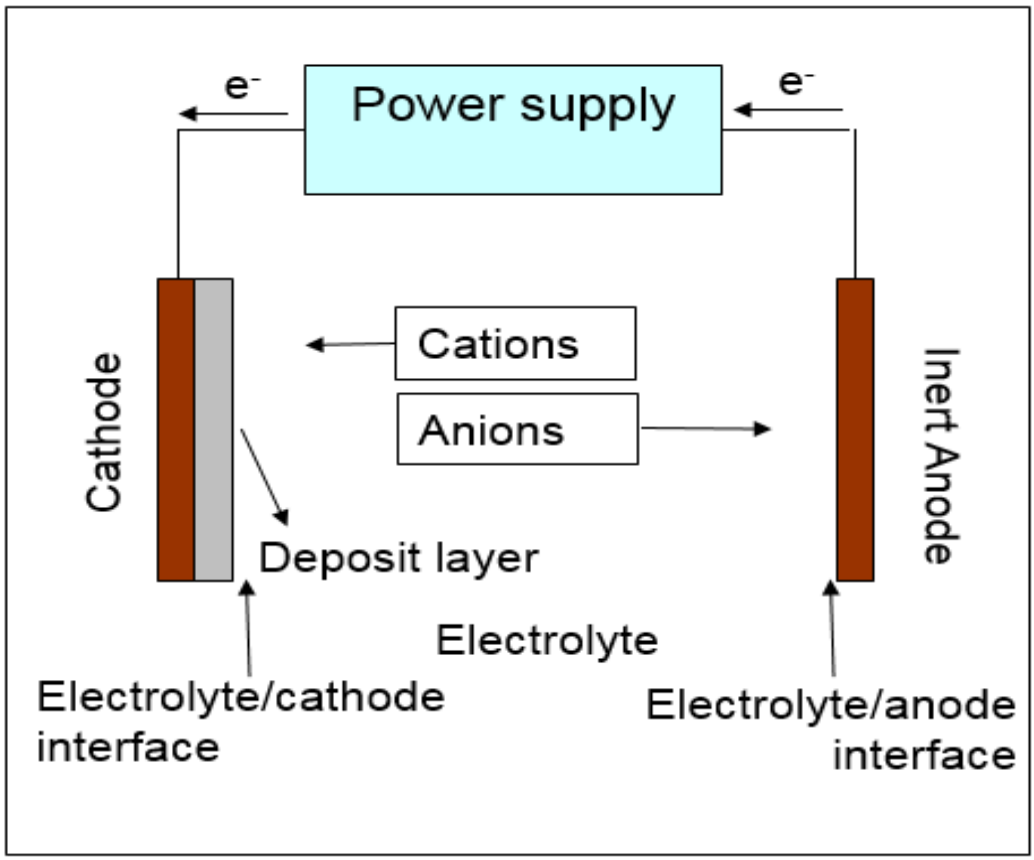

Figure 5.5 Schematic representation of unstable current region

5.3 Kinetic Parameters Investigation

A constant current density over the time in section C is a sign of steady-state electrowinning. To investigate the kinetics of the electrowinning process, Tafel plots are obtained in temperatures from 80 to 100°C using three electrode system after reaching steady-state electrowinning in section C, as shown in Figure 5.6.

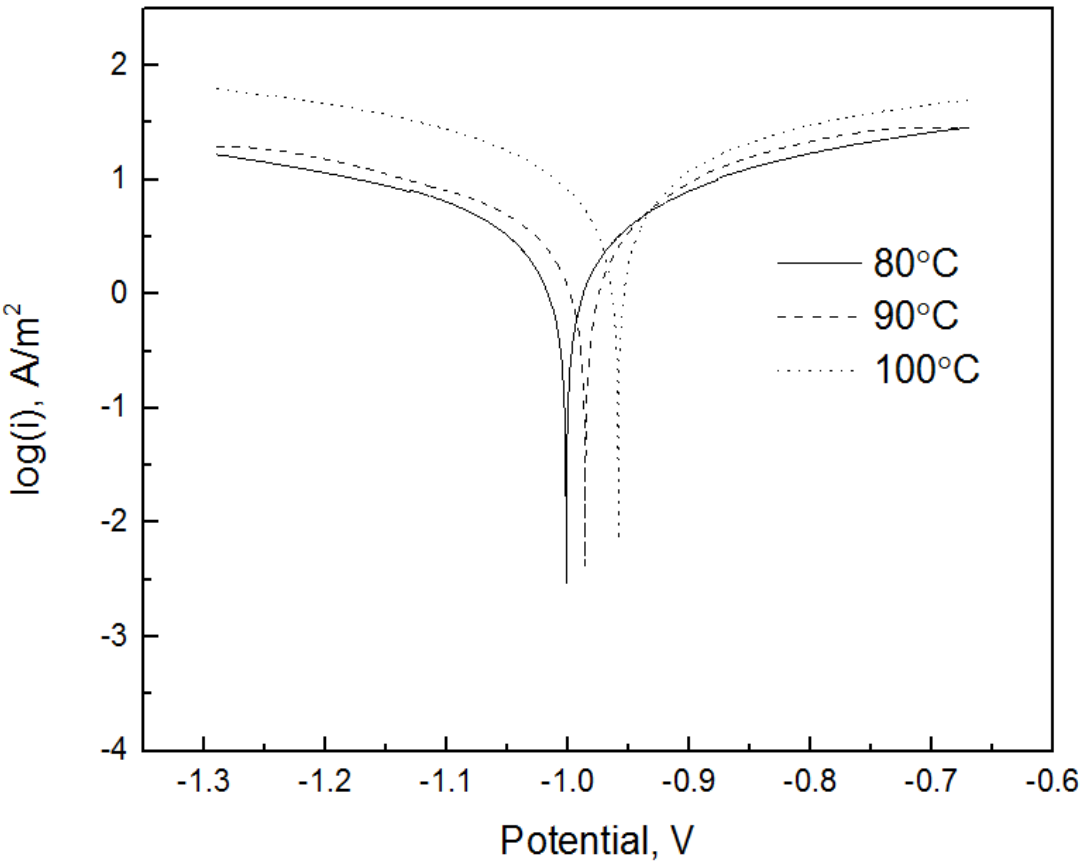

Figure 5.6 Tafel plots obtained from steady-state Zn electrowinning process in temperatures from 80 to 100°C

By extrapolating the extended cathodic and anodic linear Tafel region, the interception gives the equilibrium potential as well as exchange current density, as recorded in Table 5.1. It is seen that the absolute value of equilibrium potential is decreasing, while the exchange current density shows an increasing trend with temperature. Figure 5.7 exhibits the correlation between exchange current density and temperature and a linear behavior is found between $\ln(i_o)$ and 1/T, which can be explained by the Arrhenius equation [**92**]. The activation energy value is 3.85 kJ/mol, which is comparatively low [**93**], reflecting the very active electrode surface as well as the readiness of the reaction. Based on the obtained equilibrium potentials in Table 5.1, cathodic

polarization plots are shown in Figure 5.8 at temperatures from 80 to 100°C. Generally, the linear relationship between cathodic over-potential and current density is represented by Tafel equation, which is expressed as eq 5.3:

$$\log i = \log i_o + \left(\frac{\alpha_c \cdot \mathrm{n} \cdot \mathrm{F}}{2.303\mathrm{RT}}\right) \cdot \eta \qquad (5.3)$$

where η is the cathodic over-potential (V), i is the cathodic current density (A/m^2), R is gas constant, T is the temperature (K), i_o is the exchange current density (A/m^2), α_c is the cathodic charge transfer coefficient, n is the number of transferred electrons, and F is the Faraday's constant. The average transfer coefficient obtained from temperatures 80 to 100°C is approximately 0.2, suggesting an irreversible charge transfer process occurred, with a similar conclusion reached in other literatures [**70,71]**.

Table 5.1 Temperature dependence on equilibrium potential and exchange current density

Temperature (°C)	E^o (V)	log i_o	i_o (A/m^2)
80	-1.0290	0.7687	5.8708
90	-0.9775	1.0147	10.3442
100	-0.8958	1.2740	18.7931

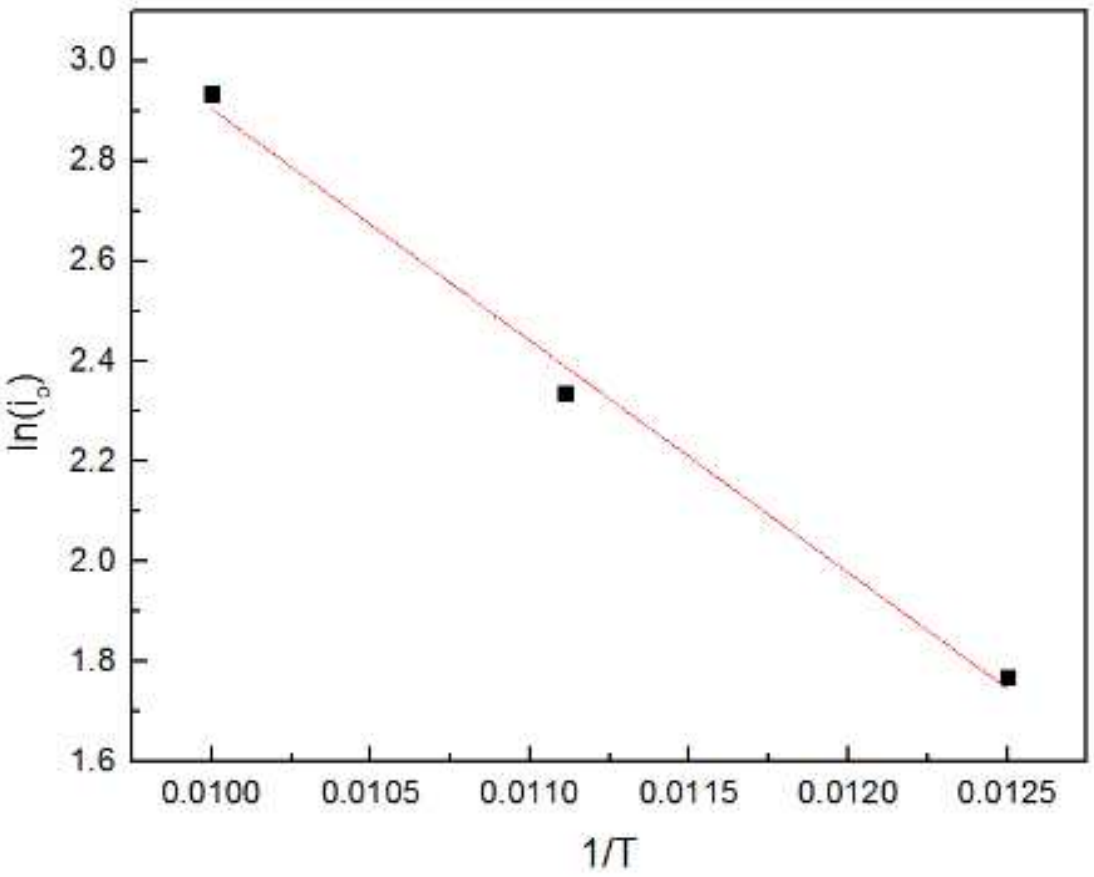

Figure 5.7 Arrhenius plot for natural logarithm of exchange current density and inverse temperature

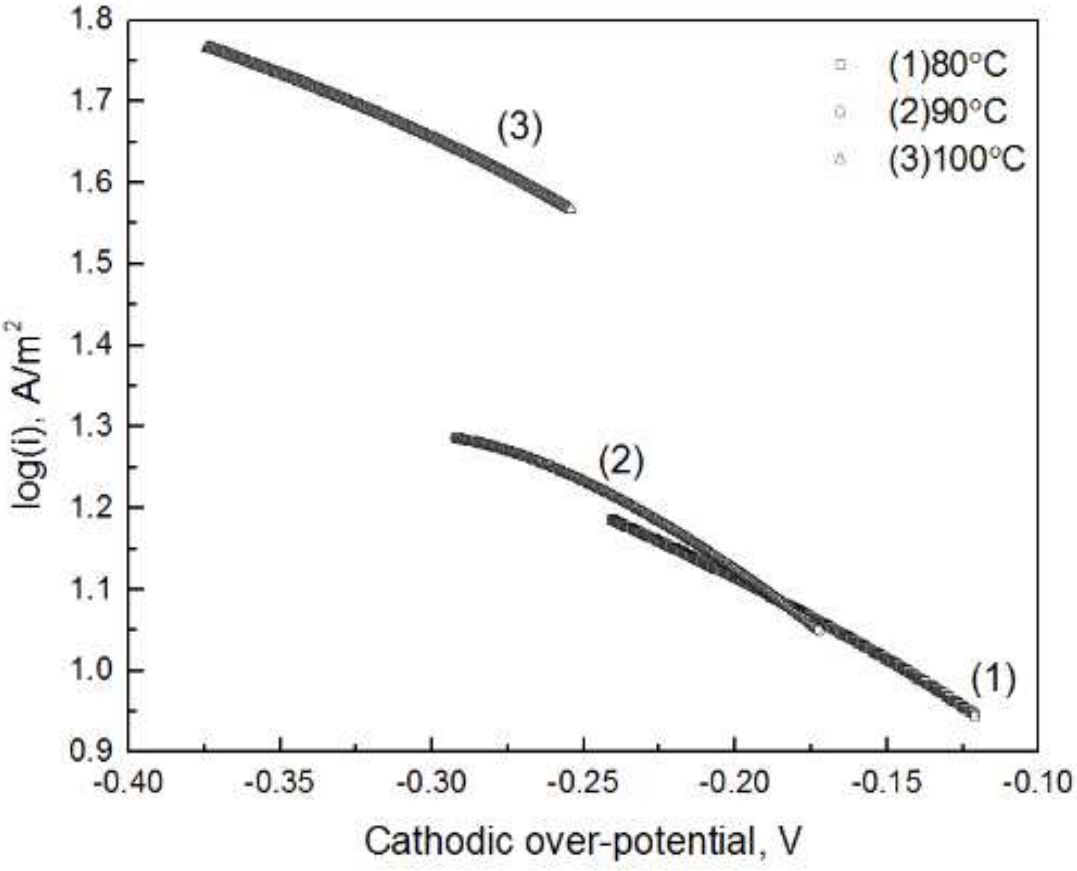

Figure 5.8 Cathodic polarization plots during steady-state electrowinning process at various temperatures: (1) 80°C, (2) 90°C, (3) 100°C

5.4 Effect of Applied Voltage on Microstructure

The effect of applied voltage on microstructure is shown in Figure 5.9. At lower applied potential as seen in Figure 5.9a, the deposited layer is dense and uniform with an average particle size of 1 μm. At this stage, a reduction-controlled growth can be visualized in that the loss of Zn^{2+} on the electrode surface can be quickly compensated by diffusion. As a result of that, formed crystals are surrounded by sufficient Zn^{2+} ions that are ready to be reduced and form a shape with minimum surface energy. As the potential reaches a more negative value of 3.3V (Figure 5.9b), significant grain growth is found for the typical hexagonal chunks that lie above the dense layer,

with an approximate size of 10 μm. In Figure 5.9c, agglomeration of Zn particles is observed without any further growth in grain size. However, it is seen that the individual particles split into small plate-like structures that are aligned perpendicular to the surface of the substrate. Moreover, as the potential increases to 3.5V, the perpendicular growth of the platelets is significant which changes the morphology from a granular structure to dendritic.

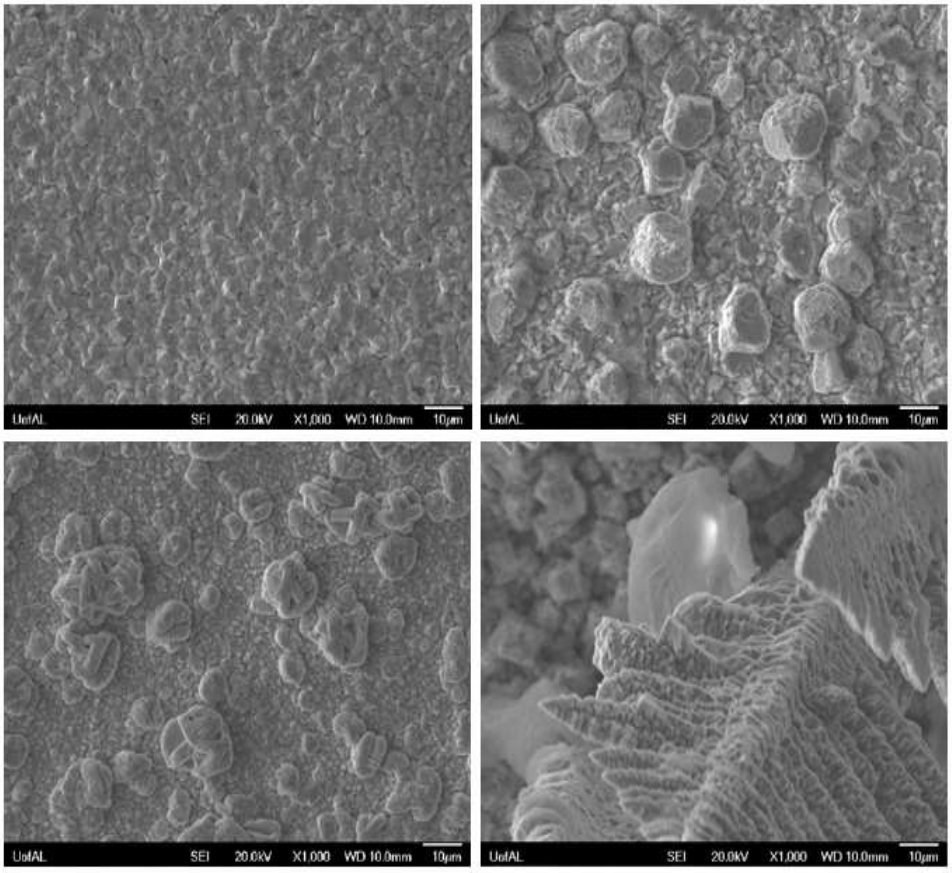

Figure 5.9 Effect of applied potential on deposits surface morphology: (a) 3.2V, (b) 3.3V, (c) 3.4V, (d) 3.5V, at fixed temperature of 90°C

The cross-sectional SEM micrographs are shown in Figure 5.10 to provide a direct comparison before and after forming dendritic zinc. It is a particular feature for a hexagonal close packed (hcp) lattice since the growth along a high-index axis is much more significant than low

index, leading to an extended growth from one-dimensional nucleation mechanism [**94**].The over-potential is measured and equal to -0.65V when applied voltage is 3.5V and this over-potential is considered to be above the critical over-potential (ηcrt) on which dendritic growth initiates. When extra over-potentials are provided, a depletion zone forms on the surface of the electrode because ions are consumed quicker than the complement by mass transfer, which indicates that the growth of the particles is now governed by diffusion [**95**].

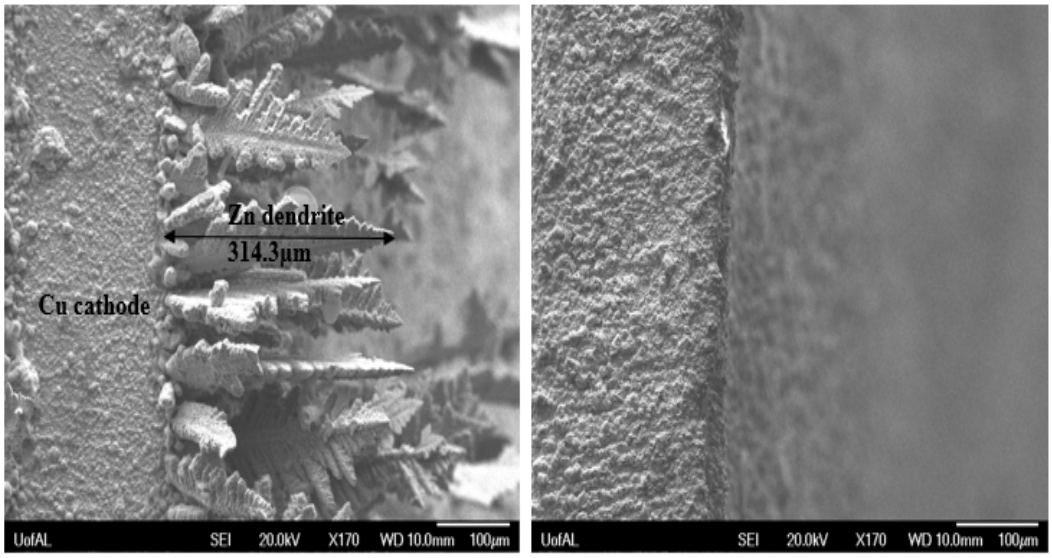

Figure 5.10 Cross section morphology of zinc deposition on copper cathode: (a) 3.5V; (b) 3.4V, at a fixed temperature of 90°C

5.5 Critical Over-potential for Zn Dendrite Formation

Further calculation of critical over-potential (η_{crt}) was carried out using eq. 5.4 [**96**]:

$$\eta_{crt} = \frac{RT}{\alpha F} ln\left(\frac{i_L \delta}{i_o h}\right) \qquad (5.4)$$

Where h is the average height of the growing dendrite measured from Figure 5.10a that is equal to 314.3 μm, δ is the diffusion layer thickness, i_o is the exchange current density which is obtained from Table I to be 10.3442 A/m^2, α is equal to 0.2, and temperature is 363K. The product of $i_L \cdot \delta$ can be calculated from eq. 5.5 **[97]**:

$$i_L = \frac{nFDC}{\delta} \qquad (5.5)$$

Where n is the number of transferred electrons, D is calculated to be 7.85×10^{-13}m^2/s, F is the Faraday constant, and C is bulk concentration of electro-active species which is equal to 0.41mol/L.

The minimum over-potential for initiation of dendritic formation is given when h is equal to δ. Eq. 5.4 and 5.5 combining yields the calculated value of η_{crt} is -0.62V. It is less than the measured over-potential of -0.65 which explains the dendrites form beyond the critical point. The calculated critical over-potential for dendrite formation of different metal is compared in Table 5.2. [**91,98-99]**. It is seen that η_{crt} of Zinc is smaller than that of Aluminum at given temperature. The reason can be due to the difference in the diffusion coefficient. In addition, zinc critical value is only -0.173V reported by Popov reflecting that dendrites are much easier to form in aqueous solution and at lower temperatures.

Table 5.2 Comparison of critical over-potential of dendrite formation for different metal deposits

Metals	Electrolytes	η_{crt}	Temp	D	Ref
Al	$AlCl_3$-EMIC	-0.536V	90°C	6.89×10^{-11}m^2/s	[91]
Zn	Urea/ChCl	-0.62V	90°C	7.85×10^{-13}m^2/s	This work
Cu	H_2SO_4	-0.65V	25°C	-	[98]
Zn	H_2SO_4	-0.173V	25°C	-	[99]

5.6 Current Efficiency and Energy Consumption

Cathodic current efficiency (η) is defined as the percentage of the actual obtained amount of zinc deposits to theoretically calculated zinc amount. The experimental weight gain (ΔW) can be obtained by measuring weight difference of the cathode before and after electrowinning (ΔW=Wfinal – Winitial). The theoretical weight gain (Wt) of deposited zinc is calculated by using Faraday's law:

$$W_t = \frac{itaA}{nF} \qquad (5.6)$$

Where i is the current density that passes through electrodes (A/m^2), t is the time (s), a is the atomic weight of the deposits (g/mol), A is the area of electro-active region on the electrode (m2), n is the number of transferred electrons which is equal 2 in the studied system, and F is Faraday constant. The product of i·t is calculated from the total area under the current density against the time curve. The current efficiency can be calculated from the equation as follows:

$$\eta = \frac{\Delta W}{W_t} \times 100\% \qquad (5.7)$$

Energy consumption in the process of electrowinning of Zn is determined using eq. 5.8:

$$E = \frac{VQ}{\eta} \qquad (5.8)$$

Where V is the applied voltage between anode and cathode, Q is the total charge required to get specific amount of deposits on the basis of faraday's law, and η is the current efficiency.

5.6.1 Effect of Cell Voltage

The calculated energy consumption under applied voltages from 3.2 to 3.5V varies from 3.04 to 3.66 kWh/kg and current efficiency is from 78.5 to 88.9%, as summarized in Table 5.3 and Figure 5.11 and 5.12. The calculated efficiency and power consumption value fall close in lower voltages (from 3.2 to 3.4V). However, an obvious decrease in current efficiency as well as an increase in energy consumption is observed at higher voltage of 3.5V. At this potential, total charges that pass through the electrochemical cell increase and thus theoretical weight gain is increased as well. Nevertheless, the actual weight of deposited zinc is lower than expected, as major current is lost during the electrolysis process due to the strong effect of polarization and co-deposition of hydrogen.

Table 5.3 Summarization of current efficiency and energy consumption in different applied voltages, at fixed temperature of 90°C

Applied Voltage (V)	ŋ (%)	E (kWh/kg)
3.2	86.2	3.04
3.3	88.9	3.05
3.4	87.7	3.18
3.5	78.5	3.66

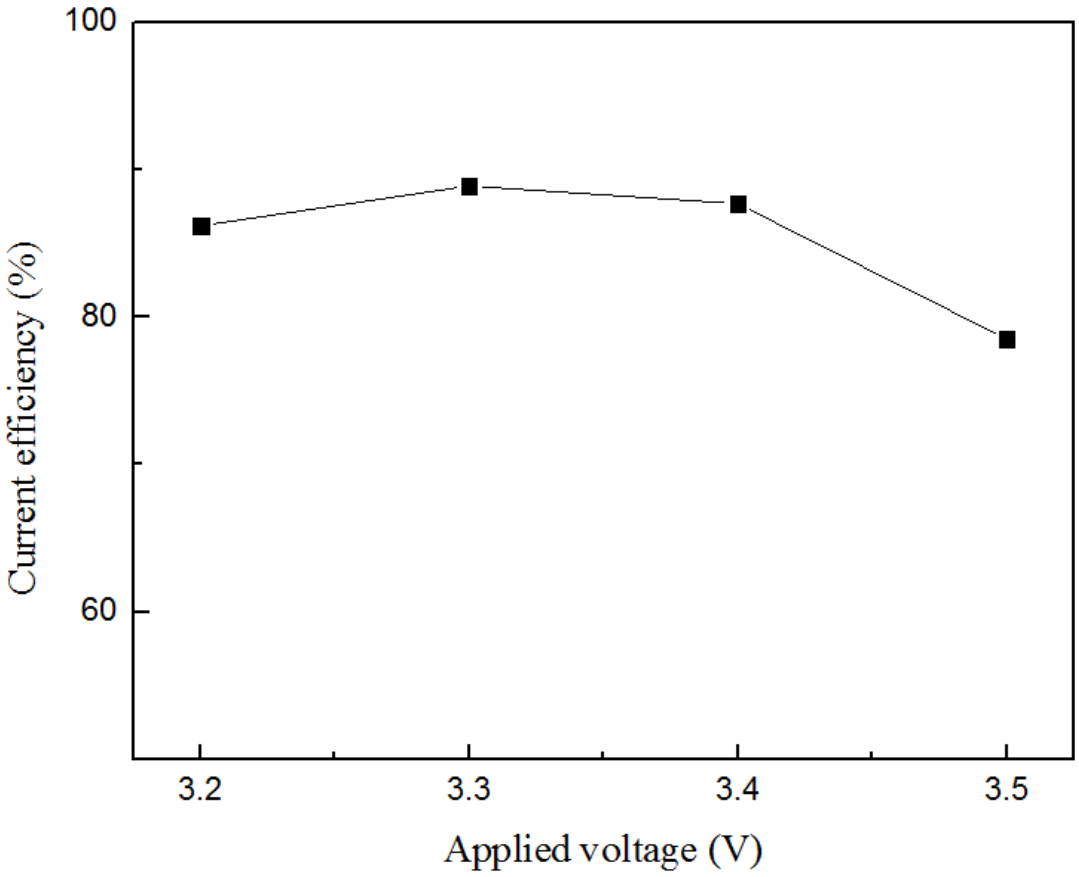

Figure 5.11 Variation of current efficiency with applied cell voltage at a temperature of 90°C

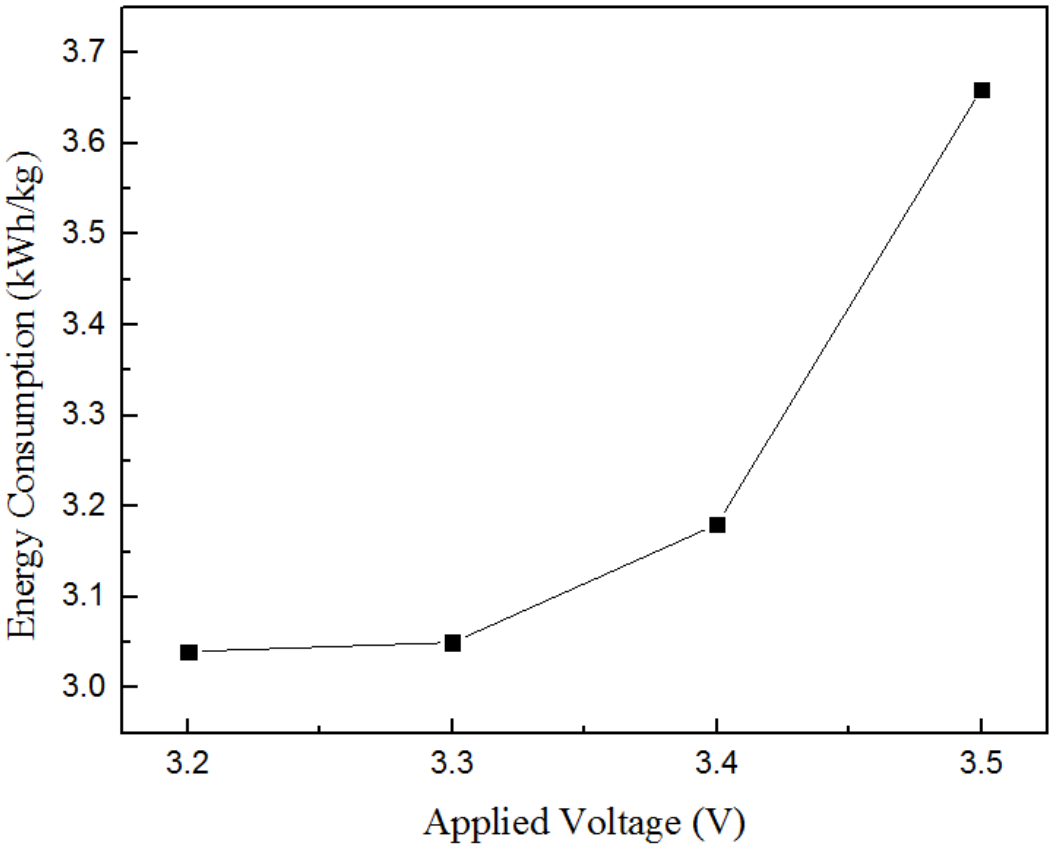

Figure 5.12 Variation of energy consumption with applied cell voltage at a temperature of 90°C

5.6.2 Effect of Temperature

Temperature is an important variable that has significant influence on current efficiency and energy consumption. Table 5.4 summarizes the current efficiency as well as energy consumption calculated at temperatures from 70 to 115°C with a fixed voltage of 3.3V. Their variation with temperature can be observed in 5.13 and 5.14 respectively. The current efficiency increases 15.1% by increasing temperature from 343 to 358K and further increases 1.4% from 358K to 373K. However, there is a decrease in current efficiency by 13.7% from 373K to 388K which might be due to decomposition of ionic liquid at elevated temperature. In addition, it is seen

that the electrodeposition process was enhanced between 358K and 373K by achieving lower power consumption from 2.69 to 2.74kWh/kg.

Table 5.4 Summary of current efficiency and energy consumption at different temperature

Temperature(K)	ŋ (%)	E(kWh/kg)
388	77.6	3.17
373	91.3	2.69
358	89.9	2.74
343	75.8	3.24

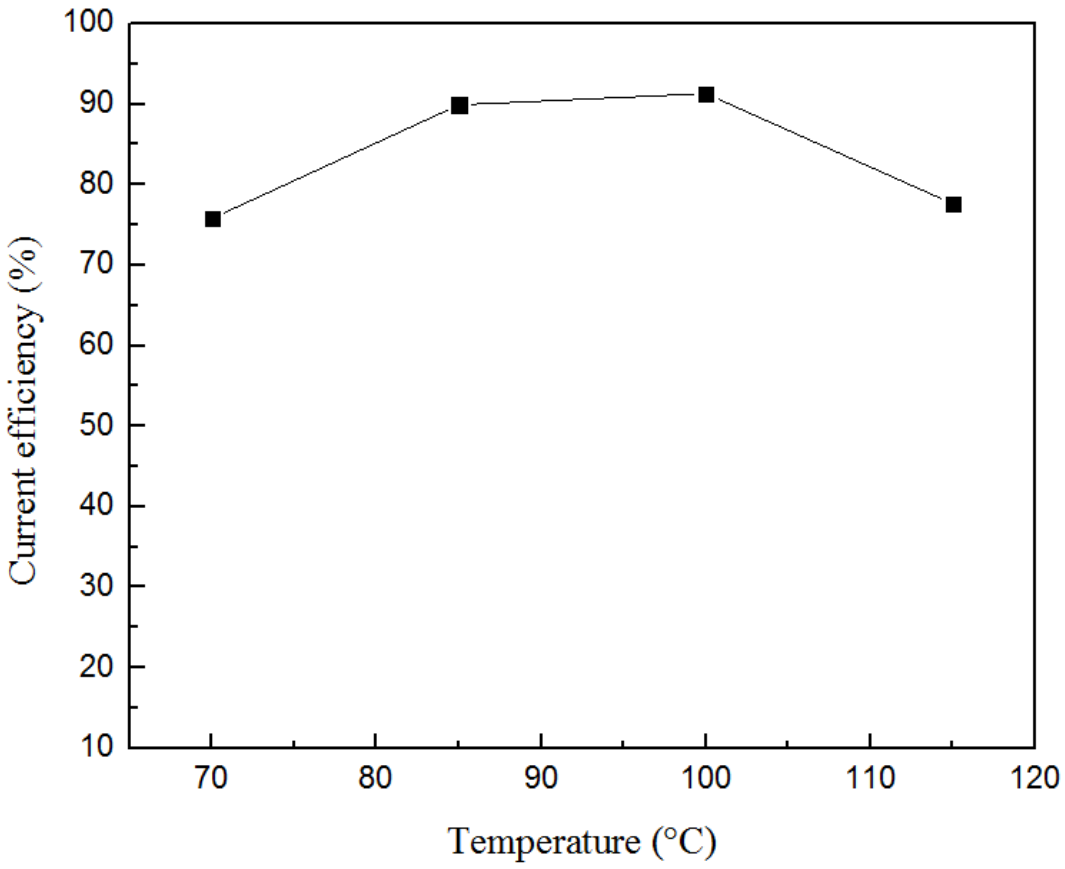

Figure 5.13 Variation of current efficiency with temperature with a fixed cell voltage of 3.3V

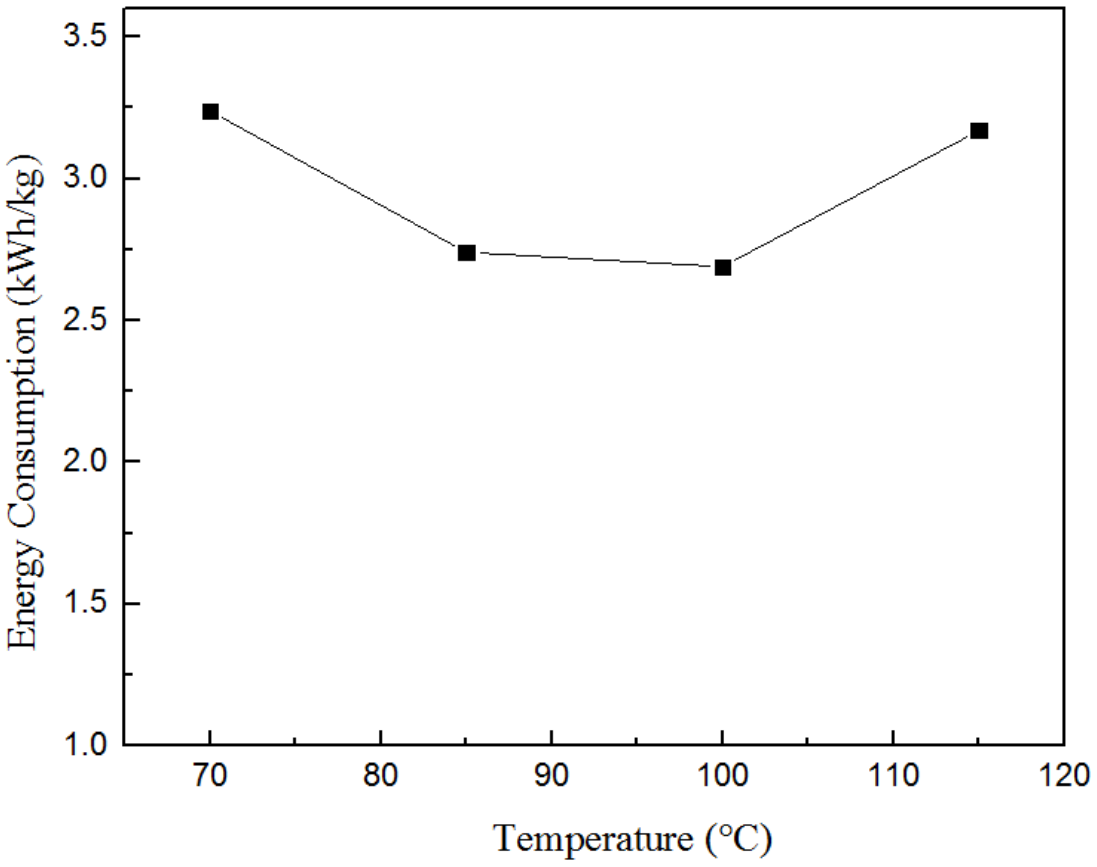

Figure 5.14 Variation of energy consumption with temperature with a fixed cell voltage of 3.3V

5.6.3 Effect of [Bmim]HSO_4 as Electrolyte Additive

The effect of concentration of [Bmim]HSO_4 as electrolyte additive is discussed and results are summarized in Table 5.5, Figure 15 and 16. With increasing concentration of [Bmim]HSO_4, the activity of ions suddenly increase leading to a higher current flow between electrodes. As a result, theoretical weight and current efficiency are enhanced. However, excess amount of additive inhibits the reaction as a efficiency drop from 92.6% to 89.5% was observed with 3.0 mg/mL of [Bmim]HSO_4.

Table 5.5 Summary of current efficiency and energy consumption with different concentration of [Bmim]HSO_4, at 100°C, with a voltage of 3.3V

Additives (mg/mL)	ŋ (%)	E (kWh/kg)
1.0	88.4	3.06
1.5	89.5	3.02
2.0	92.6	2.92
3.0	89.5	3.03

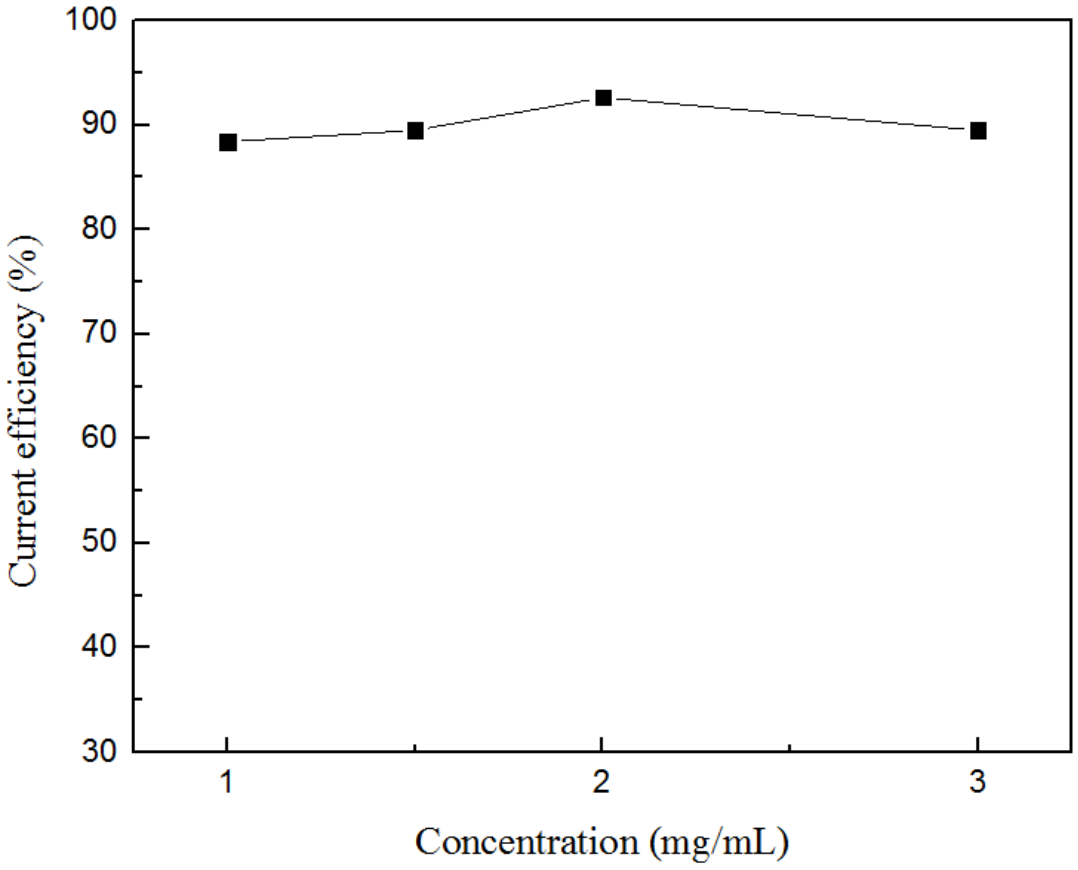

Figure 5.15 Variation of current efficiency with additive concentration at 100°C with a fixed cell voltage of 3.3V

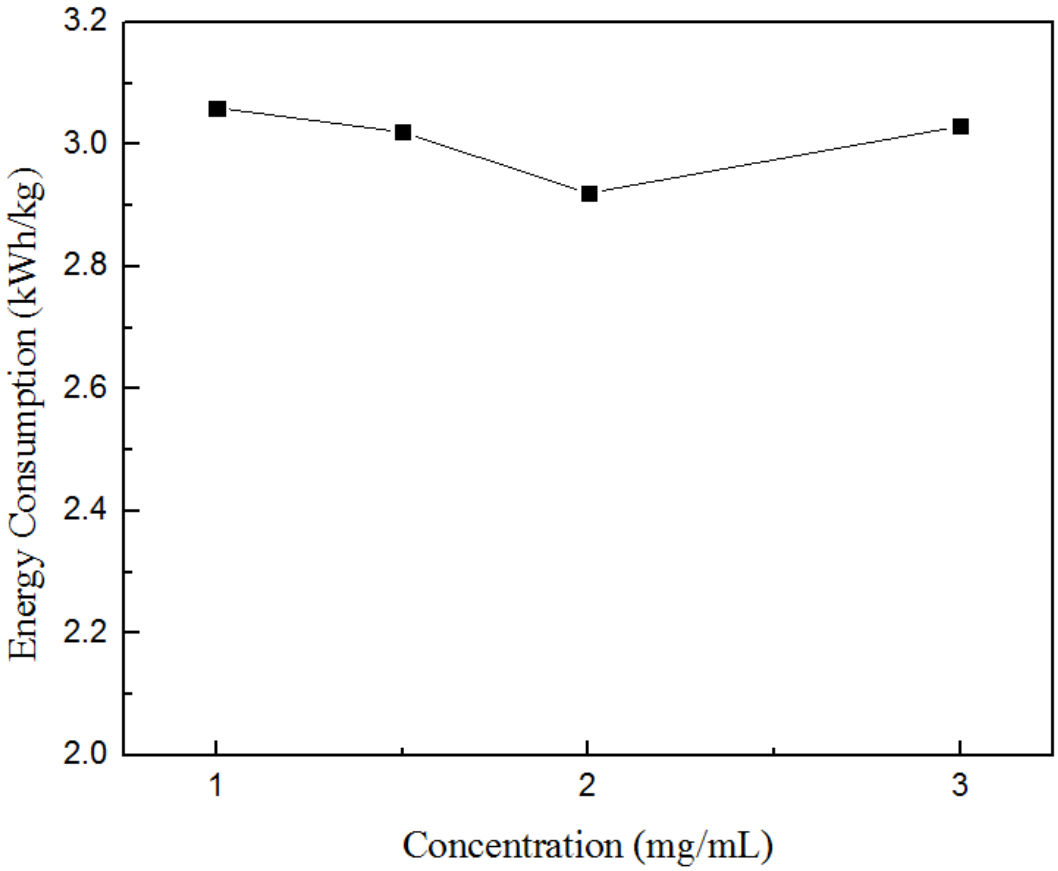

Figure 5.16 Variation of energy consumption with additive concentration at 100°C with a fixed cell voltage of 3.3V

5.6.4 A Direct Comparison between Zn Electrowinning in Ionic Liquid and Conventional Zn Electrolytic Process in Acidic Solution

A direct comparison of parameters involved in Zn electrowinning is given for electrolytic process in ionic liquid and sulfuric acid solution. Although the urea and choline chloride mixture is more costly than sulfuric aqueous solution, Zn electrowinning in ionic liquid is promising since energy consumption is lower and current efficiency is higher in optimized experimental conditions compared to those for conventional zinc electrowinning in sulfuric acid (~3.26 kWh/kg). Moreover, the only gas emission is O_2 which means our system is environmental friendly and it is feasible to

obtain high pure of zinc with further purification. A practical difficulty to overcome in the future is to reduce viscosity. Viscosity of DES is generally ten times larger than aqueous solution at room temperature. At current stage, viscosity can be effectively reduced by increasing temperature or with addition of water content.

Table 5.6 Comparison between zinc electrodeposition processes in studied ionic liquid and industrial zinc production process in acidic solution

Parameters	Zn Electrowinning in Ionic liquids (This study)	Conventional Zn Electrowinning in sulfuric acid
Cell voltage (Volts)	***3.2-3.5***	~3.5
Current density (A/m^2)	***5-130***	500
Energy consumption (kWh/kg)	***2.69-3.66***	~3.26
Current efficiency (%)	***Up to 92.6%***	~90%
Temperature	***70-115°C***	Room temperature
Gas release	***O_2***	SO_2
Raw material	***ZnO***	Zinc contained ore

CHAPTER 6

BATCH RECIRCULATION ELECTROWINNING OF ZINC

6.1 Batch Recirculation Electrowinning of Zn

In previous chapter, a number of parameters influencing the zinc electrowinning process in terms of current efficiency, energy consumption and surface morphology were investigated. Zinc has been successfully deposited at temperatures from 70 to 115°C with fixed applied voltages from 3.2 to 3.5V, with addition of [Bmim]HSO_4. This chapter explores the feasibility of this technology of low temperature zinc electrowinning in Urea/ChCl eutectic mixture in large scales, especially in batch mode. The study of large scale zinc electrowinning in batch recirculation system helps to overcome several major difficulties to the ionic liquids application. Well-designed batch recirculation ionic liquid flow system under industrial operating conditions is of vital importance to promote the application of ionic liquids in nowadays situation. The schematic and actual design of batch recirculation experiment were shown in Chapter 3. Several aspects will be considered in large scale experiments:

1. To investigate the feasibility of continuous zinc electrowinning.

2. To adapt and address possible process upsets as well as disturbances upon the usage of ionic liquid in the recirculation system based on the study of flow velocity and temperature distribution of the system.

3. To obtain energy consumption, current efficiency and other important results for the comparison with lab-scale zinc electrowinning experiment.

6.2 Effect of Electrowinning Duration

Electrowinning duration is the main variable to investigate the feasibility of the large scale application of room temperature deep eutectic solvent for zinc electrowinning. In this study, the temperature is taken at 90°C and voltage is fixed at 3.3V. Recirculation of the electrolyte achieves by maintaining a constant flow rate of 5 mL/min. Other experimental parameters are described in Table 3.2. Theoretical weight gain on the cathode comes from the accumulation of Zn deposits and is calculated using eq. 5.6. It is seen from Figure 6.1 that a linear increase in theoretical weight is expected and is mainly due to the linear diffusion in the studied electrolyte.

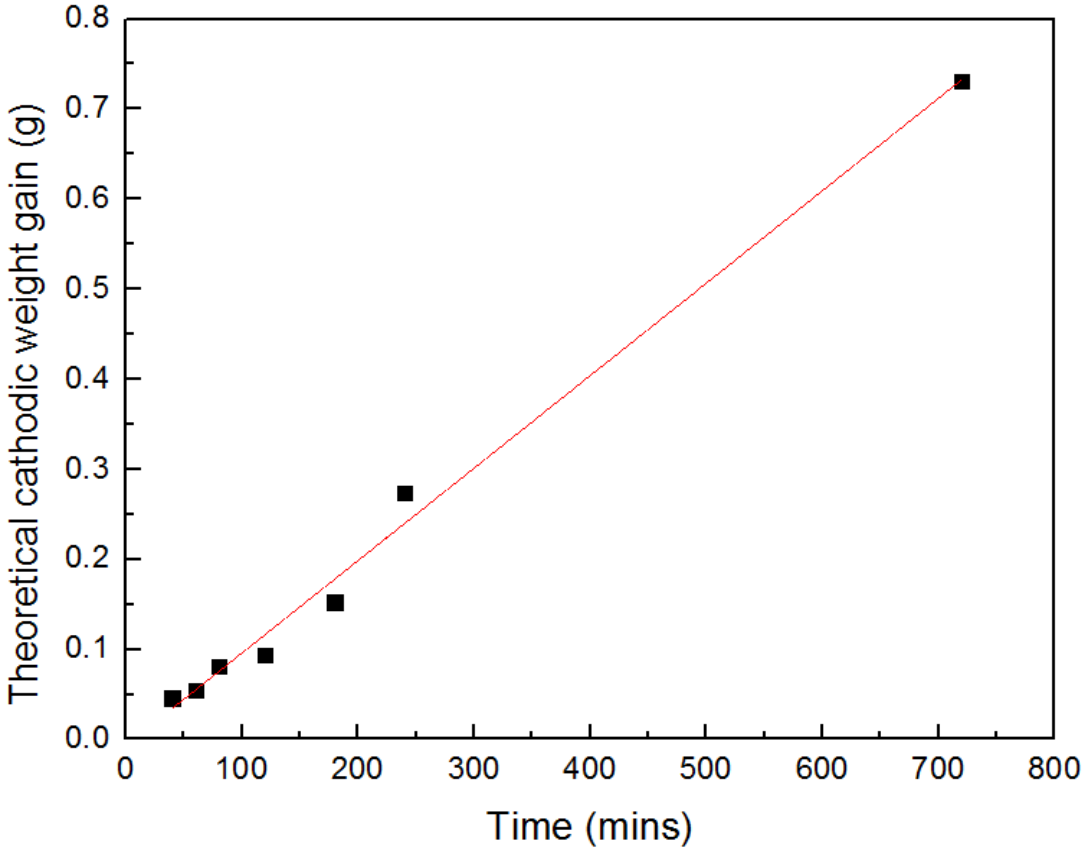

Figure 6.1 Theoretical weight gain at the cathode at different electrowinning duration

Similarly, the actual weight increase is taken from measurement of the weight difference on the cathode before and after electrowinning. As expected, it exhibits the same profile with theoretical weight gain.

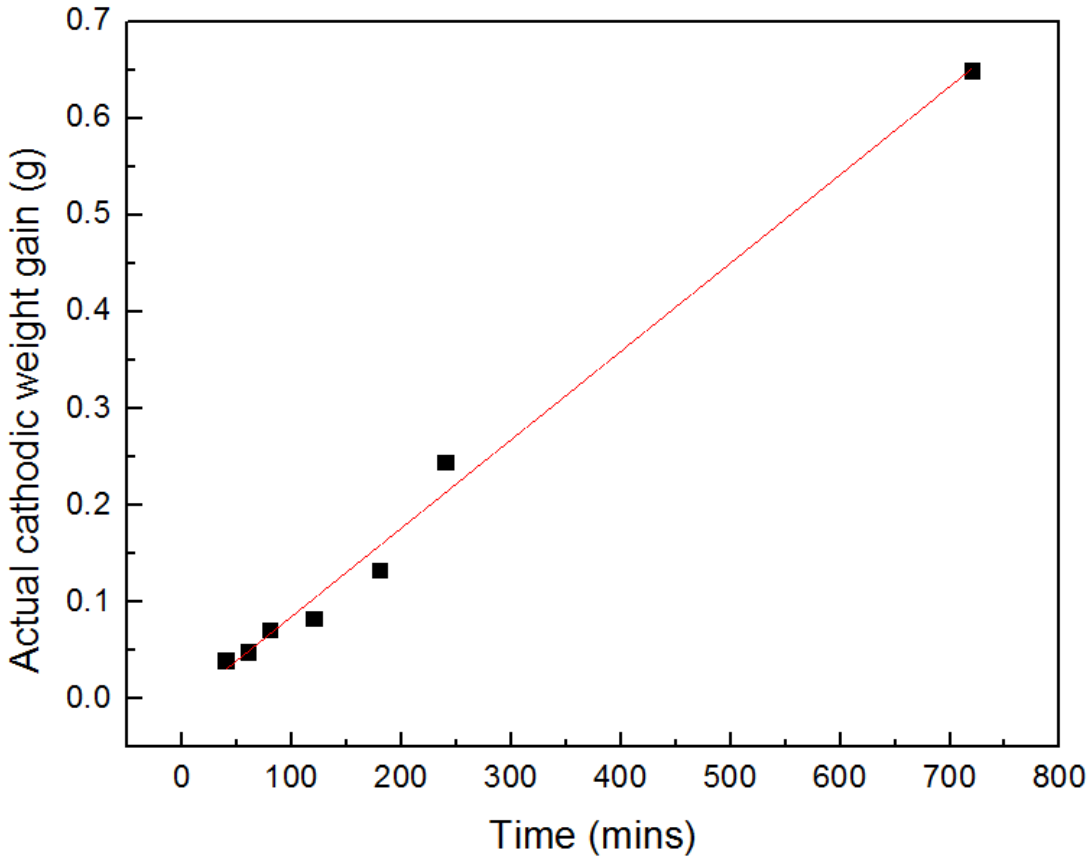

Figure 6.2 Actual weight increase at the cathode at different electrowinning duration

The current efficiency is therefore calculated with an average value of 88.8 ± 0.1% irrespective of electrowinning time, as described in Figure 6.3.

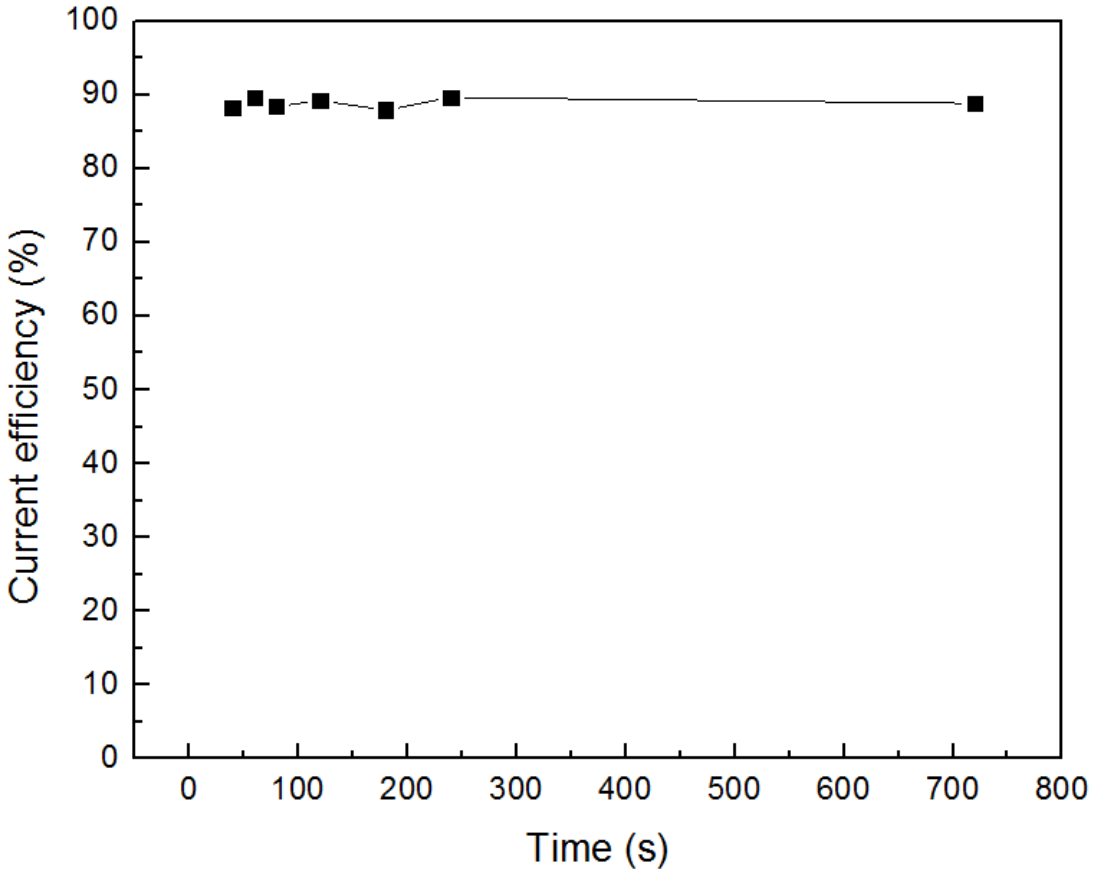

Figure 6.3 Cathodic current efficiency variation with electrowinning time

Correspondingly, the energy consumption is calculated to be 3.23 ± 0.03 kWh/kg which shows reasonable agreement with results calculated in small scale electrowinning.

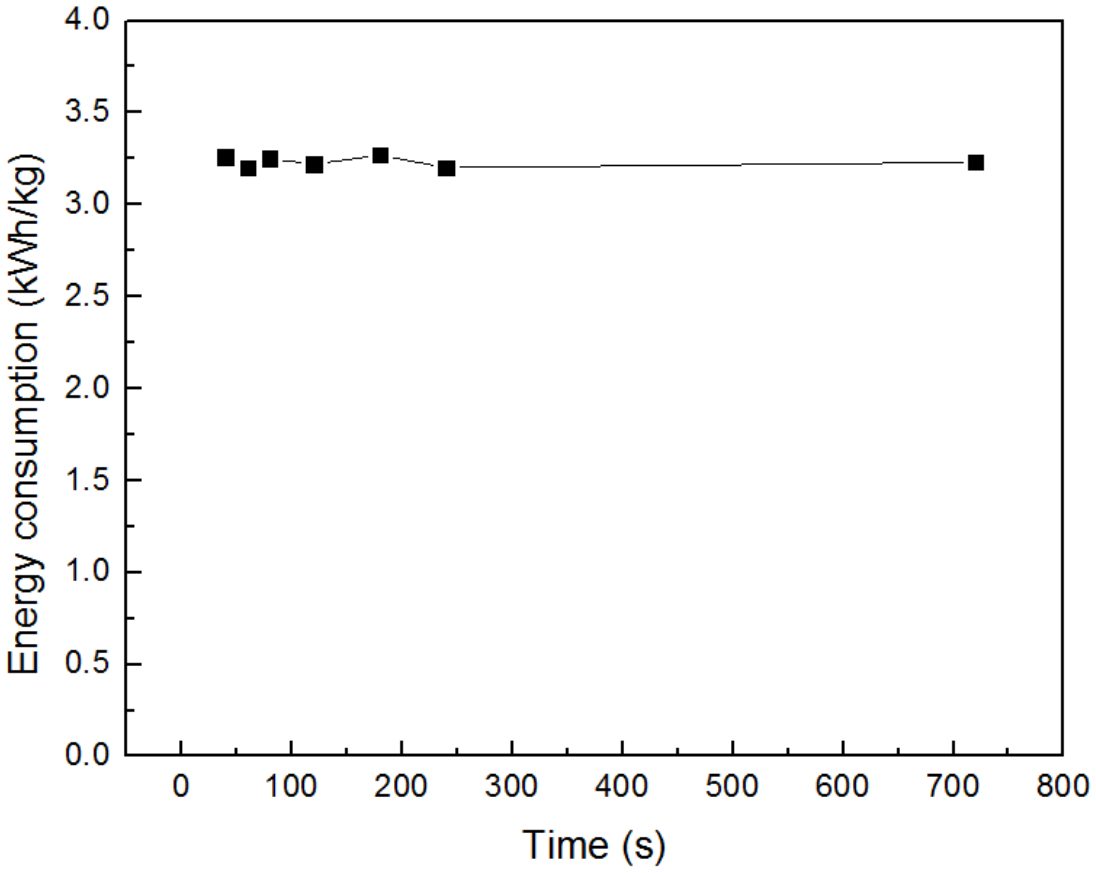

Figure 6.4 Energy consumption variation with electrowinning time

The rate of cathodic weight gain is equal to 9.01 $\times 10^{-4}$ g/min at given condition. In addition, the graphite anode is proven to be stable during the long-term electrowinning as the rate of anodic weight loss is equal to 5.82×10^{-5} g/min which is an order of magnitude smaller than cathodic weight gain and this explains that the oxygen release on the anode only practices small impact on the carbon dioxide conversion on the anode, further confirming the viability of this zinc electrowinning in ionic liquid to be green and economically benign. Table 6.1 summarizes the experimental outcomes as discussed above.

Table 6.1 Summary of the experimental outcomes obtained for large scale zinc electrowinning

Rate of cathodic weight gain (g/min)	Rate of anodic weight loss (g/min)	Average current efficiency (%)	Average energy consumption (kWh/kg)
9.01×10^{-4}	5.82×10^{-5}	88.8 ± 0.1	3.23 ± 0.03

6.3 Mathematical Modeling of Zinc Electrowinning

A 3-D mathematical model was developed for the batch zinc electrowinning reactor using Urea/ChCl low temperature electrolyte. This model describes the deposition process by incorporating the mass transport of participating ionic species, homogeneous chemical reactions within the diffusion layer, and the associated electrochemical kinetics. Process parameters and fluid flow distribution are evaluated for the optimal performance of the batch electrowinning cell.

6.3.1 System Description and Assumptions

The electrochemical deposition in a flowing electrolyte is complex process. The effect of the flow field on the electrode reaction is the result of combination of three types of mass transport of electroactive species, namely, diffusion, convection and migration. The electrowinning efficiency and deposit quality are determined by the cell configuration, and operation conditions. One way to facilitate the advancement of this technology is to establish a physical model of transport process. Details of assumptions made in developing the model for electrowinning reaction are described below [**100**]:

(1) Ionic liquid electrolyte is treated as a homogeneous solution;

(2) Isothermal conditions exist, and side reactions are neglected;

(3) Possible bubble generation from the electrode surface is not considered;

(4) Volume changes in the operation are neglected

(5) A steady state laminar fluid is assumed, the velocity profile is fully developed at the electrode/electrolyte interface; in other words, there is no end effect

(6) Physical and transport properties are constant

Parameters and material constants used in modeling are summarized in Table 6.2.

Table 6.2 Parameters and material constants used in modeling work

Properties (Room Temperature)	Electrode		2Urea/1ChCl eutectic mixture
	Copper cathode [**101**]	Graphite anode [**102**]	
Density (g/m^3)	8.94	2.25	1.25
Specific heat (J/kg·K)	385	669	181.4
Molecular weight (g/mol)	63.55	12.01	86.58
Viscosity (cP)	-		750
Flow rate (mL/min)	-		5

6.3.2 Geometry Model

In order to predict the possible disturbances and upsets in the recirculating flow system, Ansys FLUENT modeling is employed to investigate the fluid flow velocity distribution in the zinc electrowinning cell. In this study, the geometry model has been successfully established based upon the experimental design. Ansys Gambit 2.4 was utilized to construct 3D geometries and mesh the domains. All the geometries are based on actual aspect ratio of batch electrowinning cell designed in experiments. Non-structured meshes were utilized to scrutinize the domain in order to solve continuity and momentum equations in an algebraic method.

(a)

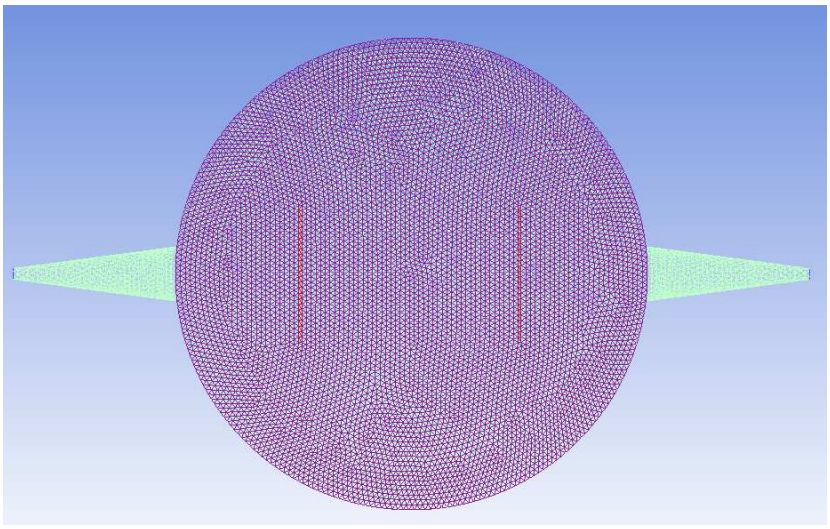

(b)

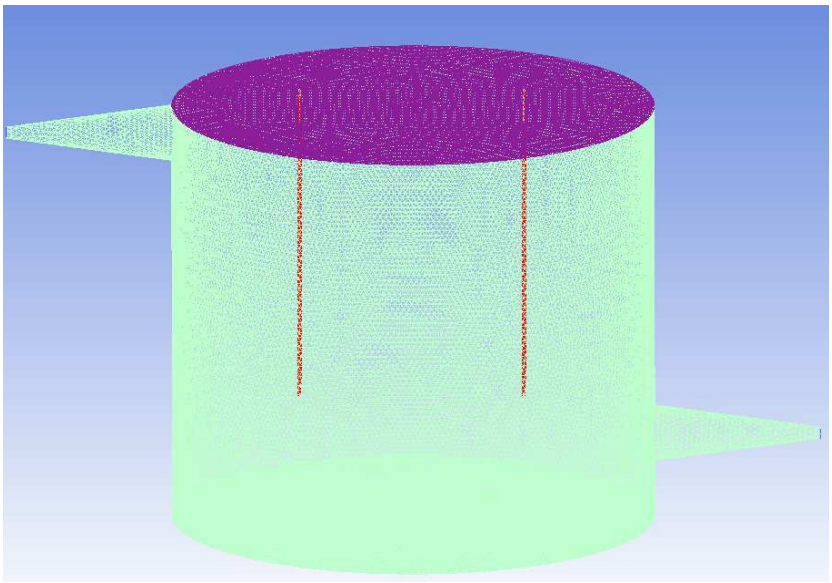

Figure 6.5 Non-structured (a) 2-D meshing grid model of cross-section view of electrowinning reactor; (b) 3-D meshing model of electrowinning reactor

6.3.3 Fluid Flow Modeling

The fundamental physical laws applicable to the electrolyte fluid flow system are the Navier-Stokes equations. The expression for the electrolyte fluid motion is given by:

$$\rho \frac{\partial u}{\partial t} + \rho(u \cdot \nabla)u = -\nabla P + \mu \nabla^2 u + \rho g \qquad (6.1)$$

Where P is the static pressure, u is the velocity, ρ is the density, ρg is the gravitational force and μ is the viscosity.

The continuity equation which expresses conservation of the mass is given by:

$$\nabla \cdot (\rho u) = 0 \qquad (6.2)$$

The boundaries of the electrowinning reactor include inlet, outlet, and inner cell walls. The boundary conditions were evaluated assuming that the fluid flow is incompressible laminar flow (RE<1000). The grid was extended to store the values of the physical properties at the boundaries.

6.3.3.1 Inlet boundary conditions

The distributions of all flow variables, except for pressure, were specified at the inlet to the electrowinning cell. The flow direction was top nozzle to the bottom nozzle on the opposite side of cell as presented in Figure 6.5. Uniform initial conditions were assumed for C_i and T,

$$C_i = C_\infty \qquad (6.3)$$

$$T = T_o \qquad (6.4)$$

On the fluid inlet boundary,

$$u_i = u_o \qquad (6.5)$$

$$C_i = C_{i\infty} \qquad (6.6)$$

6.3.3.2 Outlet boundary conditions

At the outlet boundary, the flow is directed out of the electrowinning domain. In our model, zero gradients for all variables, except for pressure, in the normal direction were assumed. On the fluid outlet boundary,

$$\frac{\partial c_i}{\partial n} = 0 \qquad (6.7)$$

6.3.3.3 Wall boundary conditions

In this modeling work, non-slip and non-penetrating wall conditions were assumed. The electrolyte velocity in the additional grid line was set to be zero and the gradient of the concentration was set to be zero as there is no mass transfer through the cell wall.

$$u_i = 0 \qquad (6.8)$$

$$\frac{\partial c_i}{\partial n} = 0 \qquad (6.9)$$

6.3.4 Fluid Flow velocity distribution

The electrolyte fluid flow velocity distribution is modeled at steady state when the inlet flow velocity is 0.027m/s and is depicted in Figure 6.6. It is shown that the velocity decreases after passing through the inlet and less flows are observed around electrodes as flows stopped after collision.

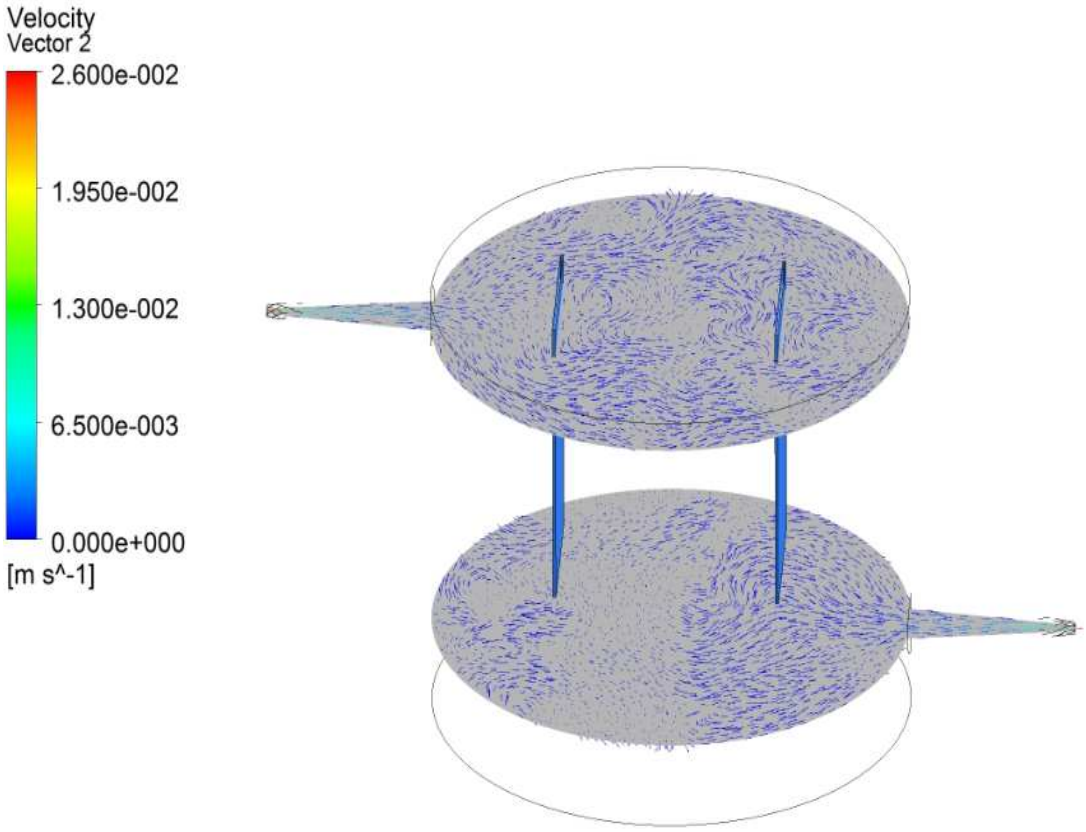

Figure 6.6 Electrolyte fluid flow velocity distribution in electrowinning cell with aspect ratio of 1:1

The velocity distribution on the copper cathode is shown in Figure 6.7. It is seen that the velocity is higher on the center of the electrode than on two ends. The formation of the circulation velocity in between electrodes makes the main contribution of higher fluid velocity.

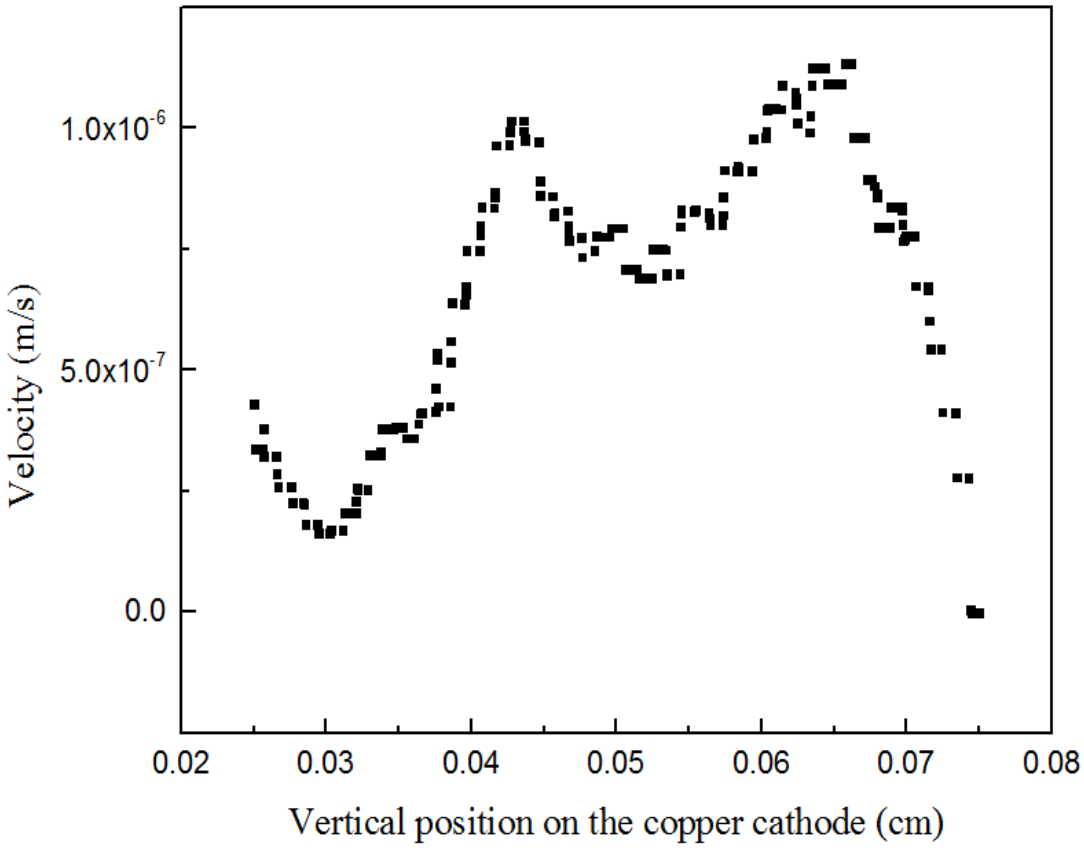

Figure 6.7 Electrolyte fluid flow velocity distribution on the copper cathode

This phenomenon can also be seen from velocity distribution between electrodes as described in Figure 6.8. The velocity exhibited a peak value in the half-way of electrodes confirming the formation of the circulation flow. This modeling provides insight of fluid flow in the recirculating electrowinning system, however, the validation of the modeled results is required in the further investigation.

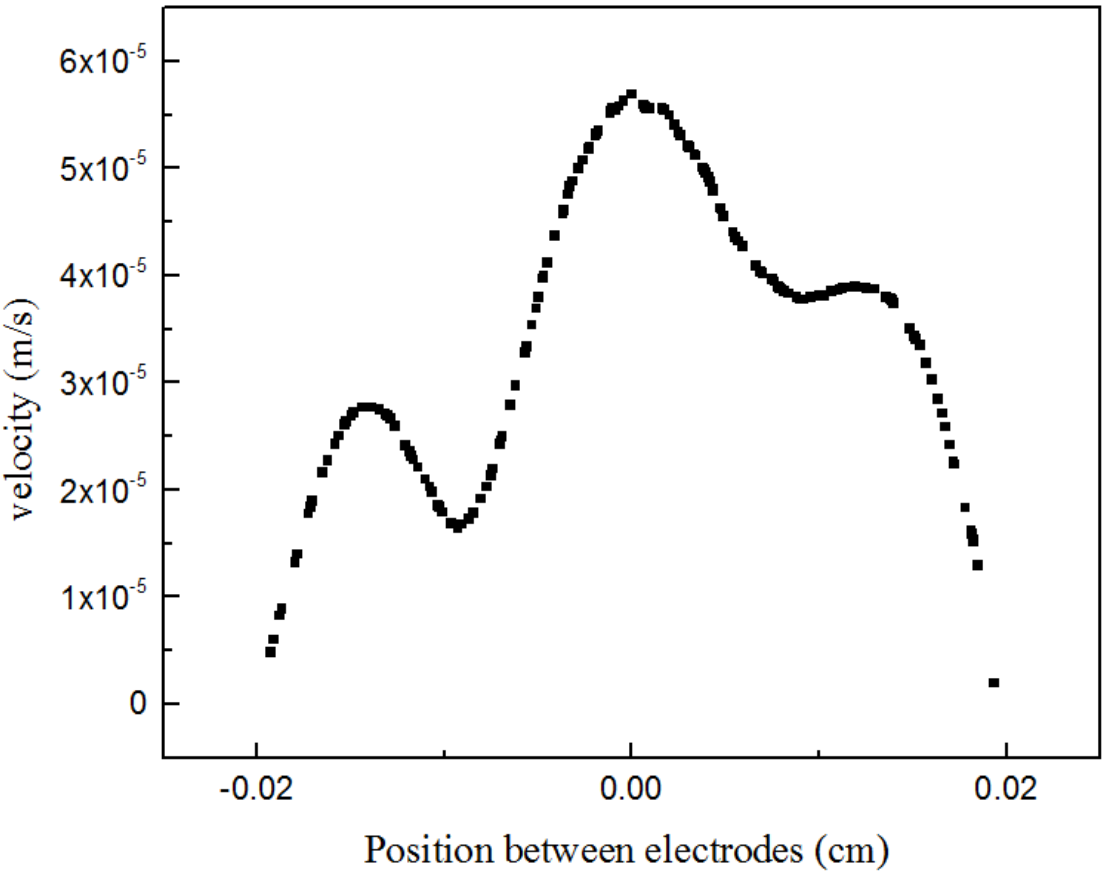

Figure 6.8 Electrolyte fluid flow velocity distribution between electrodes

CHAPTER 7

CONCLUSIONS AND FUTURE WORKS

7.1 Conclusions

Major goals of this research were achieved by successfully discovering a novel production route of zinc pure metal at low temperatures.

Zinc oxides were used as sources to electrodeposit metallic zinc. A eutectic mixture in a molar ratio 2:1 urea and choline chloride was used as electrolyte in this work. The dissolution of zinc oxide in the studied system has been investigated using FTIR and corresponding solubility measurement was carried out in ICP-AES. Through direct comparison of IR Peak identified for the $[ZnO{\cdot}Cl{\cdot}urea]^-$ complex, optimized solubility was found at a temperature of 100°C. The dissolution limit is approximated in FTIR with 1.23 mol/L ZnO in the Urea/ChCl eutectic mixture and is verified in ICP-AES with a measurement of 90584 ppm at 100°C.

The reduction potential of Zn^{2+} to Zn was found at -1.1V, using Ag as reference electrode. The reduction of Zn and its corresponding stripping process was characterized as irreversible and controlled by diffusion. Current-time transients were generated by stepping from -1.1V to -1.5V to investigate nucleation and growth mechanism. Average diffusion coefficient was confirmed 1.89×10^{-8} cm^2/s at 100°C. The nucleation process was characterized as instantaneous by comparing with 3-D nucleation model. Potentiostatic electrodeposition is done by fixing potential from -1.1 to -1.3V. XRD and EDS confirms the Zn in high purity had obtained. SEM micrographs were

showed morphology changed from small hexagonal crystal to agglomerated platelets as increasing potential. Process variables such as temperature and surface lubricant concentration were investigated in order to improve deposit layer surface quality. Temperature was proven to have large impact of the formation of deposit layer as nodular cauliflower like structure was formed at the top of each particle at 100°C. The addition of [Bmim]HSO_4 can effectively generate a more compact surface layer on the cathode and promote an improved finer grain size.

Lab-scale electrowinning of Zn was conducted from applied potentials from 3.2 to 3.5V at 90°C. Concentration polarization was confirmed in the beginning of the reaction and the diffusion coefficient was confirmed with an average value of 7.85×10^{-9} cm^2/s at 90°C which agrees to the previous value. A gradual increase of current density was due to activation polarization in which a linear correlation between current density and over-potential was confirmed. The kinetics study of the electrowinning process was carried out in the steady-state region. Tafel plots were obtained in temperatures from 80 to 100°C. The activation energy was obtained as 3.85 kJ/mol. The relatively low value suggested the very active electrode surface as well as the readiness of the reaction. The average transfer coefficient was calculated from the slope of the linear Tafel region and value was approximately 0.2, which suggested an irreversible charge transfer process. The effect of applied potential on microstructure was investigated. It was seen that dendrites formed in a higher over-potential of -0.65V and was beyond the calculated critical value for dendrite formation which is equal to -0.62V. Process variables such as cell voltage, temperature, and surface additive concentration were investigated to obtain higher current efficiency and lower energy consumption. An efficiency as high as 92.6% was obtained with 2.0mg/mL [Bmim]HSO_4 at 100°C, 3.3V showing a promising advantage over conventional zinc electrolytic technology which owns a efficiency close to 90%.

The feasibility of this novel technology was explored for large scale application, for example, in batch mode. Recirculation of the electrolyte achieves by maintaining a constant flow rate of 5 mL/min. Electrowinning duration is the main variable that was investigated under batch mode. The current efficiency was calculated with an average value of 88.8 ± 0.1% irrespective of electrowinning time. Correspondingly, energy consumption was calculated to be 3.23 ± 0.03 kWh/kg which shows reasonable agreement with results calculated in small scale electrowinning. The rate of cathodic weight gain is equal to 9.01×10^{-4} g/min at given condition. In addition, the graphite anode is proven to be stable during the long-term electrowinning as the rate of anodic weight loss is equal to 5.82×10^{-5} g/min which is an order of magnitude smaller than cathodic weight gain and this explains that the oxygen release on the anode only practices small impact on the carbon dioxide conversion on the anode, further confirming the viability of this zinc electrowinning in ionic liquid to be green and economically benign.

A model was established to study the electrolyte fluid flow velocity distribution in the electrowinning reactor. Results were illustrated that velocity in between electrodes is higher than other domain leading to the formation of cycling flow.

7.2 Future Works

The present research work was discovered a novel technology for zinc electrowinning using urea and choline chloride in a molar ratio of 2:1 low temperature deep eutectic solvents as electrolyte and investigated the feasibility of this technology for large-scale application. With the knowledge and understanding of this work, there are two main directions that can be further explored.

(1) Zn has been widely used and deposited onto iron surface for the purpose of enhancing the corrosion resistance. This idea can be extended to other metals such as Cobalt, Nickel, and Tin.

Given the remarkable solubility of ZnO in the studied electrolyte, cathode can be replacing by the targeting substrate and zinc coated metal cathode achieves provided proper potential. Electrochemical measurement is required to obtain and compare the reduction of Zn, target substrate, and metal alloys.

(2) Urea/ChCl in a molar ratio of 2:1 is known for a green solvent that is capable of selectively dissolve metal/metal oxide. This idea gives possibility of simplifying the purification process of the industrial slags for the zinc oxide recycling. Zinc coated galvanized steel scrap is the most widely used feed stock for Electric Arc Furnace (EAF) steel-making slag. The EAF dust waste are conventional recycled in an economically feasible way called Waelz Kiln technology and are produced into zinc oxide and iron units. With the novel technology, this recycling process can be conducted at lower temperature with simplified procedure.

REFERENCES

[1] H.S. Ray, R. Sridhar, and K.P. Abraham: Extraction of Nonferrous Metals (New Delhi: Affiliated East-West Press Pvt. Ltd., 1992), 1-5, 230-257, 260-261

[2] F. Habashi: "Recent Trends in Extractive Metallurgy," J. Min. Metall. Sect. B Metall, 45(2009), 1-13

[3] J.B.C. Kershaw: Electro-Metallurgy (University of Michigan Press, 2008)

[4] J. Emsley: Nature's Building Blocks (Oxford University Press, 2001)

[5] N. Greenwood, A. Earnshaw: Chemistry of the Elements, 2nd Edition, (Oxford: Butterworth-Heinemann, 1997), 1203

[6] R. Sekar, and S. Jayakrishnan: "Characteristics of Zinc Electrodeposits from Acetate Solutions," J Appl Electrochem, 36 (2006), 591–597

[7] N. Greenwood, A. Earnshaw: Chemistry of the Elements, 2nd Edition, (Oxford: Butterworth-Heinemann, 1997), 1202

[8] A.P. Brown, J.H. Meisenheider, and N. Yao: "The Alkaline Electrolytic Process for Zinc Production: A Critical Evaluation," Ind. Eng. Chem. Prod. Res. Dev, 22 (1983), 263-272

[9] A.W. Richards: "Zinc Processing," (Encyclopadia Britannica Online, 2009)

[10] F. Endres, A.P. Abbott and D. R. Macfarlane: Electrodeposition from Ionic Liquids (Wiley VCH 2008)

[11] A.P. Abbott and K.J. Mckenzie: "Application of Ionic Liquids to the Electrodeposition of Metals," Phys Chem Chem Phys, 8 (2006), 4265-4279

[12] R.G. Reddy: "Ionic Liquids: How Well Do We Know Them?" J. Phase. Equilib. Diff, 27 (2006), 210-211

[13] P. Walden: Bull. Acad. Imper. Sci (1914), 1800

[14] T.P. Wier, Jr and F.H. Hurley: "Electrodeposition of Aluminum," US patent 2, 446, 349, 1948

[15] J.S. Wilkes, J.A. Levisky, R.A. Wilson, C.L. Hussey: "Dialkylimidazolium Chloroaluminate Melts: A New Class of Room-temperature Ionic Liquids for Electrochemistry, Spectroscopy and Synthesis," Inorg. Chem, 21(1982) 1263-1264

[16] T.B. Scheffler, C.L. Hussey, K.R. Seddon, C.M. Kear, P.D. Armitage: "Molybdenum Chloro Complexes in Room-temperature Chloroaluminate Ionic Liquids: Stabilization of Hexachloromolybdate(2-) and Hexachloromolybdate(3-)," Inorg. Chem, 22 (1983), 2099-2100

[17] D. Appleby, C.L. Hussey, K.R. Seddon and J.E. Turp: "Room-Temperature Ionic Liquids as Solvents for Electronic Absorption Spectroscopy of Halide Complexes," Nature, 323 (1986) 614-616

[18] H.L. Chum, V.R. Koch, L.L. Miller, and R.A. Osteryoung: "Electrochemical Scrutiny of Organometallic Iron Complexes and Hexamethylbenzene in a Room Temperature Molten Salt," J. Am. Chem. Soc, 97 (1975), 3264-3265

[19] J. Robinson, and R.A. Osteryoung: "An Electrochemical and Spectroscopic Study of Some Aromatic Hydrocarbons in the Room Temperature Molten Salt System Aluminum Chloride-n-butylpyridinium Chloride," J. Am. Chem. Soc, 101 (1979), 323-327

[20] C.L. Hussey: "Room Temperature Molten Salt Systems," Adv. Molten Salt Chem, 5 (1983), 185

[21] A.A. Fannin, D.A. Floreani, L.A. King, J.S. Landers, B.J. Piersma, D.J. Stech, R.L. Vaughn, J.S. Wilkes and J.L. Williams: "Properties of 1,3-dialkylimidazolium Chloride-Aluminum Chloride Ionic Liquids. 1. Ion Interactions by Nuclear Magnetic Resonance Spectroscopy," J. Phys. Chem 88 (1984) 2609-2614

[22] J.S. Wilkes, J.A. Levisky, R.A. Wilson and C.L. Hussey: "Dialkylimidazolium Chloroaluminate Melts: A New Class of Room-temperature Ionic Liquids for Electrochemistry, Spectroscopy and Synthesis," Inorg. Chem 21 (1982) 1263-1264

[23] J.S. Wilkes, J.S. Frye, and G.F. Reynolds: "Aluminum-27 and Carbon-13 NMR Studies of Aluminum Chloride-dialkylimidazolium Chloride Molten Salts," Inorg. Chem 22 (1983) 3870-3872

[24] J.S. Wilkes, J.A. Levisky, J.L. Pflug, C.L. Hussey and T.B. Scheffler: "Composition Determinations of Liquid Chloroaluminate Molten Salts by Nuclear Magnetic Resonance Spectrometry," 54 (1982) 2378-2379

[25] C.L. Hussey, T.B. Scheffler, J.S. Wilkes, and A.A. Fannin: "Chloroaluminate Equilibria in the Aluminum Chloride-1-methyl-3-ethyimidazolium Chloride Ionic Liquid," J. Electrochem. Soc 133 (1986) 1389-1391

[26] J.S. Wilkes, and M.J. Zaworotko: "Air and Water Stable 1-ethyl-3-methylimidazolium Based Ionic Liquids," J. Chem. Soc., Chem. Commun 13 (1992) 965-967

[27] M. Gratzel: "Dye-Sensitized Solar Cells," J. Photochem. Photobiol C 4 (2003) 145–153

[28] P. Bonhote, A.P. Dias, N. Papageorgiou, K. Kalyanasundaram and M. Gratzel: "Hydrophobic, Highly Conductive Ambient-temperature Molten Salt," Inorg. Chem 35 (1996) 1168–1178

[29] N.V. Plechkova and K.R. Seddon: "Application of Ionic Liquids in the Chemical Industry," Chem. Soc. Rev 37 (2008) 123-150

[30] A. Stark and K. R. Seddon: "Kirk-Othmer Encyclopaedia of Chemical Technology," (John Wiley & Sons, New Jersey, 2007) 836–920

[31] A.P. Abbott, G. Capper, D.L. Davies, H.L. Munro, R.K. Rasheed and V. Tambyrajah: "Preparation of Novel, Moisture-stable, Levis-acidic Ionic Liquids Containing Quaternary Ammonium Salts with Functional Side Chains," Chem. Commun, 19 (2001) 2010-2011

[32] A.P. Abbott, G. Capper, D.L. Davies, R.K. Rasheed and V. Tambyrajah: "Novel Ambient Temperature Ionic Liquids for Zinc and Zinc Alloy Electrodeposition," Trans IMF, 79 (2001), 204-206

[33] A.P. Abbott, G. Capper, D.L. Davies, R.K. Rasheed and V. Tambyrajah: "Quaternary Ammonium Zinc- or Tin-containing Ionic Liquids: Water Insensitive, Recyclable Catalysts for Diels-Alder Reactions," Green Chem, 4 (2002), 24-26

[34] A.P Abbott, G. Capper, D. L Davies, R.K. Rasheed: "Ionic Liquid Analogues Formed from Hydrated Metal Salts," Chem. Eur. J, 10 (2004), 3769-3774

[35] A.P. Abbott, G. Capper, D. L. Davies, R.K. Rasheed and V. Tambyrajah: "Novel Solvent Properties of Choline Chloride/Urea Mixtures," Chem. Commun, 0 (2003), 70-71

[36] A.P. Abbott, D. Boothby, G. Capper, D.L. Davies, and R.K. Rasheed: "Deep Eutectic Solvents Formed between Choline Chloride and Carboxylic Acids: Versatile Alternatives to Ionic Liquids," J. Am. Chem. Soc, 126 (2004), 9142-9147

[37] Q. Zhang, K. Vigier, S. Royer and F. Jerome: "Deep Eutectic Solvents: Syntheses, Properties and Applications," Chem. Soc. Rev, 41 (2012) 7108-7146

[38] C. Rub and B. Konig: "Low Melting Mixtures in Organic Synthesis – An Alternative to Ionic Liquids?" Green. Chem, 14 (2012) 2969-2982

[39] C. D'Agostino, R.C. Harris, A.P. Abbott, and M.D. Mantle: "Molecular Motion and Ion Diffusion in Choline Chloride Based Deep Eutectic Solvents Studied by 1H Pulsed Field Gradient NMR Spectroscopy," 13 (2011) 21383-21391

[40] A.M. Popescu, C. Donath, V. Constantin: "Density, Viscosity and Electrical Conductivity of Three Choline Chloride Based Ionic Liquids," 46 (2014) 452-457

[41] R.B. Leron, M.H. Li: "Molar Heat Capacities of Choline Chloride-Based Deep Eutectic Solvents and Their Binary Mixtures with Water" Thermochimica Acta, 530 (2012) 52-57

[42] J.M. Crosthwaite, M.J. Muldoon, J.K. Dixon, J.L. Anderson, and J.F. Brennecke: "Phase Transition and Decomposition Temperatures, Heat Capacities and Viscosities of Pyridinium Ionic Liquids," J. Chem. Thermodyn 37 (2005) 559–568

[43] A.P. Abbott, G. Capper, D.L. Davies, R.K. Rasheed and P. Shikotra: "Selective Extraction of Metals from Mixed Oxide Matrixes Using Choline-Based Ionic Liquids," Inorg. Chem, 44 (2005) 6497-6499

[44] V.L. Cherginets, E.G. Khailova: "On the Solubilities of Bivalent Metal Oxides in Molten Alkaline Chlorides," Electrochim. Acta, 39 (1994), 823-829

[45] H. Kamimura, T. Kubb, I. Minami, and S. Mori: "Effect and Mechanism of Additives for Ionic Liquids as New Lubricants," Tribol Int, 40 (2007), 620-625

[46] T. Welton: "Room Temperature Ionic Liquids. Solvents for Synthesis and Catalysis," Chem Rev, 99 (1999) 2071-2084

[47] Z. Yong: "Recent Advances in Ionic Liquids for Synthesis of Inorganic Nanomaterials," Curr. Nanosci, 1 (2005) 35-42

[48] K. Hoenicke, R. Gatermann, W. Harder, and L. Hartig: "Analysis of Acrylamide in Different Foodstuffs using Liquid Chromatography–Tandem Mass Spectrometry and Gas Chromatography–Tandem Mass Spectrometry," Anal Chim Acta, 520 (2004), 207-215

[49] C. Ye, W. Liu, Y. Chen, and L. Yu: "Room-temperature Ionic Liquids: a Novel Versatile Lubricant," Chem. Commun, 21 (2001) 2244-2245

[50] Q. Zhang, Y. Hua: "Effects of 1-Butyl-3-Methylimidazolium Hydrogen Sulfate-[BMIM]HSO4 on Zinc Electrodeposition from Acidic Sulfate Electrolyte," J. Appl. Electrochem, 39 (2009) 261-267

[51] N.M. Pereira, P.M. Fernandes, C.M. Pereira, and A.F. Silva: "Electrodeposition of Zinc from Choline Chloride-Ethylene Glycol Deep Eutectic Solvent: Effect of the Tartrate Ion," 159 (2012) D501-506

[52] K.I. Popov, S.S. Djokic, and B.N. Grgur: "Fundamental Aspects of Electrometallurgy," Springer (2002) 14-34

[53] D. Pradhan: "Fundamental Studies on Electrochemical Production of Dendrite-free Aluminum and Titanium-aluminum Alloys," Ph.D Dissertation, the University of Alabama, (2010) 1-179

[54] B.N. Pal and D. Chakravorty: "Pattern Formation of Zinc Nanoparticles in Silica Film by Electrodeposition," J. Phys. Chem. B, 110 (2006) 20917-20921

[55] A.R. Despic, J. Diggle and J. O'M. Bockris: "Mechanism of the Formation of Zinc Dendrites," 115 (1968) 507-508

[56] H. Yang and R.G. Reddy: "Fundamental studies on electrochemical deposition of lead from lead oxide in 2:1 Urea/Choline chloride ionic liquids," J. Electrochem. Soc, 161 (2014) D586-592

[57] D. Pradhan, R. G. Reddy and D. Mantha: "Dendrite Free Aluminum Electrodeposition using Ionic Liquid Electrolyte," Proceedings of the Sadoway 60 Symposium, MIT, Cambridge, Massachusetts, USA, (2010) 106-112

[58] R. G. Reddy: "Low Temperature production of zinc from zinc oxide," Carbon Management Technology Conference, CMTC, Orlando, FL (2012) 1-6

[59] D. Pradhan and R. G. Reddy: "Low Temperature Electrochemical Synthesis of Ti-Al Alloys using Ionic Liquid Electrolytes," TMS, Warrendale, USA, (2008) 345-352

[60] D. Pradhan and R. G. Reddy: "Effect of Electrode Physical Properties on Dendritic Deposition of Aluminum using EmimCl-AlCl3 ionic liquid electrolyte," TMS Warrendale, USA, (2009) 17-24

[61] A.J. Bard and L.R. Faulkner: Electrochemical Methods: Fundamental and Applications, (John Wiley& Sons, New York 2000)

[62] A. Radisic, J. G. Long, P. M. Hoffmann and P.C.Searson: "Nucleation and Growth of Copper on TiN from Pyrophosphate Solution," J. Electrochem Soc, 148 (2001) 41-46

[63] V. Kamavaram: "Novel Electrochemical Refining of Aluminum Based Materials in Low Temperature Ionic Liquid Electrolytes," Ph. D Dissertation, the University of Alabama, (2004) 141-149

[64] Y. Zheng, K. Dong, Q. Wang, S. Zhang, and X. Lu: "Electrodeposition of Zinc Coatings from the Solutions of Zinc Oxide in Imidazolium Chloride/Urea Mixtures," Sci China Chem, 55 (2012), 1587-1597

[65] D. Yue, Y. Jia, Y. Yao, J. Sun, and Y. Jing: "Structure and Electrochemical Behavior of Ionic Liquid Analogue Based on Choline Chloride and Urea," Electrochim. Acta, 65 (2012) 30-36

[66] A.P. Abbott, G.C. Capper, D.L. Davies, K.J. Mckenzie and S.U. Obi: "Solubility of Metal Oxides in Deep Eutectic Solvents Based on Choline Chloride," J. Chem. Eng. Data, 51 (2006) 1280-1282

[67] R.S. Nicholson: "Theory and Application of Cyclic Voltammetry for Measurement of Electrode Reaction Kinetics," Anal. Chem 37 (1965) 1351-1355

[68] R. S. Nicholson, and I. Shain: "Theory of Stationary Electrode Polarography. Single Scan and Cyclic Methods Applied to Reversible, Irreversible, and Kinetic Systems," Anal. Chem 36 (1964) 706-723

[69] H. Yang and R.G. Reddy: "Electrochemical Deposition of Zinc from Zinc Oxide in 2:1 Urea/Choline Chloride Ionic Liquid;" Electrochim. Acta 147 (2014) 513-519

[70] A. Gomes, M. I. da Silva Pereira: "Zn Electrodeposition in the Presence of Surfactants: Part I. Voltammetric and Structural Studies," Electrochim. Acta 52 (2006) 863-871

[71] P. Chen, I. Sun: "Electrodeposition of Cobalt and Zinc Cobalt Alloys from a Lewis Acidic Zinc Chloride-1-Ethyl-3-Methylimidazolium Chloride Molten Salt," Electrochim. Acta 46 (2001) 1169-1177

[72] Y. Nuli, J. Yang, P. Wang: "Electrodeposition of magnesium film from BMIMBF4 ionic liquid," Appl. Surf. Sci 252 (2006) 8086-8090

[73] T. Jiang, M.J. Chollier, G. Dube, A. Lasia and G.M. Brisard: "Electrodeposition of Aluminium from Ionic Liquids: Part I—Electrodeposition and Surface Morphology of Aluminium from Aluminium Chloride (AlCl3)–1-ethyl-3-methylimidazolium Chloride ([EMIm]Cl) Ionic Liquids," Sur. Coat. Tech, 201 (2006), 1-9

[74] Y. Zhao and T. J. VanderNoot: "Electrodeposition of aluminium from room temperature AlCl3-TMPAC molten salts," Electrochim. Acta 42 (1997) 1639-1643

[75] A. Radisic, J. G. Long, P. M. Hoffmann and P.C.Searson: "Nucleation and Growth of Copper on TiN from Pyrophosphate Solution," J. Electrochem Soc, 148 (2001) 41-46

[76] B. Scharifker and G. Hills: "Theoretical and Experimental Studies of Multiple Nucleation," Electrochim Acta, 28 (1981) 879-889

[77] B. Scharifker and J. Mostany: "Three-dimensional Nucleation with Diffusion Controlled Growth: Part II: The Nucleation of Lead on Vitreous Carbon," J. Electroanal. Chem, 177 (1984) 25-37

[78] J. Lee, B. Miller, X. Shi, R. Kalish, and K. A. Wheeler: "Aluminum Deposition and Nucleation on Nitrogen- incorporated Tetrahedral Amorphous Carbon Electrodes in Ambient Temperature Chloroaluminate Melts," J. Electrochem Soc, 147 (2000), 3370–3376

[79] B. Scharifker and J, Mostany: "Three-dimensional Nucleation with Diffusion Controlled Growth: Part I. Number Density of Active Sites and Nucleation Rates Per Site," J. Electroanal. Chem, 177 (1984), 13-23

[80] M. Li, Z. Wang and R. G. Reddy: "Cobalt Electrodeposition using Urea and Choline Chloride," Electrochim Acta 123 (2014) 325-331

[81] D. Pradhan, and R.G. Reddy: "Mechanistic study of Al electrodeposition from EMIC-AlCl3 and BMIC-AlCl3 electrolytes at low temperature," Mater. Chem. Phys 143 (2013) 564-569

[82] V. Kamavaram, D. Mantha, and R.G. Reddy: "Recycling of Aluminum metal-matrix composites using Ionic Liquids: Effect of Process Variables on current efficiency and deposit Characteristics," Electrochim. Acta 50 (2005) 3286-3295

[83] P. Chen, and C.L. Hussey: "The electrodeposition of Mn and Zn–Mn alloys from the room-temperature tri-1-butylmethylammonium bis((trifluoromethane)sulfonyl)imide ionic liquid," Electrochim. Acta 52 (2007) 1857-1864

[84] W.R. Pitner, and C.L. Hussey: "Electrodeposition of Zinc from the Lewis Acidic Aluminum Chloride-1-Methyl-3-ethylimidazolium Chloride Room Temperature Molten Salt," J. Electrochem. Soc 144 (1997) 3095-3103

[85] A.P. Abbott, G. Capper, K.J. Mckenzie, K.S. Ryder: "Electrodeposition of Zinc-tin Alloys from Deep Eutectic Solvents Based on Choline Chloride," J. Electroanal. Chem, 599 (2007), 288-294

[86] Z. Liu, S. Zein El Abedin, F. Endres: "Electrodeposition of Zinc Films from Ionic Liquids and Ionic Liquid/water Mixtures," Electrochim. Acta, 89 (2013) 635-643

[87] H. Yang and R. G. Reddy: "Electrodeposition of Zinc from Zinc Oxide using Urea and Choline Chloride Mixture: effect of [BMIM]HSO4, Temperature, Voltage on current Efficiency, Energy Consumption, and Surface Morphology," Rare Metal Technology (2014) TMS, Warrandale, USA, 21-26

[88] T. Tsuda, L. Boyd, S. Kuwabata, and C.L. Hussey: "Electrochemical Behavior of Copper(I) Oxide in Urea-Choline Chloride Room-Temperature Melts," ECS Trans 16 (2009) 529-540

[89] A. P. Abbott, G. Capper, K. J. McKenzie and K. S. Ryder: "Electrodeposition of Zinc Tin Alloys from Deep Eutectic Solvents Based on Choline Chloride," J. Electroanal. Chem. 599 (2007) 288-294

[90] D. Grujicic, and B. Pesic: "Electrodeposition of Copper: The Nucleation Mechanisms;" Electrochim. Acta 47 (2002) 2901-2912

[91] D. Pradhan, D. Mantha, R.G. Reddy: "The Effect of Electrode Surface Modification and Cathode Overpotential on Deposit Characteristics in Aluminum Electrorefining Using EMIC–AlCl3 Ionic Liquid Electrolyte," Electrochim. Acta 54 (2009) 6661-6667

[92] J.J. Salvador-Pascual, S. Citalan-Cigarroa, O. Solorza-Feria: "Kinetics of Oxygen Reduction Reaction on Nanosized Pd Electrocatalyst in Acid Media," J. Power. Sources 172 (2007) 229-234

[93] N.M. Markovic, B.N. Grgur, and P.N. Ross: "Temperature-Dependent Hydrogen Electrochemistry on Platinum Low-Index Single-Crystal Surfaces in Acid Solutions," J. Phys. Chem. B 101 (1997) 5405-5413

[94] K.I. Popov, S.S. Djokic, and B.N. Grgur: "Fundamental Aspects of Electrometallurgy," Springer (2002) 78-79

[95] C.M. Lopez and K. Choi: "Electrochemical Synthesis of Dendritic Zinc Films Composed of Systematically Varying Motif Crystals," Langmuir, 22 (2006) 10625-10629

[96] D. Pradhan and R.G. Reddy: "Dendrite-Free Aluminum Electrodeposition from AlCl3-1-Ethyl-3-Methyl-Imidazolium Chloride Ionic Liquid Electrolytes," Metall. Trans B, 43B (2012) 519-531

[97] S.H. Zhang, and S.B. Lyon: "The Electrochemistry of Iron, Zinc and Copper in Thin Layer Electrolytes," Corr. Sci, 35 (1993) 713-718

[98] N. Nikolic, K. Popov, L. Pavlovic and M. Pavlovic: "Determination of Critical Conditions for the Formation of Electrodeposited Copper Structures Suitable for Electrodes in Electrochemical Devices," Sensors, 7 (2007) 1-15

[99] K. Popov, M. Pavlovic, M. Spasojevic, V. Nakic: "The Critical Overpotential for Copper Dendrite Formation," J. Appl. Electrochem, 9 (1979) 533-536

[100] M. Zhang: "Modeling and Experimental Validation of Aluminum Electrowinning in Chloroaluminate Ionic Liquids at Low Temperatures," Ph. D Dissertation, the University of Alabama, (2008) 112-113

[101] E.A. Brandes and G.B. Brook: Smithells Metals Reference Book (7th Edition, Elsevier, 1998) 19 1-69

[102] H.O. Pierson: Handbook of Carbon, Graphite, Diamond and Fullerenes-Properties, Processing and Applications (William Andrew Publishing/Noyes, 1993) 54 1-87

APPENDIX I

CALCULATION OF CURRENT EFFICIENCY AND ENERGY CONSUMPTION DURING ZINC ELECTRO-DEPOSITION PROCESS

The experiment conducted with modified copper cathode, platinum anode, applied voltage of 3.5V, at a temperature of 85°C for 2 hours in a non-stirring solution.

Current Efficiency (ŋ) Calculation:

Weight of Zn deposit on cathode = $\Delta W = W_{final} - W_{initial} = 1.1097 - 1.0751 = 0.0326g$

The theoretical weight (W_T) of Zn deposited on cathode was calculated using Faraday's Law:

$$W_T = \frac{Ita}{nF}$$

Where,

I= Cathodic current (A)

t= Total experimental time (s)

a= Atomic weight of Zn=65.39

nF= Molar charge

It can be calculated from the area under the current density (i) vs. time (t) plot, times by cathode area of deposition.

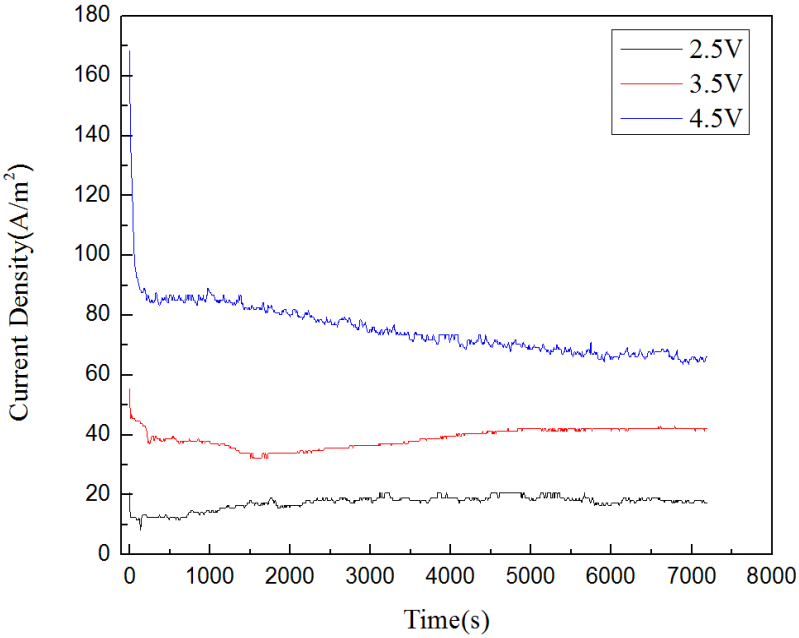

Area under the curve = i.t.A = 105.4519 A.s/cm^2;

$$W_T = \frac{i.t.A.a}{nF} = \frac{105.4519 \times 65.39}{2 \times 96480} = 0.03573\text{g}$$

Current efficiency, η = actual weight (ΔW) / Theoretical weight (W_t) = 91.2%.

$$\eta = 91.2\%$$

Energy Consumption (E) Calculation:

$$E = V\frac{Q}{\eta}$$

Where,

V = Applied voltage = $|E_{cathode} - E_{anode}|$ = 3.5V

Q =I.t = Passed charge in the solution = 105.4519 A.s

Thus, Charges/ 1000g = 105.4519 ×1000/ η = 2951354.60 Coulomb

Energy Consumption (E) = $\frac{3.5 \times 2951354.60}{0.912 \times 1000 \times 3600}$ kWh/kg of Zn = 3.15 kWh/kg of Zn

APPENDIX II

SEM MICROGRAPHS TAKEN FROM ALUMINUM ELECTRODE AND COPPER ELECTRODE

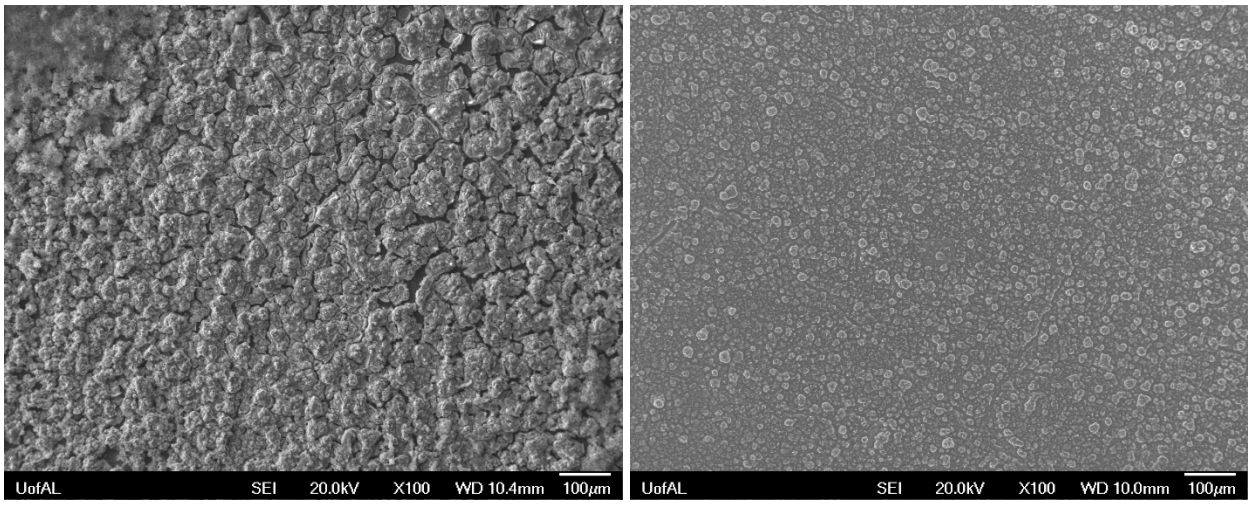

Figure. (a) Deposited layer morphology taken from aluminum electrode; (b) from copper electrode

APPENDIX III

CALCULATION OF CRITICAL CATHODE OVERPOTENTIAL (η_{crt})

Calculation of cathodic transfer coefficient (α_c):

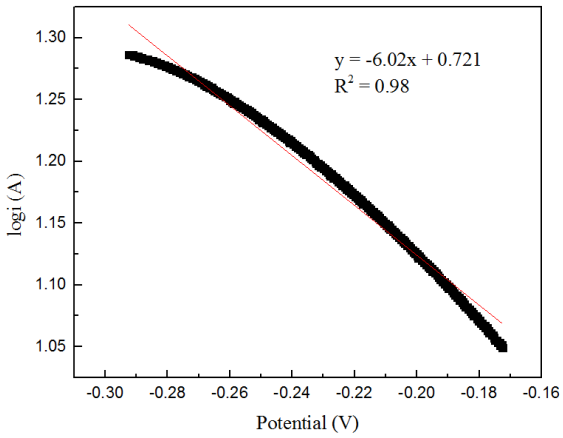

From Tafel equation:

$$\log i = \log i_o + \left(\frac{\alpha_c \cdot \mathrm{n} \cdot \mathrm{F}}{2.303\mathrm{RT}}\right) \cdot \eta \quad (1)$$

where,

η is the cathodic over-potential (V),

i is the cathodic current density (A/m^2),

R is gas constant,

T is the temperature (K),

i_o is the exchange current density (A/m^2),

α_c is the cathodic transfer coefficient,

n is the number of transferred electrons,

F is the Faraday's constant

The average calculated value for α_c is

$$\boldsymbol{\alpha_c = 0.2}$$

Calculation of cathodic over-potential (η_{crt}):

$$\eta_{crt} = \frac{RT}{\alpha F} ln\left(\frac{i_L \delta}{i_o h}\right) \qquad (2)$$

where,

h is the average height of the growing dendrite that is equal to 314.3 μm,

δ is the diffusion layer thickness

i_o is the exchange current density equal to 10.3442 A/m^2,

α is equal to 0.2

T is 363K

The product of $i_L \cdot \delta$ can be calculated from eq. 3

$$i_L = \frac{nFDC}{\delta} \qquad (3)$$

where,

n is the number of transferred electrons,

D is calculated to be $7.85 \times 10^{-13} m^2/s$

F is the Faraday constant

C is bulk concentration of electro-active species which is equal to 0.41mol/L

$$\boldsymbol{\eta_{crt} = -0.62V}$$